# The Galaxy in Context: Structural, Kinematic & Integrated Properties

**Joss Bland-Hawthorn[1], Ortwin Gerhard[2]**

[1]Sydney Institute for Astronomy, School of Physics A28, University of Sydney, NSW 2006, Australia; email: jbh@physics.usyd.edu.au
[2]Max Planck Institute for extraterrestrial Physics, PO Box 1312, Giessenbachstr., 85741 Garching, Germany; email: gerhard@mpe.mpg.de

Annu. Rev. Astron. Astrophys. 2016. 54:529–596

This article's doi: 10.1146/annurev-astro-081915-023441



**Keywords**

Galaxy: Structural Components, Stellar Kinematics, Stellar Populations, Dynamics, Evolution; Local Group; Cosmology

**Abstract**

Our Galaxy, the Milky Way, is a benchmark for understanding disk galaxies. It is the only galaxy whose formation history can be studied using the full distribution of stars from faint dwarfs to supergiants. The oldest components provide us with unique insight into how galaxies form and evolve over billions of years. The Galaxy is a luminous ($L_\star$) barred spiral with a central box/peanut bulge, a dominant disk, and a diffuse stellar halo. Based on global properties, it falls in the sparsely populated "green valley" region of the galaxy colour-magnitude diagram. Here we review the key integrated, structural and kinematic parameters of the Galaxy, and point to uncertainties as well as directions for future progress. Galactic studies will continue to play a fundamental role far into the future because there are measurements that can only be made in the near field and much of contemporary astrophysics depends on such observations.

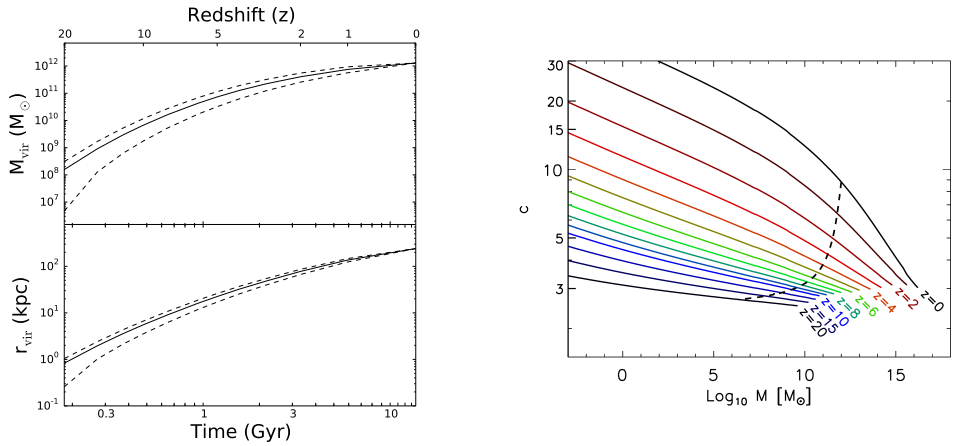


**Figure 1**

Left: The estimated growth of the Galaxy's virial mass ($M_{\rm vir}$) and radius ($r_{\rm vir}$) from $z = 20$ to the present day, $z = 0$. Throughout this review, we use $h = 0.7$, $\Omega_{\rm M} = 0.3$ and $\Omega_\Lambda = 0.7$. The virial radius at any epoch is the approximate extent over which the growing Galaxy has stabilized. This plot was derived from 5000 runs of the tree merger code of Parkinson, Cole & Helly (2008): the dashed lines encompass 67% of the predicted halos at each epoch ($1\sigma$ uncertainty). Right: The discrete curves show how the NFW concentration parameter $c$ depends on halo mass $M_{\rm vir}$ as a function of cosmic epoch indicated by the different line colours. If Galactic dark matter is correctly described by an NFW halo, the dashed line shows how $c$ evolves with mass (and therefore cosmic time). The central regions form early on and most of the accreted matter settles to the outer halo (adapted from Correa et al. 2015).

## 1. PROLOGUE

Galactic studies are a fundamental cornerstone of contemporary astrophysics. Nowadays, we speak of near-field cosmology where detailed studies of the Galaxy underlie our understanding of universal processes over cosmic time (Freeman & Bland-Hawthorn 2002). Within the context of the cold dark matter paradigm, the Galaxy built up over billions of years through a process of hierarchical accretion (see Fig. 1). Our Galaxy has recognisable components that are likely to have emerged at different stages of the formation process. In particular, the early part of the bulge may have collapsed first seeding the early stages of a massive black hole, followed by a distinct phase that gave rise to the thick disk. The inner halo may have formed about the same time while the outer halo has built up later through the progressive accretion of shells of material over cosmic time (Prada et al. 2006). The dominant thin disk reflects a different form of accretion over the same long time frame (Brook et al. 2012).

We live in an age when vast surveys have been carried out across the entire sky in many wavebands. At optical and infrared wavelengths, billions of stars have been catalogued with accurate photometric magnitudes and colours (Skrutskie et al. 2006; Saito et al. 2012; Ivezić, Beers & Jurić 2012). But only a fraction of these stars have high quality spectral classifications, radial velocities and distances, with an even smaller fraction having useful elemental abundance determinations. The difficulty of measuring a star's age continues to hamper progress in Galactic studies, but this stumbling block will be partly offset by the ESA GAIA astrometric survey already under way. By the end of the decade, this mission will

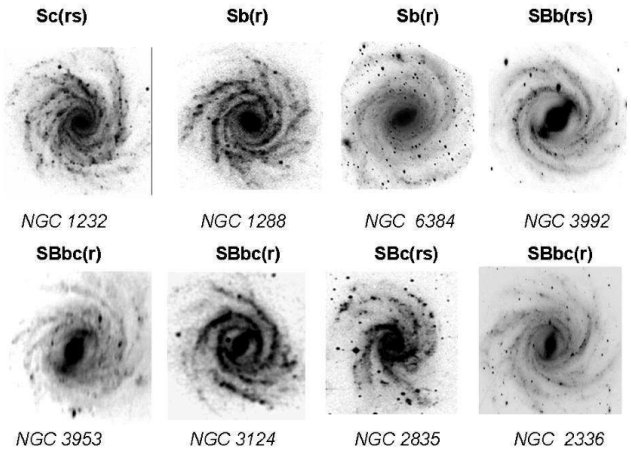


**Figure 2**

Milky Way analogues – a selection of galaxies that broadly resemble the Galaxy (Efremov 2011). All images have been rectified to a flat projection. Classifications within the de Vaucouleurs morphological classification scheme are also shown.

have measured accurate distances and velocity vectors for many millions of stars arising from all major components of the Galaxy (de Bruijne et al. 2015). In light of this impending data set, we review our present understanding of the main dynamical and structural parameters that describe our home, the Milky Way.

We run into a problem familiar to cartographers. How is one to describe the complexity of the Galaxy? No two galaxies are identical; even the best morphological analogues with the Milky Way have important differences (Fig. 2). Historically, astronomers have resorted to defining discrete components with the aim of measuring their structural parameters (see Table 1). We continue to see value in this approach and proceed to define what we mean by each subsystem, and the best estimates that can be made at the present time. In reality, these 'components' exhibit strong overlap by virtue of sharing the same evolving Galactic potential (e.g. Guedes et al. 2013) and the likelihood that stars migrate far from their formation sites (Sellwood & Binney 2002; Minchev & Famaey 2010).

Even with complete data (density field, distribution function, chemistry), it is unlikely that any one component can be entirely separated from another. In particular, how are we to separate the bar/bulge from the inner disk and inner halo? A distinct possibility is that most of our small bulge (compared to M31) has formed through a disk instability associated with bar formation, rather than during a dissipational early collapse phase. The same challenge exists in separating the thin disk from the thick disk. Some have argued for a gradual transition but there is now good evidence that a major part of the thick disk is chemically distinct from the dominant thin disk, suggesting a different origin. In this context, Binney (2013) has argued that the Galaxy's stellar populations are better described by phase-space distribution functions (DF) that are self-consistent with the underlying gravitational potential (§5).

Our goal here is to identify the useful structural and kinematic parameters that aid comparison with other galaxies and place our Galaxy in context. These "measurables" are

**Table 1 Description of Galactic parameters[a].**

| | |
|---|---|
| $R_0$ | Distance of Sun from the Galactic Centre (§3.2) |
| $z_0$ | Distance of Sun from the Galactic Plane (§3.3) |
| $\Theta_0, \Omega_0$ | Circular speed, angular velocity at Sun with respect to Galactic Centre (§3.4, §6.4.2) |
| $U_\odot, V_\odot, W_\odot$ | $U$, $V$, $W$ component of solar motion with respect to LSR (§5.3.3) |
| $\mathbf{v}_\odot$ | Solar motion with respect to LSR (§5.3.3) |
| $V_{\rm LSR}$ | Possible LSR streaming motion with respect to $\Theta_0$ (§5.3.3, §6.4.2) |
| $A$, $B$ | Oort's constants (§6.4.2) |
| $r_{\rm vir}$ | Galactic virial radius (§6.3) |
| $M_{\rm vir}$, $M_{\rm vir,timing}$ | Galactic virial mass, virial timing mass (§6.3) |
| $M_\star$, $\dot{m}_\star$ | Galactic stellar mass, global star formation rate (§2.2) |
| $M_{\rm bary}$, $f_{\rm bary}{}^b$ | Galactic baryon mass, baryon fraction (§6.2, §6.4.3) |
| $M_{\rm b}^{\rm dyn}$, $M_{\rm b}^*$, $M_{\rm clb}/M_{\rm b}^*$ | Bulge dynamical mass and stellar mass, classical bulge fraction (§4.2.4) |
| $\sigma_x^b, \sigma_y^b, \sigma_z^b, \sigma_{\rm rms}^b$ | Half-mass bulge velocity dispersions in $(x, y, z)$ and rms (§4.2.3) |
| $\phi_{\rm bp}$, $(b/a)_{\rm bp}$ | b/p-bulge orientation and axis ratio from top (§4.2.1) |
| $h_{\rm bp}$, $(c/a)_{\rm bp}$ | Central vertical scale-height and edge-on axis ratio of b/p-bulge (§4.2.1) |
| $x_X$ | Radius of maximum X (§4.2.1) |
| $M_{\rm tlb}$, $M_{\rm slb}$ | Stellar masses of thin and superthin long bar (§4.3) |
| $\phi_{\rm lb}$, $R_{\rm lb}$ | Long bar orientation and half-length (§4.3) |
| $h_{\rm tlb}$, $h_{\rm slb}$ | Vertical scale heights of thin and superthin long bar (§4.3) |
| $\Omega_b$, $R_{\rm CR}$ | Bar pattern speed and corotation radius (§4.4) |
| $M_\bullet$, $r_{\rm infl}$ | Mass and dynamical influence radius of supermassive black hole (§3.4) |
| $M_{\rm NSC}$, $M_{\rm NSD}$ | Masses of nuclear star cluster and nuclear stellar disk (§4.1) |
| $r_{\rm NSC}$, $(c/a)_{\rm NSC}$ | Nuclear star cluster half-mass radius and axis ratio (§4.1) |
| $r_{\rm NSD}$, $h_{\rm NSD}$ | Nuclear stellar disk break radius and vertical scale-height (§4.1) |
| $M_{\rm hot}$ | Coronal (hot) halo mass (§6.2) |
| $M_{\rm s}$, $M_{\rm sub}$ | Stellar halo mass and substructure mass (§6.1.2) |
| $\alpha_{\rm in}$, $\alpha_{\rm out}$, $r_{\rm s}$ | Stellar halo inner, outer density slope, break radius (§6.1.1) |
| $q_{\rm in}$, $q_{\rm out}$ | Inner and outer mean flattening (§6.1.1) |
| $\sigma_r^{\rm s}$, $\sigma_\theta^{\rm s}$, $\sigma_\phi^{\rm s}$ | Stellar halo velocity dispersions in $r$, $\theta$, $\phi$ near the Sun (§6.1.3) |
| $\overline{v}_\phi^{\rm s}$ | Local halo rotation velocity (§6.1.3) |
| $M^{\rm t}$, $M^{\rm T}$ | Thin, thick disk stellar masses (§5.1.3, §5.2.2) |
| $R^{\rm t}$, $R^{\rm T}$ | Thin, thick disk exponential scalelength in $R$ (§5.1.3, §5.2.2) |
| $z^{\rm t}$, $z^{\rm T}$ | Thin, thick disk exponential scaleheight in $z$ (§5.1.3) |
| $f_\rho$, $f_\Sigma$ | Thick disk fraction in local density, in integrated column density (§5.1.3) |
| $\sigma_R^{\rm t}$, $\sigma_z^{\rm t}$ | Old thin disk velocity dispersion in $R$, $z$ at 10 Gyr (§5.4) |
| $\sigma_R^{\rm T}$, $\sigma_z^{\rm T}$ | Thick disk velocity dispersion in $R$, $z$ (§5.4) |
| $\Sigma_{\rm tot}$, $\rho_{\rm tot}$, $\epsilon_{\rm tot}$ | Local mass surface density, mass density, dark matter energy density (§5.4.2) |

[a] Our convention is to use $R$ for a projected radius in two dimensions (e.g. disk) and $r$ for a radius in three dimensions (e.g. halo). [b] $f_{\rm bary}$ is the ratio of baryonic mass to total mass integrated to a radius where both quantities have been determined (e.g. $r_{\rm vir}$).

also important for comparing with numerical simulations of synthetic galaxies. A simulator runs a disk simulation and looks to compare the evolutionary phase where the bar/bulge instability manifests itself. In principle, only a statistical 'goodness of fit' is needed without resorting to any parametrisation (Sharma et al. 2011). But in practice, the comparison is likely to involve global properties like rotation curves, scale lengths, total mass (gas, stars, dark matter), stellar abundances and the star formation history. Here we focus

on establishing what are the best estimates for the Galaxy's global properties and the parameters that describe its traditional components.

Kerr & Lynden-Bell (1986) revisited the 1964 IAU standards for the Sun's distance and circular velocity ($R_0$ = 10 kpc; $\Theta_0$ = 250 km s$^{-1}$) relative to the Galactic Centre and proposed a downward revision ($R_0$ = 8.5 kpc; $\Theta_0$ = 220 km s$^{-1}$). Both values can now be revised further to reflect the new observational methods at our disposal three decades on. Our goal in this review is to provide an at-a-glance summary of the key structural and kinematic parameters to aid the increasing focus on Galactic studies. For reasons that become clear in later sections, we cannot yet provide summary values that are all internally consistent in a plausible dynamical description of the Galaxy; this is an important aim for the next few years. For more scientific context, we recommend reviews over the past decade that consider major components of the Galaxy: Helmi (2008), Ivezić, Beers & Jurić (2012), Rix & Bovy (2013) and Rich (2013).

This is an era of extraordinary interest and investment in Galactic studies exemplified above all by the GAIA astrometric mission and many other space-based and ground-based surveys. In the next section (§2), we provide a context for these studies. The Galaxy is then described in terms of traditional components: Galactic Centre (§3), Inner Galaxy (§4), Disk Components (§5) and Halo (§6). Finally, we discuss the likely developments in the near term and attempt to provide some pointers to the future (§7).

## 2. THE GALAXY IN CONTEXT

We glimpse the Galaxy at a moment in time when globally averaged star formation rates (SFR) are in decline and nuclear activity is low. In key respects, the Milky Way is typical of large galaxies today in low density environments (Kormendy et al. 2010), especially with a view to global parameters (e.g. current SFR $\dot{m}_\star$, baryon fraction $f_{\rm bary}$) given its total stellar mass (cf. de Rossi et al. 2009), as we discuss below. But in other respects, it is relatively unusual, caught in transition between the 'red sequence' of galaxies and the 'blue cloud' (Mutch, Croton & Poole 2011). Moreover, unlike M31, our Galaxy has not experienced a major merger for the past 10 Gyr indicating a remarkably quiescent accretion history for a luminous galaxy (Stewart et al. 2008). Most $L_\star$ galaxies lie near the turnover of the galaxy luminosity function where star formation quenching starts to become effective (Benson et al. 2003). But this may not be the last word for the Galaxy: the Magellanic gas stream is evidence for very substantial ($\sim 10^9$ M$_\odot$) and ongoing gas accretion in the present day (Putman et al. 1998; Fox et al. 2014). The Galaxy stands out in another respect: it is uncommon for an $L_\star$ galaxy to be orbited by two luminous dwarf galaxies that are both forming stars (Robotham et al. 2012). None the less, the Galaxy will always be the most important benchmark for galaxy evolution because it provides information that few other galaxies can offer − the fully resolved constituents that make up an $L_\star$ galaxy in the present epoch.

### 2.1. Environment & Evolution

The Galaxy is one of the two dominant members of the Local Group, a low-mass system constituting a loosely bound collection of spirals and dwarf galaxies. The Local Group has an internal velocity dispersion of about 60 km s$^{-1}$ (van den Bergh 1999) and is located in a low-density filament in the far outer reaches of the Virgo supercluster of galaxies (Tully

**Table 2 Global magnitudes, colour indices and mass-to-light ratios for the Galaxy.**

| | | | | | |
|---|---|---|---|---|---|
| Absolute magnitude[a], $M_{\Delta\lambda}$ | $u$ | $g$ | $r$ | $i$ | $z$ |
| | -19.87 | -21.00 | -21.64 | -21.87 | -22.15 |
| | $U$ | $B$ | $V$ | $R$ | $I$ |
| | -20.67 | -20.70 | -21.37 | -21.90 | -22.47 |
| Colour index[b], $(M_{\Delta\lambda_1} - M_{\Delta\lambda_2})$ | $u-r$ | $u-g$ | $g-r$ | $r-i$ | $i-z$ |
| | 1.96 | 1.29 | 0.65 | 0.28 | 0.28 |
| | $U-V$ | $U-B$ | $B-V$ | $V-R$ | $R-I$ |
| | 0.86 | 0.14 | 0.73 | 0.54 | 0.58 |
| Mass-to-light ratio, $\Upsilon^\star$ | $u$ | $g$ | $r$ | $i$ | $z$ |
| | 1.61 | 1.77 | 1.50 | 1.34 | 1.05 |
| | $U$ | $B$ | $V$ | $R$ | $I$ |
| | 1.66 | 1.73 | 1.70 | 1.45 | 1.18 |

Magnitudes and colours derived for the Galaxy from Milky Way analogues drawn from the SDSS survey using the Kroupa initial mass function. All values assume $R_0 = 8.2$ kpc and $R_d = 2.6$ kpc for the Galaxy. [a]The SDSS and Johnson photometry are calibrated (typical errors $\sim$ 0.1 mag) with respect to the AB and Vega magnitude systems, respectively; [b]Different calibration schemes are needed for the SDSS total magnitudes and the unbiassed galaxy colours which leads to inconsistencies between magnitude differences and colour indices (courtesy of Licquia, Newman & Brinchmann 2015).

et al. 2014). Galaxy groups with one or two dominant spirals are relatively common, but close analogues of the Local Group are rare. The presence of an infalling binary pair − the Small and Large Magellanic Clouds (SMC, LMC) − around an $L_\star$ galaxy is only seen in a few percent of cases in the Galaxy and Mass Assembly (GAMA) survey (Driver et al. 2011). This frequency drops to less than 1% if we add the qualification that the massive binary pair are actively forming stars.

With a view to past and future evolution, it is instructive to look at numerical simulations of the Local Group. The Constrained Local Universe Simulations − the CLUES project (www.clues-project.org) − are optimised for a study of the formation of the Local Group within a cosmological context (Forero-Romero et al. 2013; Yepes, Gottlöber & Hoffman 2014). The accretion history of the Local Group is relatively quiet, consistent with its cold internal dynamics. The largest simulations with the most advanced prescriptions for feedback (e.g. FIRE, Hopkins et al. 2014) are providing new insight on why only a small fraction of the dark minihalos in orbit about the Galaxy are visible as dwarf galaxies (Wetzel et al. 2016). But we are still a long way from a detailed understanding of how the dark matter and baryons work together to produce present day galaxies.

The future orbital evolution and merging of the Local Group has been considered by several groups (Cox & Loeb 2008; van der Marel et al. 2012a; Peebles & Tully 2013). These models are being successively refined as proper motions of stars in M31 become available. We learn that the Galaxy and M31 will reach pericentre passage in about 4 Gyr and finally merge in $\sim$6 Gyr. The models serve to remind us that the Galaxy is undergoing at least three strong interactions (LMC, SMC, Sgr) and therefore cannot be in strict dynamical equilibrium (Binney 2013).

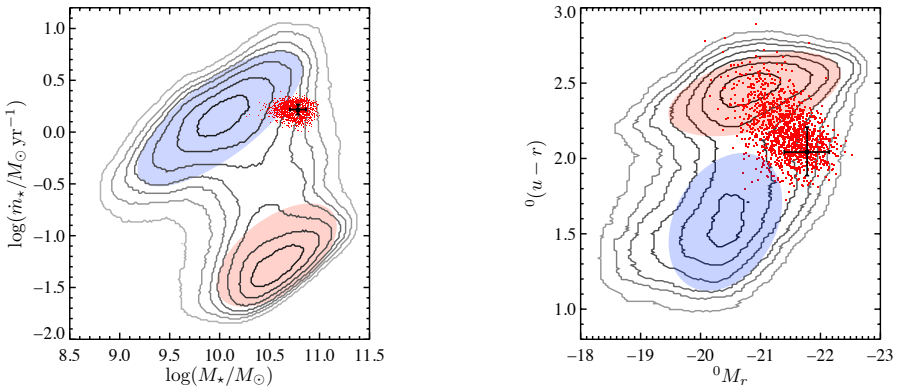


**Figure 3**

Left: Sample of 3500 Milky Way analogues (red dots) drawn from the SDSS survey with the same stellar mass $M_\star$ and star formation rate $\dot{m}_\star$, given the measurement uncertainties. The Galaxy indicated by a cross resides in the 'green valley' just below the 'blue cloud' (see also Mutch, Croton & Poole (2011)). Right: When mapped to absolute magnitude-colour space, the Milky Way analogues are dispersed over a wider region extending into the red sequence. The error bar is noticeably offset from the centre of the distribution due to corrections for inclination reddening and Eddington bias. The increased scatter compared to the left panel is a consequence of the broad range of $g-r$ colours that can correspond to a specific star formation rate. The magnitude and color superscript "0" indicates that the results are corrected to $z=0$. In both figures, the contours indicate the density of galaxies in the projected plane (courtesy of Licquia, Newman & Brinchmann 2015).

## 2.2. Galaxy classification & integrated properties

For most of the last century, galaxy studies made use of morphological classification to separate them into different classes. But high-quality, multi-band photometric and spectroscopic surveys have provided us with a different perspective (Blanton & Moustakas 2009). The bulge to disk ratio, e.g. from Sersic index fitting to photometric images, continues to play an important role in contemporary studies (Driver et al. 2011). Many observed properties correlate with the total stellar mass $M_\star$ and the global star formation rate $\dot{m}_\star$. Galaxies fall into a 'red sequence' where star formation has been largely quenched, and a 'blue cloud' ('main sequence') where objects are actively forming stars, with an intervening 'green valley.' Mutch, Croton & Poole (2011) first established that the Galaxy today appears to fall in the green valley, much like M31 interestingly. Their method is based on the Copernican principle that the Galaxy is unlikely to be extraordinary given global estimates for $M_\star$ and $\dot{m}_\star$. In large galaxy samples, these quantities are expected to correlate closely with photometric properties like absolute magnitude and color index with a scatter of about 0.2 dex. In Fig. 3, we show the results of the most recent analysis of this kind (Licquia, Newman & Brinchmann 2015).

Flynn et al. (2006) recapitulate the long history in deriving Galaxy global properties. Chomiuk & Povich (2011) present an exhaustive study across many wavebands and techniques to arrive at a global star formation rate $\dot{m}_\star$ for the Galaxy. They attempt to unify the choice of initial mass function and stellar population synthesis model across methods,

and find $\dot{m}_\star \approx 1.9$ M$_\odot$ yr$^{-1}$, within range of the widely quoted value of $1-3$ M$_\odot$ yr$^{-1}$ by McKee & Williams (1997). Licquia & Newman (2015) revisit this work and conclude that $\dot{m}_\star = 1.65 \pm 0.19$ M$_\odot$ yr$^{-1}$ for an adopted Kroupa IMF. Likewise, there are many estimates of the Galaxy's total stellar mass, most from direct integration of starlight and an estimate of the mass-to-light ratio, $\Upsilon^\star$(see below). These have largely converged on $M_\star = 6 \pm 1 \times 10^{10}$ M$_\odot$ (§6) for a Galactocentric distance of $R_0 \approx 8.3$ kpc. In §6.4, we estimate a total stellar mass of $M_\star = 5 \pm 1 \times 10^{10}$ M$_\odot$ (and a revised $R_0$) from combining estimates of the mass of the bulge and the disk from dynamical model fitting to stellar surveys and to the Galactic rotation curve.

To transform these quantities into the magnitude system, one method is to select a large set of disk galaxies from the SDSS photometric survey with measured bolometric properties over a spread in inclination and internal extinction. Licquia, Newman & Brinchmann (2015) select possible analogues that match $M_\star$ and $\dot{m}_\star$ in the Galaxy given the uncertainties. In Fig. 3*a*, we present the total absolute magnitudes and unbiassed galaxy colors for the analogues using the SDSS *ugriz* bands; most appear to fall in the green valley, in agreement with Mutch, Croton & Poole (2011). Given these data, the likely values for the Galaxy are presented in Table 2 without the uncertainties. Note the lack of consistency between the quoted SDSS magnitudes and colors because they are derived using different calibration methods as recommended for SDSS DR8 (Aihara et al. 2011), but the differences are mostly below the statistical errors quoted by Licquia, Newman & Brinchmann (2015). In Fig. 3*b*, the analogues show a lot of scatter when transformed to color-magnitude space where the green valley is less well defined. While the Galaxy's location has moved, it still resides in the green valley.

The same inconsistency is seen in the Johnson magnitudes (Table 2) which are derived via color transformations from the SDSS magnitudes (Blanton & Roweis 2007). The `cmodel` and `model` magnitudes in *ugriz* bands are converted to an equivalent set of *UBVRI* magnitudes and color indices respectively (see http://www.sdss.org/dr12/algorithms/magnitudes/#mag_model). This results in small differences between the color derived from single-band absolute magnitudes as opposed to the color inferred from the best SDSS color measurement, but these differences mostly fall below the uncertainties.

For either the SDSS or the Johnson magnitudes, there are no earlier works that cover the five bands; most studies concentrate on $B$ and $V$ (de Vaucouleurs & Pence 1978; Bahcall & Soneira 1980). de Vaucouleurs (1983), updating his earlier work, derived $M_B = -20.2 \pm 0.15$ assuming a distance of $R_0 = 8.5 \pm 0.5$ kpc and a color term $B-V = 0.53 \pm 0.04$, similar to values derived by Bahcall & Soneira (1980): $M_B = -20.1$, $M_V = -20.5$ and $B-V = 0.45$. van der Kruit (1986) took the novel approach of using observations from the *Pioneer* probes en route to Jupiter and beyond to measure optical light from the Galaxy and found $M_B = -20.3 \pm 0.2$ and $B-V = 0.83 \pm 0.15$. These values are mostly dimmer and bluer than the modern values in Table 2. The latter find strong support with the dynamically determined $I$-band values ($M_I = -22.4$, $\Upsilon^\star_I = 1.4$) from Piffl et al. (2014a), and ($M_I = -22.5$, $\Upsilon^\star_I = 1.3$) from Bovy & Rix (2013), and are in close agreement with Flynn et al. (2006).

It is clear from Fig. 3 that the Milky Way is a very luminous, reddish galaxy, somewhat at odds with its traditional classification as an Sb−Sbc galaxy. This has raised questions in the past about where it falls on the Tully-Fisher relation (e.g., Malhotra et al. 1996; Hammer et al. 2012). But this high luminosity is consistent with its high circular velocity ($\sim 240$ km s$^{-1}$) discussed in §6.4. In Table 2, the Galaxy is slightly fainter in *ugriz* absolute magnitude

and slightly less massive in both stellar and baryonic mass than the average for its rotation speed. When considering both the current uncertainties in Milky Way properties and the scatter of galaxies about the relation, the Galaxy is consistent with the Tully-Fisher relation to better than $1\sigma$ uncertainty. The Milky Way appears to be a kinematically typical spiral galaxy for its intrinsic luminosity.

$M_{\Delta\lambda}$: Galaxy absolute magnitude; Table 2

$M_{\Delta\lambda_1} - M_{\Delta\lambda_2}$: Galaxy color index; Table 2

$\Upsilon^{\star}_{\Delta\lambda}$: Galaxy mass-to-light ratio; Table 2

$\dot{m}_{\star}$: $1.65 \pm 0.19$ $M_{\odot}$ $yr^{-1}$; Galaxy total star formation rate

## 3. Galactic Center

### 3.1. Location

The Galactic Center, as we understand it today, was first identified through the discovery of Sgr A by radio astronomers (Piddington & Minnett 1951). Based on its unique radio emission properties and its precise coincidence with the dynamical center of the rotating inner HI disk (Oort & Rougoor 1960), the IAU officially adopted Sgr A as the center of the Galaxy, making its position the zero of longitude and latitude in a new system of Galactic coordinates (Blaauw et al. 1959). Later Balick & Brown (1974) discovered the unresolved source Sgr A*, now known to be at the location of the Milky Way's supermassive black hole, at $(l_c, b_c) = (-0.056°, -0.046°)$ (Reid & Brunthaler 2004).

Thirty years ago, Kerr & Lynden-Bell (1986) gave this working definition of the Galactic Center: *Currently it is assumed that the Galactic Centre coincides sufficiently well with the Galaxy's barycentre that a distinction between the point of greatest star density (or any other central singularity) and the barycentre (centre of mass) is not necessary. It is also assumed that to sufficient accuracy for the internal dynamics of the Galaxy, the Galactic Centre defines an inertial coordinate system. These assumptions could prove to be untrue if for instance the centre of the distribution of the mysterious mass in the heavy halo were displaced from the mass centre of the visible Galaxy.*

Indeed, in a hierarchical universe the first assumption is almost certainly violated beyond tens of kpc: we will see in § 6 that the Galaxy continues to accrete satellite galaxies carrying both stars and dark matter; furthermore, the Milky Way's dark matter halo interacts both with infalling dark matter and with other halos in the Local Group. However, as discussed below, the inner Milky Way appears to have "settled down" to a well-defined and well-centered midplane; thus we may assume that the region of greatest star density coincides with the barycenter of the mass within the Solar Circle.

The second part of the definition may ultimately also come into question. Numerical simulations reveal that dark matter halos tumble at the level of a few radians per Hubble time. The baryonic components are largely bound to the dark matter but may slosh around within them. Furthermore, the spin axis of the Galactic Plane is likely to precess with respect to a celestial coordinate frame defined by distant quasars or radio sources. Over the lifetime of the GAIA mission, this precession ($\sim 30$ $\mu$as $yr^{-1}$) should be detectable (Perryman, Spergel & Lindegren 2014).

**Galactic Center:** Location of radio source Sgr A*

$(l_c, b_c)$: $(-0.056°, -0.046°)$, Galactic coordinates of Sgr A*

**SMBH:** Milky Way's supermassive black hole

### 3.2. Distance

The distance of the Sun to the Galactic Center, $R_0$, is one of the fundamental scaling parameters for the Galaxy. All distances determined from angular sizes or from radial velocities and a rotation model are proportional to $R_0$. Also the sizes, luminosities, and masses of objects such as molecular clouds scale with $R_0$, as do most estimates of global Galactic luminosity and mass. Because $R_0$ is one of the key parameters, we consider its

measured value in some detail here. Previous reviews on this subject can be found in Kerr & Lynden-Bell (1986); Reid (1993); Genzel, Eisenhauer & Gillessen (2010); Gillessen et al. (2013), and a recent compilation of results is given in Malkin (2013).

Similar to their discussion, we divide methods of determining $R_0$ into direct (primary), model-based, and secondary. Direct methods compare an angular dimension or velocity near the Galactic Center with a physical length scale or radial velocity (RV), with minimal modelling assumptions and without having to use additional calibrations. Model-based methods determine $R_0$ as one of the model parameters through a global fit to a set of data. Secondary methods finally use standard candle tracers whose distances are based on secondary calibrations such as period-stellar luminosity relations, and whose distributions are known or assumed to be symmetric with respect to the Galactic Center. In the following, we briefly review the different methods. Table 3 gives the list of independent recent determinations of $R_0$ which we use for obtaining an overall best estimate below.

**3.2.1. Direct estimates.** As discussed more fully in §§3.4, 6.4, the SMBH is at rest at the dynamical center of the Milky Way within the uncertainties (Reid & Brunthaler 2004; Reid 2008). Thus $R_0$ can be determined by measuring the distance to the SMBH's radiative counterpart, Sgr A$^*$. At $\sim$8 kpc distance, the expected parallax of Sgr A$^*$ is $\sim 100\,\mu$as. This would be resolvable with Very Long Baseline Interferometry (VLBI), but unfortunately the image of Sgr A$^*$ is broadened by interstellar scattering (e.g., Bower et al. 2004). However, Reid et al. (2009b) measured trigonometric parallaxes of $H_2O$ masers in Sgr B2, a molecular cloud complex which they estimated is located $\sim$130 pc in front of Sgr A$^*$.

A second direct estimate of the distance to the SMBH comes from monitoring proper motions (PM) and line-of-sight (LOS) velocities for stellar orbits near Sgr A$^*$ (Eisenhauer et al. 2003; Ghez et al. 2008; Gillessen et al. 2009b; Morris, Meyer & Ghez 2012), in particular the star S2 which by now has been followed for a complete orbit around the dynamical center. The main systematic uncertainties are source confusion, tying the SMBH to the astrometric reference frame, and the potential model; relativistic orbit corrections lead to an increase of $R_0$ by $\sim 0.1$ kpc (Genzel, Eisenhauer & Gillessen 2010). See also Gillessen et al. (2009a) who combined the existing two major data sets in a joint analysis.

The statistical parallax of the nuclear star cluster (NSC) obtained by comparing stellar PM and LOS has been used as a third direct estimate of $R_0$ (Genzel et al. 2000; Trippe et al. 2008; Do et al. 2013). This method has now become accurate enough that projection and finite field-of-view effects in combination with orbital anisotropies need to be modelled (Chatzopoulos et al. 2015).

**3.2.2. Model-based estimates.** VLBI astrometry has provided accurate parallaxes and proper motions for over 100 OH, SiO, and Methanol masers in High Mass Star Formation Regions (HMSFR) in the Galactic disk (Honma et al. 2007, 2012; Reid et al. 2009a, 2014; Sato et al. 2010). Most of these sources are located in the Galactic spiral arms. By fitting a spiral arm model together with a model for Galactic circular rotation to the positions and velocities of the HMSFR, precise estimates of $R_0$ can be obtained together with rotation curve and other parameters (for a different analysis, see Bajkova & Bobylev 2015). Because distances are determined geometrically, no assumptions on tracer luminosities or extinction are necessary. The main remaining systematic uncertainties thus are the assumption of axisymmetric rotation, the detailed parametrisation of the rotation curve model, and the treatment of outliers.

Another long-standing approach is based on analyzing the velocity field near the Solar Circle, using PM and LOS velocities of various tracers. These methods assume an axisymmetric velocity field and, in some cases, include the perturbing effects of a spiral arm model. In the traditional form, the data are used to solve for the Oort constants A, B (§6.4) from the PMs and for $2AR_0$ from the RVs, to finally estimate $R_0$ (Mihalas & Binney 1981; Zhu & Shen 2013). Another variant is to use young stars or star formation regions assumed to follow circular orbits precisely (Sofue et al. 2011; Bobylev 2013). An analysis less sensitive to the uncertain perturbations from spiral arms and other substructure is that by Schönrich (2012), who uses a large number of stars with PMs and RVs from the SEGUE survey (Yanny et al. 2009), to determine $R_0$ by combining the rotation signals in the radial and azimuthal velocities for stars within several kpc from the Sun.

A promising new method is based on the detailed dynamical modelling of halo streams. While stream modelling has mostly been used to obtain estimates for the mass and shape of the dark matter halo (see § 6.3), Küpper et al. (2015) showed that with accurate modelling $R_0$ can also be well-constrained as part of a multi-parameter fit to detailed density and LOS velocity measurements along the stream.

Vanhollebeke, Groenewegen & Girardi (2009) compared predictions from a stellar population model for the Galactic bulge and intervening disk to the observed star counts. They used a density model based on NIR data from Binney, Gerhard & Spergel (1997) and varied the star formation history and metallicity distribution of bulge stars. The value of $R_0$ from their best fitting models depends heavily on the magnitudes of red clump stars, showing a close connection to secondary methods.

**3.2.3. Secondary estimates.** There is a long history of secondary $R_0$ measurements based on the distance distributions of RR Lyrae stars, Cepheids, Mira stars, red clump giants (RCG), and globular clusters (Reid 1993). Individual distances are derived from external calibrations of period-luminosity (PL) relations for the variable stars, and from horizontal branch (HB) magnitudes for RCG and globular clusters. The main systematic errors in these methods come from uncertainties in the calibrations, but also from the extinction corrections and reddening law, and from how the distance distribution in the survey volume is related to the center of the Galaxy.

RR Lyrae, pulsationally unstable HB stars with characteristic absolute magnitudes $M_I = 0.2$, $M_K = -0.5$ (Catelan, Pritzl & Smith 2004), are the primary distance tracers for old, metal-poor populations. Large numbers of RR Lyrae stars identified by the OGLE (Udalski et al. 2008) and VVV surveys (Minniti et al. 2010) were recently used to map out the old metal-poor population in the bulge (Pietrukowicz et al. 2015; Dékány et al. 2013, respectively). Individual distances are more accurate by a factor $\sim 2$ in the NIR than in optical data, due to higher precision and reduced metallicity dependence in the PL-relation, and less sensitivity to reddening. With the large bulge samples the centroid of the distribution can be determined more accurately than in earlier work (e.g., Groenewegen 2008; Majaess 2010). On larger Galactic scales, Dambis (2009) calibrated thick disk and halo RR Lyrae populations separately by statistical parallax to then estimate $R_0$.

Type II Cepheids trace old, typically metal-poor populations; they are brighter than RR Lyrae stars but much less numerous. Groenewegen (2008) used NIR data for 39 population II Cepheids in the bulge from the OGLE survey; a related work is by Majaess (2010). Matsunaga et al. (2011, 2013) analysed 3 classical Cepheids and 16 type II Cepheids from a NIR survey of the inner $\sim 30$ pc in the nuclear bulge.

**Table 3 Recent measurements of distance $R_0$ to Galactic Center**

| Label | Reference | Method | Loc | T | $R_0$ [kpc] |
|---|---|---|---|---|---|
| Rd+09 | Reid et al. 2009 | Trig. Parallax of Sgr B | GC | d | $7.90 \pm 0.75$ |
| Mo+12 | Morris et al. 2012 | Orbit of S0-2 around Sgr A* | GC | d | $7.70 \pm 0.40$ |
| Gi+09 | Gillessen et al. 2009 | Stellar orbits around Sgr A* | GC | d | $8.33 \pm 0.35$ |
| Ch+15 | Chatzopoulos et al. 2015 | NSC statistical parallax | GC | d | $8.27 \pm 0.13$ |
| Do+13 | Do et al. 2013 | NSC statistical parallax | GC | d | $8.92 \pm 0.56$ |
| BB15 | Bajkova & Bobylev 2015 | Trig. Parallaxes of HMSFRs | DSN | m | $8.03 \pm 0.32$ |
| Rd+14 | Reid et al. 2014 | Trig. Parallaxes of HMSFRs | DSN | m | $8.34 \pm 0.19$ |
| Ho+12 | Honma et al. 2012 | Trig. Parallaxes of HMSFRs | DSN | m | $8.05 \pm 0.45$ |
| ZS13 | Zhu & Shen 2013 | Near-R0 rotation yg tracers | DSN | m | $8.08 \pm 0.62$ |
| Bo13 | Bobylev 2013 | Near-R0 rotation SFRs+Cephs | DSN | m | $7.45 \pm 0.66$ |
| Sch12 | Schönrich 2012 | Near-R0 rotation SEGUE stars | DSN | m | $8.27 \pm 0.41$ |
| Ku+15 | Küpper et al. 2015 | Tidal tails of Pal-5 | IH | m | $8.30 \pm 0.35$ |
| VH+09 | Vanhollebeke et al. 2009 | Bulge stellar popul. model | B | m | $8.70 \pm 0.50$ |
| Pi+15 | Pietrukowicz et al. 2015 | Bulge RR Lyrae stars | B | s | $8.27 \pm 0.40$ |
| De+13 | Dekany et al. 2013 | Bulge RR Lyrae stars | B | s | $8.33 \pm 0.15$ |
| Da09 | Dambis 2009 | Disk/Halo RR Lyrae stars | DSN | s | $7.58 \pm 0.57$ |
| Ma+13 | Matsunaga et al. 2013 | Nuclear bulge T-II Cepheids | B | s | $7.50 \pm 0.60$ |
| Ma+11 | Matsunaga et al. 2011 | Nuclear bulge Cepheids | B | s | $7.90 \pm 0.36$ |
| Gr+08 | Groenewegen et al. 2008 | Bulge Cepheids | B | s | $7.98 \pm 0.51$ |
| Ma+09 | Matsunaga et al. 2009 | Bulge Mirae | B | s | $8.24 \pm 0.43$ |
| GrB05 | Groenewegen & Bl. 2005 | Bulge Mirae | B | s | $8.60 \pm 0.81$ |
| FA14 | Francis & Anderson 2014 | Bulge red clump giants | B | s | $7.50 \pm 0.30$ |
| Ca+13 | Cao et al. 2013 | Bulge red clump giants | B | s | $8.20 \pm 0.20$ |
| Fr+11 | Fritz et al. 2011 | NSC red clump giants | GC | s | $7.94 \pm 0.76$ |
| FA14 | Francis & Anderson 2014 | All globular clusters | BIH | s | $7.40 \pm 0.28$ |
| Bi+06 | Bica et al. 2006 | Halo globular clusters | IH | s | $7.10 \pm 0.54$ |

Recent determinations of the distance to the Galactic Center, $R_0$, used for weighted averages and in Fig. 4. Columns give label for Fig. 4, reference, location (Galactic Center, bulge, disk and solarneighbourhood, inner halo), type of measurement (direct, model-based, secondary), $R_0$. The listed uncertainties include statistical and systematic errors, added in quadrature when both are published. Where a systematic error is not quoted by the authors or included in their total published error, we estimated it from results obtained by them under different assumptions, when possible (GrB05, Fr+11, BB15, Rd+14, Bo13, Bi+06). For Ca+13 who did not give an error, we estimated one from the metallicity dependence of the RCG calibration of Nataf et al. (2013). In the remaining cases (ZS13, Sch12, Kue+15, Da09) we took the systematic error to be equal to the statistical error.

Groenewegen & Blommaert (2005) obtained a PL relation for 2691 Mira long period variables in the OGLE bulge fields while Matsunaga et al. (2009) studied 100 Miras in the nuclear bulge. For these red giants the extinction corrections are smaller, but calibrations from the Large Magellanic Cloud (LMC) and globular clusters were needed to estimate $R_0$ from these data.

Since the work of Paczynski & Stanek (1998), red clump giants (RCG) have been recognized as important distance probes in the Galaxy (see Girardi, this volume). RCG are He-core burning stars with a narrow range of luminosities, especially in medium-to-old age populations such as in the Galactic bulge. Typical absolute magnitudes are $M_I = -0.5$, $M_K = -1.6$, with a dispersion $\sim$0.1-0.2 mag, and systematic effects due to age and metallicity variations are relatively small and fairly well understood. Surveys towards the inner

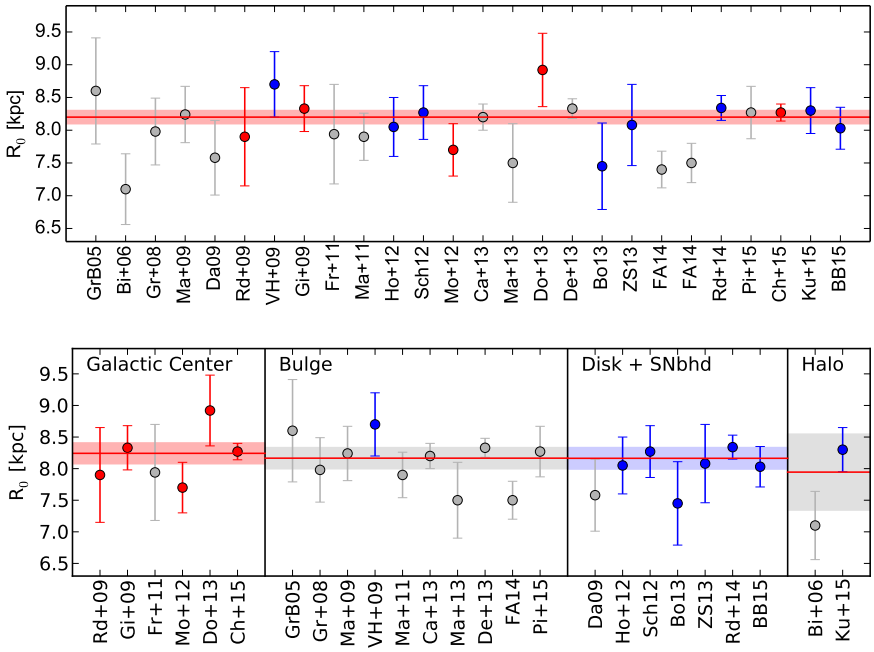


**Figure 4**

Recent measurements of $R_0$ from Table 3, using different methods. Red, blue, and grey points denote direct, model-based, and secondary estimates. Top: time sequence for all, with our adopted best estimate, $R_0 = 8.2 \pm 0.1$ kpc. Bottom: separate time-sequences for determinations in the Galactic Center, bulge, disk and solar neighbourhood, and inner halo (not using the FA14 globular cluster value which includes the inner metal-rich clusters). The horizontal lines show weighted mean values for the respective components, and colored bands show $1\sigma$ UUE-errors. See text for details.

Galaxy are frequently done in the NIR to minimize extinction (Babusiaux & Gilmore 2005; Nishiyama et al. 2006) or in the $I$-band (Paczynski & Stanek 1998; Nataf et al. 2013). The $K$-band studies tend to give slightly shorter distances. Fritz et al. (2011) used RCG in several NIR bands to determine a distance to the central NSC.

The centroid of the distance distribution of globular clusters, the basis for the famous early work by Shapley (1918), continues to be used for estimating $R_0$ (Bica et al. 2006; Francis & Anderson 2014). These studies are based on the catalogue of Harris (2010, and earlier), where individual distances are estimated from HB magnitudes and reddening. The distance distribution of the clusters is somewhat asymmetric, and $R_0$ values found are on the low side of the distribution in Table 3. Systematic effects could be due to missing clusters behind the Galactic Center, or to errors in the HB magnitudes, e.g., from extinction uncertainties or stellar confusion in crowded cluster fields (Genzel, Eisenhauer & Gillessen 2010). However, the method provides a rare opportunity to estimate $R_0$ from Galactic halo tracers.

**3.2.4. Overall best estimate and discussion.** Table 3 gives the list of recent determinations which we use for obtaining an overall best estimate for $R_0$. For each method we kept at

most three determinations to prevent overweighting often-employed techniques with similar systematic uncertainties; for example, there are many determinations of $R_0$ using RCG as standard candles. We omitted determinations which were later updated by the same group of authors based on improved data, but kept independent reanalyses of published data by other authors. We also did not include $R_0$ estimates which used priors based on measured values already taken into account (e.g. McMillan 2011).

Fig. 4 shows the overall distribution of these 26 measurements with time, and the separate distributions for tracers in the Galactic Center, bulge, disk, and halo, respectively. To obtain a best estimate for $R_0$, we consider weighted means for the total and various subsamples. For any $N_m$ measurements, we compute (i) the standard error of the weighted mean, SE; (ii) the unbiassed standard error of the weighted mean (UE, square root of $1/N_m$ times the unbiassed weighted sample variance); (iii) following Reid (1993), we consider possible correlations between some of the measurements. These can arise, e.g., because HB or PL calibrations use very similar theoretical models or calibrators, or are based on a common LMC distance; because two data sets, although independent, can only be obtained for the same small number of stars; or because several measurements are all based on the assumption that the velocity field near the Solar Circle is axisymmetric. Clearly, some of these correlations have stronger influence than others. For a conservative error evaluation, we retain $N_{uc} = 11$ independent measurements for the total sample, and $N_{uc} = (4, 4, 3, 2)$ for the separate (GC, B, DSN, IH) tracer samples. We note that the sets of methods kept for the different regions are largely independent. In each case, we determine a UUE uncorrelated sample error by replacing $N_m$ in UE by $N_{uc}$.

Using the notation $R_0 \pm \mathrm{UUE}[\mathrm{UE}, \mathrm{SE}]$, we find $R_0 = 8.14 \pm 0.10\ [0.07, 0.06]$ kpc for the total sample; $R_0 = 8.17 \pm 0.12\ [0.09, 0.07]$ kpc for measurements 2013 or later; $R_0 = 8.29 \pm 0.03[0.03, 0.08]$ kpc for the 4 measurements with errors $\leq 0.2$ kpc (Ch+15, Rd+14, De+13, Ca+13); $R_0 = 8.22 \pm 0.07\ [0.07, 0.07]$ kpc for the 11 uncorrelated best determinations; $R_0 = 8.21 \pm 0.08\ [0.05, 0.06]$ kpc excluding the 2 values outside their $(2\sigma)$ of the overall weighted mean; and $R_0 = 8.19 \pm 0.08[0.06, 0.06]$ kpc for all values excluding halo. All data samples give very consistent results; the fact that SE and UE generally agree within $\sim$20% suggests that the errors given for the individual $R_0$ measurements are mostly realistic. Based on the scatter and UUE errors of the various sample means, we adopt here our best estimate for the distance to the Galactic Center: $R_0 = 8.2 \pm 0.1$ kpc. This value is significantly lower than the IAU standard ($R_0 = 8.5$ kpc).

The weighted sample means for tracers in the different regions of the Galaxy are $R_0 = 8.24 \pm 0.16\ [0.13, 0.11]$ kpc for the GC sample, $R_0 = 8.17 \pm 0.17\ [0.11, 0.09]$ kpc for the B sample, $R_0 = 8.16 \pm 0.17\ [0.11, 0.13]$ kpc for the DSN sample, and $R_0 = 7.95 \pm 0.60\ [0.60, 0.29]$ kpc for the IH sample. The fact that tracers in the Galactic Center, bulge, and disk result in similar estimates for $R_0$ within small errors (also for UUE with largely independent respective methods) suggests that the different Galactic components are well-centered, and thus that relative sloshing motions between these components must currently be unimportant. Together with the good alignment of the Milky Way bar and HI disk with the Galactic plane (§ 3.3), this suggests that the inner Milky Way has settled to a well-determined equilibrium state. Even the inner halo tracers on scales of $10 - 20$ kpc are consistent with having the same Galactic Center as the bulge and disk, within $\sim$0.6 kpc error.

We anticipate significant improvements in many of these distance measurements based on data from the GAIA satellite, which will provide accurate parallaxes and proper motions for large numbers of Milky Way stars. These data will greatly improve our dynamical

understanding of the Galactic disk, but also of the bulge and bar outside highly extincted regions, and lead to much-improved secondary calibrations, e.g., for RR Lyrae and RCG. The direct estimate of $R_0$ from stellar orbits around Sgr A$^*$ is expected to improve steadily as the time base line increases and more orbits can be reliably constrained, and especially with accurate astrometric and spectroscopic monitoring of the next close pericenter passage (2018 for the star S2).

$R_o$: $8.2 \pm 0.1$ kpc, Sun's distance from Galactic Center

$z_0$: $25 \pm 5$ pc, solar offset from local disk midplane

### 3.3. Solar offset and Galactic plane

Early estimates of the Sun's vertical position with respect to the Galactic Plane date back to van Tulder (1942)'s analysis of stellar catalogues, from which was determined $z_0 = 14 \pm 2$ pc towards the North Galactic pole. In support of the early value, Conti & Vacca (1990) obtained $z_0 = 15 \pm 3$ pc using 150 Wolf-Rayet stars within 20 kpc of the Sun. PIONEER 10 observations of the optical background light in the Galaxy indicated $z_0 = 13 \pm 3$ pc (Toller 1990), and modeling the COBE NIR surface brightness distribution resulted in $z_0 = 14 \pm 4$ pc (Binney, Gerhard & Spergel 1997).

But more expansive studies of the nearby disk show that these are underestimates. Chen et al. (2001) demonstrated the importance of correctly treating the larger-scale parameters of the disk population in such studies, using the SDSS photometric survey. While the radial scalelength is relatively unimportant, a vertically extended population with a well established scaleheight is critical. The following estimates are based on either OB stars, open clusters, or optical star counts for a range of stellar populations, and are broadly consistent: $z_0 = 24 \pm 3$ pc (Stothers & Frogel 1974); $z_0 = 28 \pm 5$ pc (Pandey, Bhatt & Mahra 1988); $z_0 = 21 \pm 4$ pc (Humphreys & Larsen 1995); $z_0 = 27 \pm 3$ pc (Mendez & van Altena 1998); $z_0 = 28 \pm 6$ pc (Chen et al. 1999); $z_0 = 27 \pm 4$ pc (Chen et al. 2001); $z_0 = 24 \pm 2$ pc (Maíz-Apellániz 2001). While the last estimate from HIPPARCOS OB stars has the smallest error, the distribution of young stars may be more sensitive to various perturbations, as illustrated by Gould's belt. Therefore we adopt here the best estimate from the complete SDSS photometric survey, i.e. $z_0 = 25 \pm 5$ pc (Jurić et al. 2008), which captures all these values.

The Galactic midplane was defined based on the very flat distribution of HI gas in the inner Galaxy, with an estimated uncertainty in the position of the Galactic pole of $\sim 0.1^\circ$ (Blaauw et al. 1960). Because the Sun was found to lie in the HI principal plane within the errors, and the measured offset relative to Population I stars was not considered reliable, the $b = 0$ plane was defined to pass through the Sun and Sgr A (not Sgr A$^*$). Since we know now that $z_0 \simeq 25$ pc, the true Galactic plane is likely to be slightly inclined relative to the plane $b = 0$. If it is assumed that Sgr A$^*$ lies precisely in the Galactic plane (see § 3.4), the required inclination angle is $\simeq 0.13^\circ$ (see Fig. 5 and Goodman et al. 2014). Objects located in the Galactic plane between the Sun and the Galactic Center then appear at slightly negative latitudes. Near-infrared star counts in the inner Galaxy have enough signal-to-noise to detect such offsets. The mean latitude of the peak of RCG counts in the Galactic long bar (see § 4.3) is indeed found at $b \simeq -0.12^\circ$, corresponding to an offset of 14 pc at $\sim 6$ kpc distance (Wegg, Gerhard & Portail 2015). The observed peak latitudes agree with those predicted for the inclined plane to within $\sim 5$ pc or $\sim 0.1\%$ of the half-length of the bar (Fig. 5). The Galactic long bar is thus consistent with lying in a tilted midplane passing through Sgr A$^*$ and the point $z_0 = 25$ pc below the Sun to within $\sim 0.1\%$. Both stars and HI gas suggest that the Galactic disk inside the Solar Circle is very nearly flat.

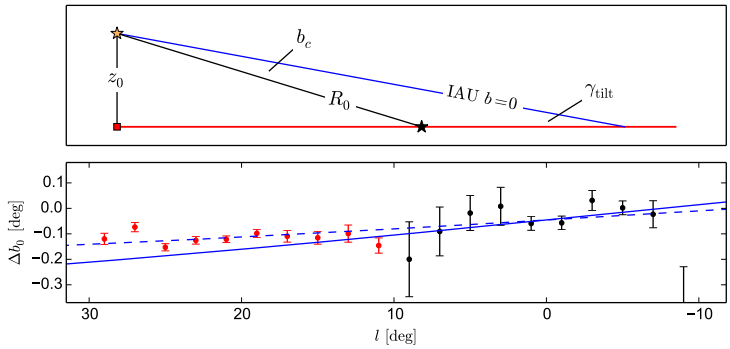


**Figure 5**

Top: illustration of the tilt of the true Galactic disk plane (red) vs. the $b=0-$plane (blue), as predicted from solar offset $z_0$ and assuming that the true plane passes through Sgr A* (black star); after Goodman et al. (2014). Bottom: measured offsets $\Delta b_0$ of bulge (black) and long bar (red) peak starcounts from the $b=0-$plane. The full line shows the predicted offsets for a one-dimensional bar with bar angle 27° (§4), lying precisely in the true Galactic plane defined by $z_0=25$ pc, $R_0=8.2$ kpc, and $b_c=-0.046°$, so that $\gamma_{\rm tilt}=0.13°$. The dashed line is obtained when assuming an additional rotation of the true plane around the Sun-Galactic Center line by 0.14°. Deviations from the plane in the long bar region are less than $\sim 0.05° \simeq 5$ pc, of order 0.1% of the length of the long bar. Adapted from Wegg, Gerhard & Portail (2015); see also §4.3.

## 3.4. Black hole and solar angular velocity

Measurements in the Milky Way have provided the best evidence for a central SMBH to date; see Reid (2009) and Genzel, Eisenhauer & Gillessen (2010) for recent reviews. Infrared studies of the motions of gas clouds in the Sgr A region first indicated a central point mass of several $10^6\ M_\odot$ (e.g., Lacy et al. 1980). Later, PM measurements of stars in the dense NSC showed evidence for a Keplerian increase of the stellar velocity dispersion to several 100 km s$^{-1}$ at $\sim 0.01$ pc of the Galactic Center, corresponding to a central mass of $\sim 2-3\times 10^6\ M_\odot$ (Eckart & Genzel 1997; Ghez et al. 1998). Currently, from accurate LOS velocities and astrometric measurements with adaptive optics, stellar orbits have been determined for some 30 of the so-called S-stars in the central arcsec, including one complete 15.8 year orbit for the star S2. All orbits are well-fitted by a common enclosed mass and elliptical orbit focal point. From multi-orbit fits, rescaled to $R_0=8.2$ kpc, the total enclosed mass is $M_\bullet = 4.3\times 10^6\ M_\odot$ (Ghez et al. 2008) and $M_\bullet = 4.2\times 10^6\ M_\odot$ (Gillessen et al. 2009b), and $M_\bullet = (4.20\pm 0.36)\times 10^6\ M_\odot$ from a joint analysis of the combined VLT and Keck data (Gillessen et al. 2009a). The error given is combined statistical and systematic and is expected to improve steadily with increasing time baseline of the measurements; it has an important contribution from a degeneracy between $M_\bullet$ and $R_0$.

Therefore, external constraints on $R_0$ reduce the range of black hole mass allowed by the orbit measurements. Combining with their measurement of the NSC statistical parallax, Chatzopoulos et al. (2015) found $M_\bullet = (4.23\pm 0.14)\times 10^6\ M_\odot$. Using instead the overall best $R_0=8.2\pm 0.1$ kpc from §3.2, the mass of the black hole becomes $M_\bullet = (4.2\pm 0.2\times 10^6)\ M_\odot$. This corresponds to a Schwarzschild radius of $\sim 0.1$ AU, and to a dynamical radius of influence $r_{\rm infl}\simeq 3.8$ pc, where the interior mass of the NSC $M(r<r_{\rm infl})=2M_\bullet$ (Chatzopoulos et al. 2015). The inferred mass is also consistent with the orbital roulette value obtained

by Beloborodov et al. (2006) from the stellar motions in the clockwise disk of young stars around Sgr A*. For $M_\bullet = 4.2 \times 10^6\ M_\odot$ and a bulge velocity dispersion of $\sigma \simeq 113$ km s$^{-1}$ (§4.2.3), the Milky Way falls below the best-fitting $(M_\bullet - \sigma)-$relation for elliptical galaxies and classical bulges by a factor of ∼5-6 (Kormendy & Ho 2013; Saglia et al. 2016).

From the orbit fit, any extended mass distribution within the orbit of S2 can contribute no more than 10% of the enclosed mass. The S2 star has approached the central mass within 125 AU at pericenter, requiring a minimum interior mass density of $\rho_\bullet(< 125\,\mathrm{AU}) = 5 \times 10^{15}\,\mathrm{M}_\odot\,\mathrm{pc}^{-3}$. This is so large that one can rule out any known form of compact object other than a black hole (Reid 2009; Genzel, Eisenhauer & Gillessen 2010). From matching the positions of SiO maser stars visible both in the NIR and the radio, the position of the compact mass and the radio source Sgr A* have been shown to coincide within ∼2mas = 16 AU (Reid et al. 2003; Gillessen et al. 2009b). The size of Sgr A* in mm radio observations is < 1 AU (Shen et al. 2005; Doeleman et al. 2008). These facts taken together make it highly likely that Sgr A* is the radiative counterpart of the black hole at the center of the Galaxy.

The apparent PM of Sgr A* relative to a distant quasar (J1745-283) has been measured with great precision using VLBI (Reid & Brunthaler 2004; Reid 2008). The PM perpendicular to the Galactic plane is entirely consistent with the reflex motion of the vertical peculiar velocity of the Sun, with residual $-0.4 \pm 0.9$ km s$^{-1}$, suggesting strongly that the SMBH is essentially at rest at the Galactic Center. Indeed the Brownian motion of the SMBH due to perturbations from the stars orbiting inside its gravitational influence radius is expected to be ∼ 0.2 km s$^{-1}$ (Merritt, Berczik & Laun 2007). On the assumption that Sgr A* is motionless at the Galactic Center, its measured PM in the Galactic plane determines the total angular velocity of the Sun with high accuracy: $\Omega_{g,\odot} = 30.24 \pm 0.12$ km s$^{-1}$kpc$^{-1}$. For $R_0 = 8.2 \pm 0.1$ kpc from §3.2, the inferred value of the total solar tangential velocity relative to the Galactic Center is $V_{g,\odot} = 248 \pm 3$ km s$^{-1}$. We will return to these constraints in our discussion of the Galactic rotation curve in §6.4 which brings together many of the major themes of this review.

$M_\bullet$: $(4.2 \pm 0.2 \times 10^6)\ M_\odot$, mass of Galactic SMBH

$\rho_\bullet(< 125\,\mathrm{AU})$: $5 \times 10^{15}\ M_\odot\,\mathrm{pc}^{-3}$, mass density within pericenter of star S2

$r_{\mathrm{infl}}$: 3.8 pc, SMBH's dynamical influence radius

$\Omega_{g,\odot}$: $30.24 \pm 0.12$ km s$^{-1}$kpc$^{-1}$, Sun's total angular velocity relative to Sgr A*

$V_{g,\odot}$: $248 \pm 3$ km s$^{-1}$, Sun's tangential velocity relative to Sgr A*

## 4. Inner Galaxy

### 4.1. Nuclear star cluster and stellar disk

Becklin & Neugebauer (1968) discovered an extended NIR source centered on Sgr A: the MW's nuclear star cluster (NSC). The source has a diameter of $\sim 5' \simeq 2.4$ pc, is elongated along the Galactic plane, and its surface brightness falls with projected radius on the sky $\propto R_s^{-0.8\pm0.1}$. NSC are commonly seen in the centers of disk galaxies and many contain an AGN and thus a SMBH (e.g. Böker 2010). NIR spectroscopy has shown that most of the luminous stars in the Galactic NSC are old (> 5 Gyr) late-type giant and RCG stars (the "old" NSC, Pfuhl et al. 2011). But also a surprising number of massive early-type stars were found in this volume (Krabbe et al. 1995), including massive young stars in one and possibly two disks with diameters 1′-2′ rotating around the SMBH (Paumard et al. 2006; Bartko et al. 2009), and a remarkable concentration of B-stars within 1" of the SMBH, the so-called S-stars (Eckart et al. 1995). Recent reviews on the NSC can be found in Genzel, Eisenhauer & Gillessen (2010) and Schödel et al. (2014b).

The structure and dynamics of the NSC must be studied in the IR because of the very high extinction towards the GC ($A_K \sim 2.6$ mag, $A_V \sim 40$ mag, Fritz et al. 2011; Nishiyama et al. 2008). Recent analysis of SPITZER/IRAC 3.6 $\mu$m/4.5 $\mu$m images (Schödel

**NSC:** Nuclear star cluster

$L_{4.5,\mathrm{NSC}}$: $(4.1 \pm 0.4) \times 10^7 L_\odot$, NSC Luminosity

$r_{\mathrm{NSC}}$: $4.2 \pm 0.4$ pc, half-light radius

$c/a$: $= 0.71 \pm 0.04$, axis ratio

$M_{\mathrm{NSC}}$: $= (1.8 \pm 0.3) \times 10^7\ M_\odot$, NSC mass

et al. 2014a) has shown that the old NSC is centered on Sgr A$^*$ and point-symmetric, and it is flattened along to the Galactic plane with minor-to-major projected axis ratio $q = 0.71 \pm 0.02$. Chatzopoulos et al. (2015) obtain $q = 0.73 \pm 0.04$ from fitting K-band star counts; they also show that NSC dynamics requires a flattened star cluster with an axis ratio consistent with this value. The NSC radial density profile is discussed in these papers and in Fritz et al. (2014). When fitting the 4.5 $\mu$m data with a Sersic profile, Schödel et al. (2014a) obtain a total 4.5 $\mu$m luminosity $L_{4.5,\mathrm{NSC}} = (4.1 \pm 0.4) \times 10^7 L_\odot$ and a spherical half-light radius of $r_h = 4.0 \pm 0.4$ pc.

The dynamical mass within 100" = 4 pc is $(8.9 \pm 1) \times 10^6\ M_\odot$ (Chatzopoulos et al. 2015); thus $M/L_{4.5} = 0.44 \pm 0.06\ M_\odot/L_{4.5,\odot}$ and the total mass of the NSC for the Sersic model is $M_{\mathrm{NSC}} = (1.8 \pm 0.3) \times 10^7\ M_\odot$. An additional error in $M_{\mathrm{NSC}}$ not accounted for in this estimate comes from the fact that the surface density profile of the NSC goes below that of the much larger, surrounding nuclear stellar disk at projected $R_s \gtrsim 100$", making its outer density profile uncertain (Chatzopoulos et al. 2015). The rotation properties and velocity dispersions were measured by Trippe et al. (2008); Fritz et al. (2014) from stellar PM and LOS velocities, and from NIR integrated spectra by Feldmeier et al. (2014). The NSC is approximately described by an isotropic rotator model, with slightly slower rotation (Chatzopoulos et al. 2015). There are indications for a local kinematic misalignment in the LOS velocities but not in the PM (Feldmeier et al. 2014; Fritz et al. 2014) which, if confirmed, might indicate some contribution to the NSC mass by infalling star clusters (Antonini et al. 2012); this needs further study. Another unsolved problem is the apparent core in the NSC density profile (Buchholz, Schödel & Eckart 2009); this might indicate that the NSC is not fully relaxed, consistent with the relaxation time estimated as $\approx 10$ Gyr throughout the NSC (Merritt 2013).

The old NSC is embedded in a nuclear stellar disk (NSD) which dominates the three-dimensional stellar mass distribution outside $\sim 30$ pc (Chatzopoulos et al. 2015) and within $\sim 200 - 400$ pc (Launhardt, Zylka & Mezger 2002). From star counts, its vertical density profile is near-exponential with scale-height $h_{\mathrm{NSD}} \simeq 45$ pc (Nishiyama et al. 2013). This confirms an earlier analysis of COBE data by Launhardt, Zylka & Mezger (2002) which cover a larger area but with lower resolution. The projected density profile along the major axis ($|l|$) is approximately a power-law $\propto |l|^{-0.3}$ out to $\sim 90$ pc; thereafter it drops steeply towards the NSD's outer edge at $\sim 230$ pc, approximately $\propto |l|^{-2}$. The axis ratio of the NSD inferred in these papers from the star counts and NIR data is $\sim 3$:1 at small radii and $\sim 5$:1 on the largest scale. The total stellar mass estimated by Launhardt, Zylka & Mezger (2002) is $M_{\mathrm{NSD}} = (1.4 \pm 0.6) \times 10^9\ M_\odot$, of order 10% of the mass of the bulge. The rotation of the NSD has been seen in OH/IR stars and SiO masers (Lindqvist, Habing & Winnberg 1992; Habing et al. 2006) and with APOGEE stars (Schönrich, Aumer & Sale 2015), with an observed gradient $\approx 150$ km s$^{-1}$/deg and estimated rotation velocity $\approx 120$ km s$^{-1}$ at $R \simeq 100$ pc. These data suggest a dynamical mass on the lower side of the estimated stellar mass range. The NSD is likely related to past star formation in the zone of $x_2$-orbits near the center of the barred potential (e.g. Molinari et al. 2011). Clearly, understanding the NSD better is relevant for the evolution of the Galactic bulge and probably also for the growth of the SMBH, and further information about its kinematics and stellar population would be important. Figure 6 illustrates this still enigmatic Galactic component together with the NSC.

**NSD:** Nuclear stellar disk

$r_{\mathrm{NSD}}$: $\simeq 90$ pc, NSD break radius

$h_{\mathrm{NSD}}$: 45 pc, NSD vertical scale-height

$M_{\mathrm{NSD}}$: $(1.4 \pm 0.6) \times 10^9\ M_\odot$, stellar mass of NSD

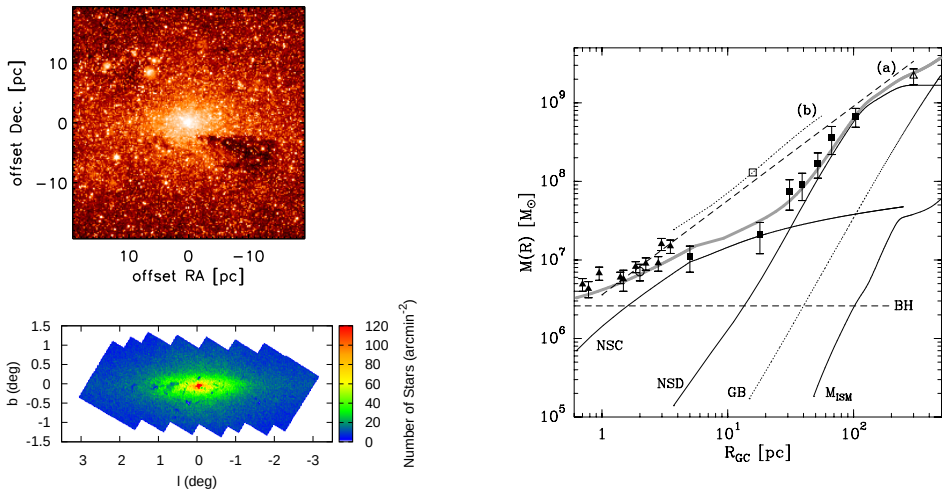


**Figure 6**

Top left: extinction-corrected 4.5 $\mu$m IRAC image of the NSC from Schödel et al. (2014a). Bottom left: extinction-corrected star count map of the NSD from Nishiyama et al. (2013). The scale is 143 pc/deg at $R_0 = 8.2$ kpc. The NSC is seen as the red dot in the center of this image. Right: enclosed photometric mass within spherical radius for the NSC, NSD, Galactic bulge (GB), and total (thick line) from Launhardt, Zylka & Mezger (2002), with mass measurements at the time overplotted as points with error bars.

## 4.2. Bulge

For many years, the Galactic bulge was considered as a structure built through mergers early in the formation of the Galaxy, now called a *classical bulge*. Particularly the old ages of bulge stars inferred from color-magnitude diagrams supported this view (Ortolani et al. 1995; Clarkson et al. 2008). The NIR photometry with the DIRBE instrument on board the COBE satellite first established the boxy nature of the bulge (Weiland et al. 1994; Binney, Gerhard & Spergel 1997), later confirmed by the 2MASS star count map (Skrutskie et al. 2006). Recent star count data have unambiguously established that the bulk of the bulge stars are part of a so-called *box/peanut or b/p-bulge* structure representing the inner, three-dimensional part of the Galactic bar (McWilliam & Zoccali 2010; Nataf et al. 2010; Wegg & Gerhard 2013), consistent with the observed cylindrical rotation (Kunder et al. 2012; Ness et al. 2013b). This corroborates long-standing evidence for a barred potential in the bulge region from non-circular motions seen in HI and CO longitude-velocity-($lv$)-diagrams (Binney et al. 1991; Englmaier & Gerhard 1999). The central parts of the Galaxy also contain the dense NSD and some have argued for a separate, 200 pc-scale *nuclear bar* (Alard 2001; Rodriguez-Fernandez & Combes 2008). Finally, the peak in the density of the *inner stellar halo* is found in this region as well. Disentangling these various components clearly requires the best data possible. Results to date and open issues are summarized below. More extensive reviews of the Galactic bulge can be found in Rich (2013); Gonzalez & Gadotti (2016); Shen & Li (2015).

**4.2.1. The Galactic b/p bulge.** A large fraction of the bulge stars follows a rotating, barred, box/peanut shaped bulge with exponential density distribution, similar to the inner three-dimensional part of an evolved N-body bar. The best available structural information for the dominant bulge population comes from large samples of red clump giant stars (RCG), for which individual distances can be determined to $\sim$10% accuracy. These He-core burning stars have a narrow range of absolute magnitudes and colors, $\sigma(\mathrm{K}_s) \simeq 0.17$ and $\sigma(\mathrm{J}-\mathrm{K}_s) \simeq 0.05$ and are predicted to trace the stellar population within 10% for metallicities in the range [0.02,1.5] solar (Salaris & Girardi 2002). In the color-magnitude diagram, RCG appear spread because of distance, reddening, age ($\sim 0.03$/Gyr in $\mathrm{K}_s$ at age 10Gyr), and metallicity (by $\sigma_{Ks}$(Fe/H) $\sim$0.11 for the measured bulge metallicity distribution). Among the 25,500 stars of the ARGOS survey, RCG are prominent down to [Fe/H]$= -1.0$, which comprises $\sim$95% of their sample (Ness et al. 2013a); i.e., RCG are representative for most of the bulge stars.

Using $\sim$8 million RCG from the VVV survey (Minniti et al. 2010) over the region $-10^\circ \le l \le 10^\circ$, $-10^\circ \le b \le 5^\circ$, Wegg & Gerhard (2013) obtained RCG line-of-sight density distributions for $\sim$ 300 sightlines outside the most crowded region $|b| < 1^\circ$, and combined these to a 3-dimensional map of the bulge RCG density assuming 8-fold triaxial symmetry (Figure 7). As shown in the figure, RMS variations between 8-fold symmetric points in the final map are indeed small; there is no evidence for asymmetries in the volume of the RCG measurement ($\pm 2.2 \times \pm 1.4 \times \pm 1.2$ kpc). The RCG bulge is strongly barred, with face-on projected axis ratio $\simeq (1:2.1)$ for isophotes reaching $\sim$2 kpc along the major axis; it has a strong b/p-shape viewed side-on, and a boxy shape as seen from the Sun, consistent with the earlier COBE and 2MASS data. Unsharp masking (Portail et al. 2015) results in a strong off-centered X-shape structure (Fig. 7), similar to some galaxies in the sample of Bureau et al. (2006); see also Nataf et al. (2015).

**Box/Peanut (b/p) bulge:**

$\phi_{\rm bp}$: $27 \pm 2^\circ$, b/p bulge bar angle

$(b/a)_{\rm bp}$: $0.5 \pm 0.05$, axis ratio from top

$(c/a)_{\rm bp}$: 0.26, edge-on axis ratio ($x \sim 0$)

$h_{\rm bp}$: 180 pc, vertical scale-height ($x \sim 0$)

$x_X$: $1.5 \pm 0.2$ kpc, radius of max. X

The near side of the b/p bulge has its major axis in the first Galactic quadrant ($0^\circ < l < 90^\circ$). The *bar angle* between major axis and the Sun-Galactic center line found by Wegg & Gerhard (2013) is $\phi_{\rm bp} = 27^\circ \pm 2^\circ$, with most of the error systematic. This is consistent with earlier parametric determinations from OGLE $I$ band RCG star counts ($29^\circ \pm 2^\circ$, Cao et al. 2013), ($25^\circ \pm 2^\circ$, Rattenbury et al. 2007), ($20^\circ$-$30^\circ$, Stanek et al. 1997), from non-parametric inversion of 2MASS red giant star counts ($20^\circ$-$35^\circ$, López-Corredoira, Cabrera-Lavers & Gerhard 2005), and from modelling the asymmetry of the COBE NIR photometry ($\sim 25^\circ \pm 10^\circ$, Dwek et al. 1995; Binney, Gerhard & Spergel 1997; Freudenreich 1998; Bissantz & Gerhard 2002). The global bulge axis ratios obtained with parametric star count models are typically (1:0.4:0.3), similarly to those found from modelling the COBE data. However, it is clear from Fig. 7 that a single vertical axis ratio does not capture the shape of the b/p bulge. The lower left panel shows that the density distributions inside $\sim$ 1 kpc are nearly exponential, with scale-lengths $(h_x : h_y : h_z) = (0.70 : 0.44 : 0.18)$ kpc and axis ratios $(10 : 6.3 : 2.6)$ (Wegg & Gerhard 2013). Further down the major axis, $h_z/h_x$ increases to $\sim$0.5 at $x \sim 1.5$ kpc where the X-shape is maximal, and then decreases rapidly outwards.

**4.2.2. Inner bulge and disk structure.** The structure of the inner Galactic disk between the NSD and $R \sim 2$ kpc is not well-known due to heavy extinction and crowding. Observations of maser stars and VVV Cepheids indicate a barred disk of young stars (Habing et al. 2006; Dékány et al. 2015). The cold kinematics of young bar stars has likely been seen in APOGEE LOS velocity histograms (Aumer & Schönrich 2015). The short $h_z = 180$ pc vertical scale height in the bulge is perhaps indicative of a central disk-like, high-density pseudo-bulge

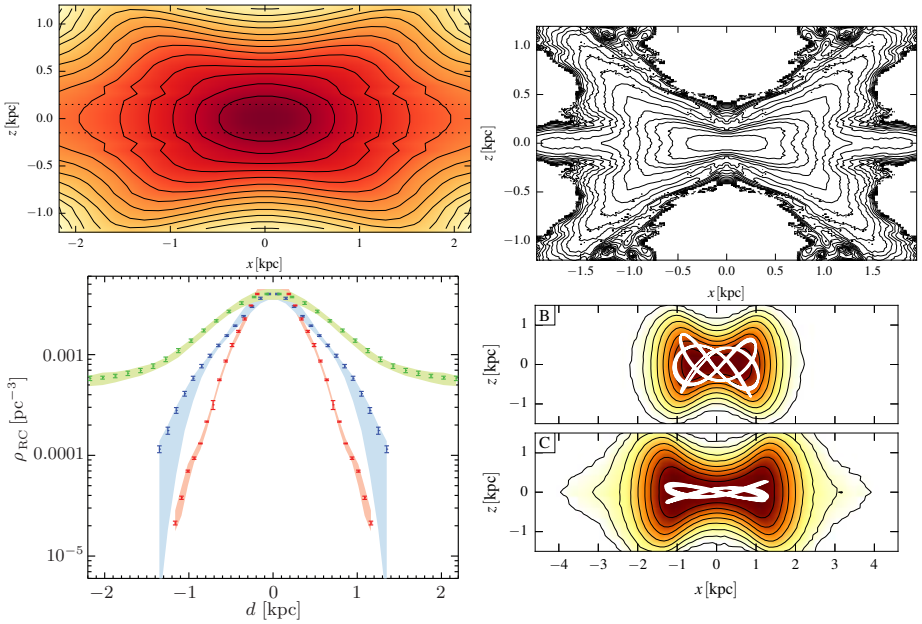


**Figure 7**

The Galactic b/p bulge density measured from K-band RCG star counts (Wegg & Gerhard 2013). Top left: side-on projection showing the prominent b/p shape. Top right: X-structure in unsharp-masked image (Portail et al. 2015). Bottom left: density profiles along the bulge principal axes $(x, y, z)$ in green, blue and red. The error bars show the RMS variations between 8-fold symmetric points around the triaxially symmetric 3D-map. Colored regions show estimated systematic errors. The density is typically accurate to $\sim$10%. Exponential scale-lengths along the $(x, y, z)$-axes are (0.70 : 0.44 : 0.18) kpc near the center. Bottom right: major orbit families supporting the b/p-shape in dynamical models of the b/p-bulge (Portail, Wegg & Gerhard 2015).

structure, as is seen in many early and late type b/p bulge galaxies (Bureau et al. 2006; Kormendy & Barentine 2010). NIR RCG star counts at $b = \pm 1^\circ$ have confirmed a structural change in the RCG longitude profiles at $|l| \simeq 4^\circ$ (Nishiyama et al. 2005; Gonzalez et al. 2011a; Wegg & Gerhard 2013). This has been interpreted by means of an N-body model in terms of a rounder, more nearly axisymmetric central parts of the b/p bulge (Gerhard & Martinez-Valpuesta 2012). As predicted by the model, the transition at $|l| \simeq 4^\circ$ is confined to a few degrees from the Galactic plane (Gonzalez et al. 2012).

The nuclear bulge within $\sim 200$ pc is dominated by the NSD. Based on longitudinal asymmetries in a map of projected 2MASS star counts Alard (2001) presented indications for a 200 pc scale nuclear bar separate from the b/p bulge-bar. However, the large-scale Galactic bar by itself leads to similar inverted asymmetries in the center, just by projection (Gerhard & Martinez-Valpuesta 2012), so the observed asymmetries are not a tell-tale signature. Unfortunately, the distance resolution of the RCG is not sufficient to investigate the LOS-structure of a tilted nuclear bar. Thus the most promising test appears to be with models of the nuclear gas flow (Bland-Hawthorn & Cohen 2003; Rodriguez-Fernandez & Combes 2008), but this requires understanding the larger-scale properties of the gas flow better (see §4.4) which influence the nuclear gas flow. Further studies in the IR, both photometric and spectroscopic, are clearly needed to shed more light on the inner bulge.

**4.2.3. Does the Milky Way have a classical bulge? Kinematics and metallicities of bulge stars.** Bulges in several disk galaxy formation models have been found to harbour a rapid early starburst component, as well as a second component which forms later after disk build-up and instabilities, and/or minor mergers (Samland & Gerhard 2003; Obreja et al. 2013). The former could be associated with a classical bulge even in the absence of a significant early merger-built bulge. The Milky Way bulge has a well-established vertical metallicity gradient (Zoccali et al. 2008; Johnson et al. 2011; Gonzalez et al. 2013) which has often been taken as the signature of a dissipatively formed classical bulge (see Pipino, Matteucci & D'Ercole 2008). However, because violent relaxation is inefficient during the bar and buckling instabilities, preexisting metallicity gradients, such that stars with lower binding energies have lower metallicities, would survive as outward metallicity gradients in the final b/p bulge (Martinez-Valpuesta & Gerhard 2013; Di Matteo et al. 2014). Recent spectroscopic surveys have attributed the vertical metallicity gradient to a superposition of several metallicity components whose relative contributions change with latitude (Babusiaux et al. 2010; Ness et al. 2013a). Hence the signature of a classical bulge must be found with more detailed kinematic and chemical observations.

The mean line-of-sight rotation velocities of bulge stars are nearly independent of latitude, showing *cylindrical rotation* as is common in barred bulges. First found with planetary nebulas (Beaulieu et al. 2000), this was shown conclusively with the BRAVA (Kunder et al. 2012), ARGOS (Ness et al. 2013b), and GIBS (Zoccali et al. 2014) surveys. Rotation velocities reached at $l \sim 10^\circ$ are $\sim 75$ km s$^{-1}$. LOS velocity dispersions at $l \sim 0$ are $\sim 80$ km s$^{-1}$ at $|b| = 8^\circ$ and increase rapidly towards the Galactic plane, reaching $\sim$120 km s$^{-1}$ in Baade's window at $|b|=4^\circ$. Based on the dynamical model of Portail et al. (2015, see §4.2.4), mass-weighted velocity dispersions inside the bulge half mass radius are $(\sigma_x^b, \sigma_y^b, \sigma_z^b) \approx (135, 105, 96)$ km s$^{-1}$ and the rms is $\sigma_{\rm rms}^b \approx 113$ km s$^{-1}$, to $\approx$3km s$^{-1}$.

The ARGOS survey mapped the kinematics for different metallicities, showing that higher/lower metallicity stars have lower/higher velocity dispersions. Soto, Rich & Kuijken (2007) and Babusiaux et al. (2010) found differences between the vertex deviations of metal-rich and metal-poor bulge stars and argue for the existence of two main bulge stellar populations, of which only the more metal-rich one follows the bar. Rojas-Arriagada et al. (2014) find two about equally numerous, metal-rich and metal-poor components in the metallicity distribution of their fields, whereas (Ness et al. 2013a,b) find evidence for five populations. The metal-rich components trace the X-shape and hence the barred bulge, but the origin of the metal-poor stars ([Fe/H]$<-0.5$) is currently debated. They could represent an old bulge formed through early mergers, or a thick disk component participating in the instability together with the inner stellar halo (e.g. Babusiaux et al. 2010; Di Matteo et al. 2014).

Large numbers of RR Lyrae stars found in the OGLE and VVV bulge surveys have shown that the most metal-poor ([Fe/H]$=-1.0\pm0.2$), old population does not participate in the b/p-bulge (Dékány et al. 2013; Pietrukowicz et al. 2015), consistent with the ARGOS result that only stars with [Fe/H] $\gtrsim -0.5$ participate in the split red clump (Ness et al. 2012). The rotation of the RR Lyrae stars has not yet been measured. The ARGOS stars with [Fe/H]$<-1$ rotate still fairly rapidly; whether they could be stars from the stellar halo or a low-mass classical bulge spun up by the b/p-bulge (Saha, Martinez-Valpuesta & Gerhard 2012) is still to be checked in detail.

In summary, it is unclear at this time whether the Milky Way contains any classical bulge at all - comparing N-body-simulated b/p bulge models to the BRAVA data, Shen et al.

(2010) found that the cylindrical rotation in the Galactic bulge could be matched by their models only if the initial models contained a classical bulge with $\lesssim 8\%$ of the initial disk mass ( $\lesssim 25\%$ of the final bulge mass), and none was needed. However, there is strong evidence from structural and kinematic properties that the major part of the Galactic bulge was built from the disk through evolutionary processes similar to those observed in galaxy evolution simulations, as is also inferred for many external galaxies (so-called *secular evolution*, Kormendy 2013).

**4.2.4. Mass and mass-to-light ratio in the bulge.** The stellar mass of the bulge can be estimated from a photometric model combined with a stellar population model. For example, Dwek et al. (1995) obtained $1.3 \times 10^{10}\ M_\odot$ from the COBE NIR luminosity and a Salpeter IMF ($2.0 \times 10^{10}\ M_\odot$ rescaled for Kroupa IMF, Licquia, Newman & Brinchmann 2015). Valenti et al. (2015) obtained a projected mass of $2.0 \pm 0.3 \times 10^{10}\ M_\odot$ from scaling the measured mass function in a small bulge field to the whole bulge using RCG. The stellar mass corresponds to the dynamical mass only if the contribution of dark matter in the bulge region is unimportant.

The dynamical mass in the bulge can be determined either from gas kinematics in the bulge region, or from stellar kinematics combined with a dynamical model. For a barred bulge, simple rotation curve analysis does not apply, and analysis of the full gas velocity field requires hydrodynamical models (see §4.4). Stellar-dynamical models require a well-determined tracer density, i.e., a NIR luminosity or tracer density distribution. Furthermore, since the dominant part of the Galactic bulge is the inner b/p part of the Galactic bar, the result depends somewhat on the spatial region defined as "the bulge".

Zhao, Spergel & Rich (1994) built a self-consistent model of the bar/bulge using the Schwarzschild method, and found a total bulge mass of $2 \times 10^{10}\ M_\odot$. Kent (1992) modelled the 2.4 $\mu$m SPACELAB emission with an oblate isotropic rotator and constant mass-to-light ratio, finding a mass of $1.8 \times 10^{10}\ M_\odot$. Bissantz, Englmaier & Gerhard (2003) determined the circular velocity at 2.2 kpc to be 190 km s$^{-1}$, modelling gas dynamics in the potential of the deprojected COBE NIR luminosity distribution from Bissantz & Gerhard (2002). Assuming spherical symmetry, this leads to a total bulge mass of about $1.85 \times 10^{10}\ M_\odot$. However, a number of other studies have found lower masses (Licquia, Newman & Brinchmann 2015).

In the most recent study, Portail et al. (2015) find a very well-constrained total dynamical mass of $1.84 \pm 0.07 \times 10^{10}\ M_\odot$ in the VVV bulge region (the box $\pm 2.2 \times \pm 1.4 \times \pm 1.2$ kpc), by fitting made-to-measure dynamical models to the combined VVV RCG star density and BRAVA kinematics (Figure 8). The data can be fit well by models with a range of dark-to-stellar mass ratios. Comparing the implied total surface mass density with the COBE surface brightness and stellar population models, a Salpeter IMF for a 10 Gyr old population can be ruled out, predicting significantly more mass than is dynamically allowed. For an IMF between those of Kroupa (2001); Chabrier (2003); Zoccali et al. (2000), 10-40% of the mass in the bulge region would required to be in dark matter. Recently Calamida et al. (2015) derived the bulge IMF in the SWEEPS field, removing foreground disk stars, and found a double-power law form remarkably similar to a Kroupa or Chabrier IMF. The models of Portail et al. (2015) then predict a total stellar mass in this region of 1.4-1.7 $\times 10^{10}\ M_\odot$, including stars in the inner disk, and a dark matter fraction of 10-25%. The estimated total stellar mass in the bulge and disk of the Galaxy is $M^*_{\rm tot} \approx 4.7\text{-}5.7 \times 10^{10}\ M_\odot$ (§6.4), so the ratio of stellar mass in the bulge region to total is $M^*_{\rm b}/M^*_{\rm tot} = 0.3 \pm 0.06$.

The stellar mass involved in the peanut shape is important for constraining the origin of

$M^{\rm dyn}_{\rm b}$: $1.84 \pm 0.07 \times 10^{10}\ M_\odot$, dynamical mass in VVV bulge region

$M^*_{\rm b}$: (1.4-1.7) $\times 10^{10}\ M_\odot$, stellar mass in VVV bulge region

$M^*_{\rm b}/M^*_{\rm tot}$: $0.3 \pm 0.06$, stellar mass in the bulge region to total

$f_{\rm b,DM}$: 10%-25%, dark matter fraction in VVV region

$(\sigma^b_x, \sigma^b_y, \sigma^b_z, \sigma^b_{\rm rms})$: (135, 105, 96, 113) km/s, mass-weighted velocity dispersions within half-mass radius along $(x, y, z)$ and rms

$M_{\rm clb}/M^*_{\rm b}$: 0-25%, classical bulge (clb) fraction

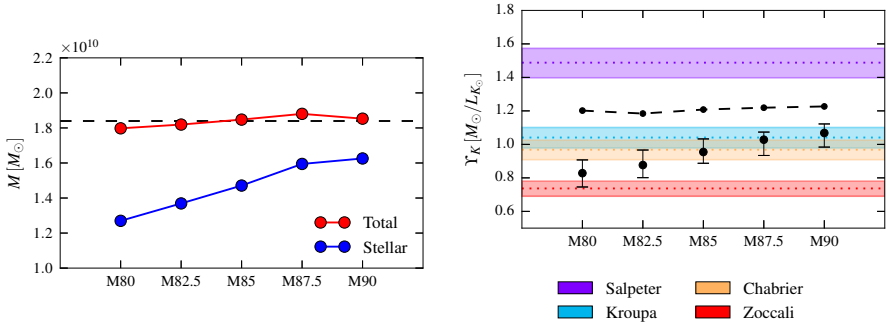


**Figure 8**

Left: Mass of the Galactic bulge in the VVV box for the five dynamical models of Portail et al. (2015) with different dark matter halos. The blue curve refers to the stellar mass while the red curve refers to the total mass. Right: Stellar mass-to-light ratio in the $K$ band for the same five models. The model errors shown are dominated by systematic effects. The different colored lines indicate predictions for different IMF as stated in the legend. The most recent measurements (Calamida et al. 2015) are close to a Kroupa IMF. The black dashed line is an estimate of the highest allowed mass-to-light ratio obtained by turning all dark matter in the VVV box into stars. This rules out a Salpeter IMF for the Galactic bulge with age 10 Gyr.

the bulge populations (§4.2.3). Li & Shen (2012) applied an unsharp masking technique to the side-on projection of the model of Shen et al. (2010), removing an elliptical bulge model from the total. This revealed a centred X-structure accounting for about 7% of their model bulge. Portail et al. (2015) removed a best-matched ellipsoidal density from the three-dimensional RCG bulge density of Wegg & Gerhard (2013), finding that 24% of the bulge stellar mass remained in the residual X-shape. Most reliable would be a dynamical, orbit-based definition of the mass in the peanut shape. However, in the bulge models of Portail et al. (2015), stars in the X-shape do not stream along $x_1v_1$ 'banana' orbits (Pfenniger & Friedli 1991) which follow the arms of the X-shape. Instead, the peanut shape is supported by 'brezel' orbit families which contribute density everywhere between the arms of the X-structure (Portail, Wegg & Gerhard 2015, see Fig. 7). In these models, the fraction of stellar orbits that *contribute* to the X-structure account for 40-45% of the bulge stellar mass.

## 4.3. The "long bar" outside the bulge

In N-body models for disk galaxy evolution, box/peanut bulges are the inner three-dimensional parts of a longer, planar bar which buckled out of the galaxy plane in a firehose-like instability (Combes et al. 1990; Raha et al. 1991; Athanassoula 2005). There is also evidence that b/p bulges in external galaxies are embedded in longer, thinner bars (Bureau et al. 2006). Thus also the Milky Way is expected to have a thin bar component extending well outside the b/p bulge. Finding the Galactic planar bar and characterizing its properties has however proven difficult, because of intervening dust extinction and the superposition with the star-forming disk at low-latitudes towards the inner Galaxy.

Hammersley et al. (2000) drew attention to an overdensity of stars in the Milky Way disk plane reaching outwards from the bulge region to $l \simeq 28°$. NIR star count studies with UKIDSS and other surveys confirmed this structure (Cabrera-Lavers et al. 2007, 2008). Its vertical scale-length was found to be less than 100 pc, so this is clearly a disk feature. With SPITZER GLIMPSE mid-infrared star counts, less affected by dust than K-band data,

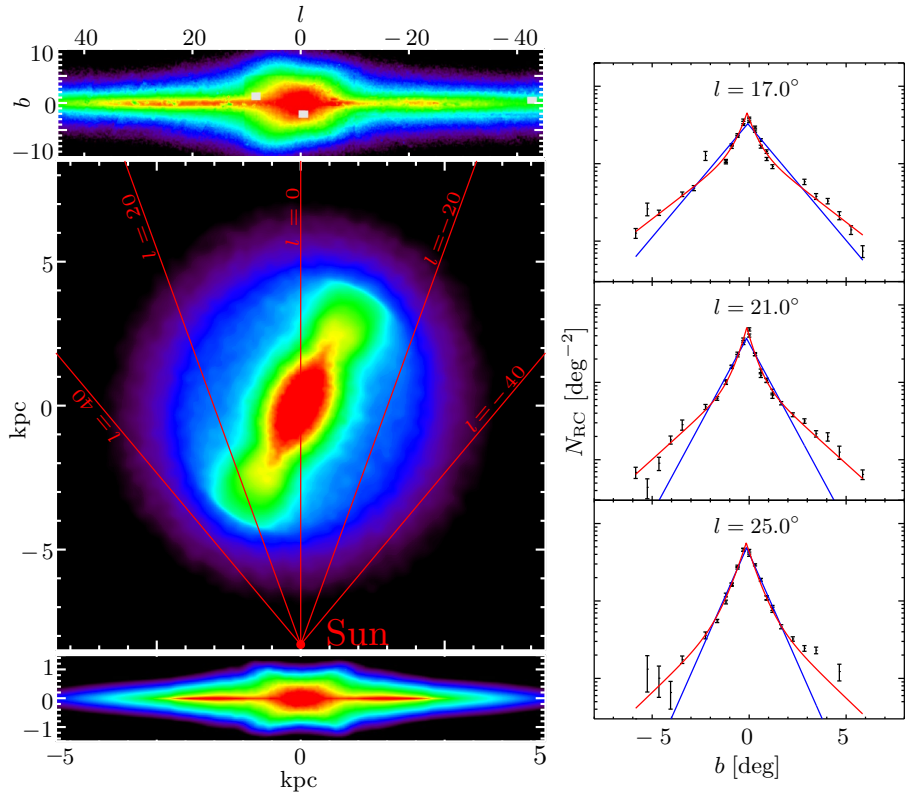


**Figure 9**

Left: projections of the Galactic b/p-bulge and long bar reconstructed from NIR star counts. Top: inner Galaxy as seen from the Sun, in bright star counts complete across several NIR surveys. Middle: Projection of best-fitting RCG star count model as seen from the North Galactic Pole. Viewing directions from the Sun are indicated for longitudes $|l| = 0°, 20°, 40°$. Bottom left: side-on view showing the transition from the b/p bulge to the long bar and disk. Right: Vertical surface density profiles of RCG stars for several longitude slices in the long bar region. Blue lines show single exponential fits. Red lines show the preferred double exponential model consisting of a superthin ($h_z = 45\,\mathrm{pc}$) and a thin bar component ($h_z = 180\,\mathrm{pc}$). The fraction of stars in the superthin component increases with longitude (adapted from Wegg, Gerhard & Portail 2015).

Benjamin et al. (2005) similarly found a strong bar-like overdensity of sources at positive longitudes. Because of its wide longitude extent and the narrow extent along the LOS this structure was termed the "long bar".

Based on the combined 2MASS, UKIDSS, VVV, and GLIMPSE surveys, Wegg, Gerhard & Portail (2015) investigated the long bar in a wide area in latitude and longitude, $|b| \leq 9°$ and $|l| \leq 40°$, using RCG stars and correcting for extinction star-by-star. They found that the Galactic bar extends to $l \sim 25°$ at $|b| \sim 5°$ from the Galactic plane, and to $l \sim 30°$ at lower latitudes. Their long bar has an angle to the line-of-sight of $29.5° \pm 1.5°$, consistent with the bar angle inferred for the bulge at $|l| < 10°$. The vertical scale-height of the RCG stars decreases continuously from the b/p bulge to the long bar. Thus the central b/p bulge appears to be the vertical extension of a longer, flatter bar, similar as seen in external

**Long bar:**

$\phi_{\rm lb}$: $29.5° \pm 1.5°$, long bar angle

$R_{\rm lb}$: $5.0 \pm 0.2$ kpc, bar half-length

$h_{\rm tlb}$: 180 pc, thin bar scale-height

$h_{\rm slb}$: 45 pc, superthin bar scale-height

$M_{\rm tlb}$: $\sim 7 \pm 0.1 \times 10^9\ M_\odot$, stellar mass of thin bar

$M_{\rm slb}$: $\sim 3 \times 10^9\ M_\odot$, stellar mass of superthin bar

galaxies and N-body models.

These recent results are based on a larger and more uniform data base and on a more uniform analysis than the earlier work on the long bar, using cross-checked star-by-star extinction corrections and a statistical rather than CMD-based selection of RCG stars. This leads to smaller errors in the RCG magnitude distributions and reduced scatter between neighbouring fields, particularly near the Galactic plane. These results therefore supercede in particular the earlier claim that the long bar is an independent bar structure at angle $\sim 45°$ and misaligned with the b/p bulge.

Comparing parametric models for the RCG magnitude distributions with the data, Wegg, Gerhard & Portail (2015) find a total bar (half) length of $R_{\rm lb} = 5.0 \pm 0.2$ kpc. Projections of their best model for the combined bulge and long bar are shown in Figure 9. The top panel illustrates the asymmetries seen by observers at the Sun, due to the bar shape and geometry. The side-on view in Fig. 9 clearly shows the Milky Way's central box/peanut bulge and the decrease of the scale-height in the long-bar region. In the central face-on view, the projected b/p-bulge resembles the bar-lens structures described by Laurikainen et al. (2011), which are considered to be the more face-on counterparts of b/p-bulges (Laurikainen et al. 2014); see the image of NGC 4314 in Figure 10.

In the same analysis, Wegg, Gerhard & Portail (2015) find evidence for two vertical scale-heights in the long bar, also illustrated in Fig. 9. The *thin* bar component has $h_{\rm tlb} \simeq 180$ pc and its density decreases outwards roughly exponentially; it is reminiscent of the old thin disk near the Sun. The second *superthin* bar component has $h_{\rm slb} \simeq 45$ pc and its density increases outwards towards the bar end where it dominates the RCG counts. The short scale-height is similar to the 60-80 pc superthin disk found in the edge-on spiral galaxy NGC 891 (Schechtman-Rook & Bershady 2013). Stars in this component have an estimated vertical velocity dispersion of $\sigma_z \simeq$ 20-30 km s$^{-1}$ and should be younger than the thin component. However, to have formed RCG they must have ages at least $> 0.5$ Gyr but star-forming galaxies have a strong bias towards ages around $\sim 1$ Gyr (Salaris & Girardi 2002). Such a younger bar component could arise from star formation towards the bar end or from disk stars captured by the bar.

The dynamical mass of the long bar component has not yet been determined. The stellar mass was estimated by Wegg, Gerhard & Portail (2015) from the RCG density using isochrones and a Kroupa IMF. This resulted in a total non-axisymmetric mass for the thin bar component of $M_{\rm tlb} \simeq 6-8 \times 10^9\ M_\odot$, assuming a 10 Gyr old, $\alpha$-enhanced population, and $M_{\rm slb} \simeq 3.3 \times 10^9\ M_\odot$ for the superthin component, assuming a constant past star formation rate. Owing to its 5 kpc half-length and its total mass $\sim 10^{10}\ M_\odot$, the long bar may have quite some impact on the dynamics of the Galactic disk inside the solar circle, particularly on the gas flow and the spiral arms, but perhaps also on surface density and scale-length measurements in the disk (see Fig. 10). In Section 4.4 below, we summarize constraints on the bar's corotation radius, which must be larger than $R_{\rm lb}$.

## 4.4. Pattern speed

The pattern speed $\Omega_{\rm b}$ of the b/p bulge and bar, or equivalently its corotation radius $R_{\rm CR}$, has great importance for the dynamics of the bar and surrounding disk. Despite a number of different attacks on measuring $\Omega_{\rm b}$ its value is currently not accurately known. An upper limit comes from determining the length of the bar and assuming that, like in external galaxies the Galactic bar is a fast bar, i.e., $\mathcal{R} = R_{\rm CR}/R_{\rm lb} = 1.2 \pm 0.2$ (Aguerri, Debattista

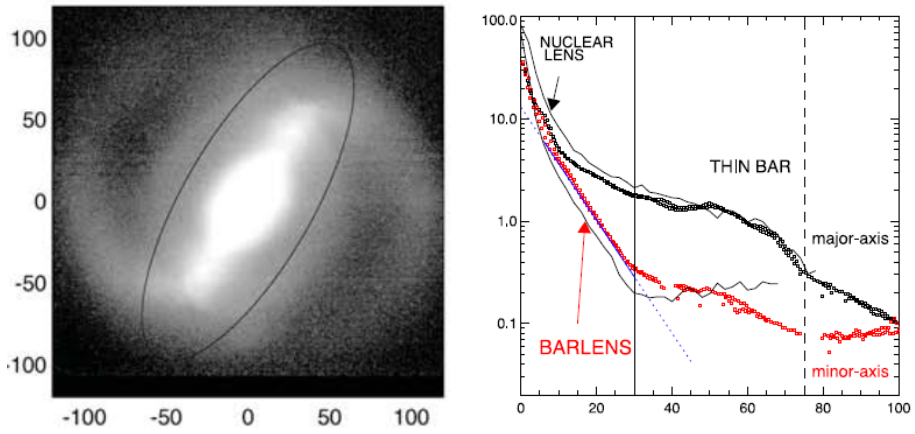


**Figure 10**

Left: K-band image of the bar-lens galaxy NGC 4314 from Laurikainen et al. (2011), with similar morphology as the face-on image of the Galactic b/p bulge and long bar in Fig. 9. Scaled and reflected to the rotation of the Milky Way, the Sun would be located at roughly (-110",-80") in this image. Right: major and minor axis surface brightness profiles for NGC 4314, from Laurikainen et al. (2014).

& Corsini 2003; Aguerri et al. 2015). Here the 1.0 lower limit is based on the fact that theoretically, bars cannot extend beyond their corotation radius because the main $x_1$-orbit family supporting the bar becomes unstable (Contopoulos 1980; Athanassoula 1992). The length of the long bar from starcounts is $R_{\rm lb} \simeq 5.0 \pm 0.2$ kpc and the length of the thin bar component alone is $R_{\rm tlb} \simeq 4.6 \pm 0.3$ kpc (Wegg, Gerhard & Portail 2015); thus a strong lower limit is $R_{\rm CR} = 4.3$ kpc and a more likely range is $R_{\rm CR} = 5.0 - 7.0$ kpc, or $\Omega_{\rm b} \sim 34 - 47\,{\rm km\,s^{-1}\,kpc^{-1}}$ for $\Theta_0 = 238$ km s$^{-1}$ = const. (§6.4).

Early determinations appeared to give rather high values of $\Omega_{\rm b}$. The most direct method applied a modified version of the Tremaine-Weinberg continuity argument to a complete sample of OH/IR stars in the inner Galaxy (Debattista, Gerhard & Sevenster 2002), giving $\Omega_{\rm b} = 59 \pm 5 \pm 10$ (sys) km s$^{-1}$ kpc$^{-1}$ for $(R_0, \Theta_0) = (8\,{\rm kpc}, 220$ km s$^{-1})$ but depending sensitively on the radial motion of the LSR.

More frequently, the pattern speed of the bar has been estimated from hydrodynamic simulations comparing the gas flow with observed Galactic CO and HI *lv*-diagrams. These simulations are sensitive to the gravitational potential, and generally reproduce a number of characteristic features in the *lv*-plot, but none reproduces all observed features equally well. Consequently the derived pattern speeds depend somewhat on the gas features emphasized. Englmaier & Gerhard (1999) and Bissantz, Englmaier & Gerhard (2003) estimated $55 - 65\,{\rm km\,s^{-1}\,kpc^{-1}}$ ($R_{\rm CR} = 3.4 \pm 0.3$ kpc) matching the terminal velocity curve, spiral arm tangents and ridges in the *lv*-plot. Fux (1999) obtained $\sim 50\,{\rm km\,s^{-1}\,kpc^{-1}}$ ($R_{\rm CR} = 4 - 4.5$ kpc) from a comparison to various reference features in the CO *lv*-plot; Weiner & Sellwood (1999) obtained $42\,{\rm km\,s^{-1}\,kpc^{-1}}$ ($R_{\rm CR} = 5.0$ kpc) from matching the extreme HI velocity contour; Rodriguez-Fernandez & Combes (2008) obtained $30 - 40\,{\rm km\,s^{-1}\,kpc^{-1}}$ and $R_{\rm CR} = 5 - 7$ kpc matching to the Galactic spiral arm pattern. The most recent analysis based on a range of potential parameters is by Sormani, Binney & Magorrian (2015). They conclude that overall a pattern speed of $\Omega_{\rm b} = 40\,{\rm km\,s^{-1}\,kpc^{-1}}$ corresponding to $R_{\rm CR} = 5.6$ kpc

matches best the combined constraints from the terminal velocity envelope, the central velocity peaks, and the spiral arm traces in the $lv$-diagram (for $R_0, \Theta_0 = 8\,\mathrm{kpc}, 220\ \mathrm{km\ s^{-1}}$).

Stellar-dynamical models of the Galactic b/p bulge also depend on $\Omega_\mathrm{b}$ and give estimated ranges for its value. Shen et al. (2010) and Long et al. (2012) find $\Omega_\mathrm{b} \simeq 40\,\mathrm{km\,s^{-1}\,kpc^{-1}}$ for the same N-body model matched to the BRAVA kinematic data. The recent models of Portail et al. (2015) fitted additionally to the RCG density from Wegg & Gerhard (2013) give values in the range $\Omega_\mathrm{b} \sim 25 - 30\,\mathrm{km\,s^{-1}\,kpc^{-1}}$, placing corotation in the range $R_\mathrm{CR} > 7.2\,\mathrm{kpc}$ (for $R_0, \Theta_0 = 8.3\,\mathrm{kpc}, 220\ \mathrm{km\ s^{-1}}$). These values could depend somewhat on the still uncertain gravitational potential in the long bar region.

A final method is based on the interpretation of star streams observed in the distribution of stellar velocities in the solar neighborhood as due to resonant orbit families near the outer Lindblad resonance of the bar (Kalnajs 1991; Dehnen 2000). Dehnen (2000) estimates $\Omega_\mathrm{b} = (1.85{\pm}0.15)\ \Theta_0/R_0$ ($51{\pm}4\,\mathrm{km\,s^{-1}\,kpc^{-1}}$ for $(R_0, \Theta_0) = (8\,\mathrm{kpc}, 220\ \mathrm{km\ s^{-1}})$. Minchev, Nordhaus & Quillen (2007) find $\Omega_\mathrm{b} = (1.87 \pm 0.04)\ \Theta_0/R_0$ ($51.5 \pm 1.5\,\mathrm{km\,s^{-1}\,kpc^{-1}}$). Chakrabarty (2007) and others argue that spiral arm perturbations need to be included, finding $R_0/R_\mathrm{CR} \simeq 2.1 \pm 0.1$ and $\Omega_\mathrm{b} \simeq 57.5 \pm 5\,\mathrm{km\,s^{-1}\,kpc^{-1}}$. The latest analysis of the Hercules stream by Antoja et al. (2014) gives $R_0/R_\mathrm{CR} \simeq (1.83 \pm 0.02)$, $\Omega_\mathrm{b} \simeq 53 \pm 0.5\,\mathrm{km\,s^{-1}\,kpc^{-1}}$, and $R_\mathrm{CR} = 4.49 \pm 0.05\,\mathrm{kpc}$ when rescaled to $(R_0, \Theta_0) = (8.2\,\mathrm{kpc}, 238\ \mathrm{km\ s^{-1}})$. This is the current most precise measurement but is model-dependent; it would place corotation just inside the thin long bar and clearly within the superthin bar. It is just compatible with all the uncertainties; alternatively it may suggest that the Hercules stream has a different origin than the outer Lindblad resonance.

$\Omega_\mathrm{b}$: $43 \pm 9\,\mathrm{km\,s^{-1}\,kpc^{-1}}$ Bar pattern speed

$R_\mathrm{CR}$: 4.5-7.0 kpc Bar corotation radius

Considering all these determinations and the systematic uncertainties, we finally adopt a range of $R_\mathrm{CR} = 4.5$-$7\,\mathrm{kpc}$, or $\Omega_\mathrm{b} \simeq 43 \pm 9\,\mathrm{km\,s^{-1}\,kpc^{-1}}$ for our best estimated $(R_0, \Theta_0) = (8.2\,\mathrm{kpc}, 238\ \mathrm{km\ s^{-1}})$. More accurate dynamical modelling of a wider set of stellar-kinematical data, in particular from GAIA, is expected to narrow down this rather wide range in the coming years (Hunt & Kawata 2014).

## 5. STELLAR DISK

Our vantage point from within the Galaxy allows us to obtain vast amounts of unique information about galactic processes but this detail comes at a price. The Solar System falls between two spiral arms (Fig. 11) at a small vertical distance from the Galactic Plane (§3.3). The thinness of the disk gives a fairly unobstructed view of the stellar halo and the outer bulge. But deprojecting the extended disk remains fraught with difficulty because of source confusion and interstellar extinction. Our off-centred position at the Solar Radius is a distinct advantage except that it complicates any attempt to learn about large-scale, non-axisymmetries across the Galaxy. We now have a better understanding of the structure of the inner Galaxy (§4) but the outer disk remains largely mysterious (see §5.5 below).

Over the past decade, we have learnt much about the Galactic stellar disk, but few parameters are known with any precision. The local surface density and the vertical density profile of the summed disk component (gas, stars, background dark matter) are known to high certainty (§ 5.4.1). But while photometric scalelengths are well established in external galaxies (Lange et al. 2015), the radial scalelengths and vertical scaleheights of the Galactic thin and thick disks are uncertain. Unlike for the inner Galactic bar/bulge region (§4), we are not able to present a fully consistent picture for the disk at this time, although the key parameters are discussed and values recommended. Major reviews of the stellar disk include

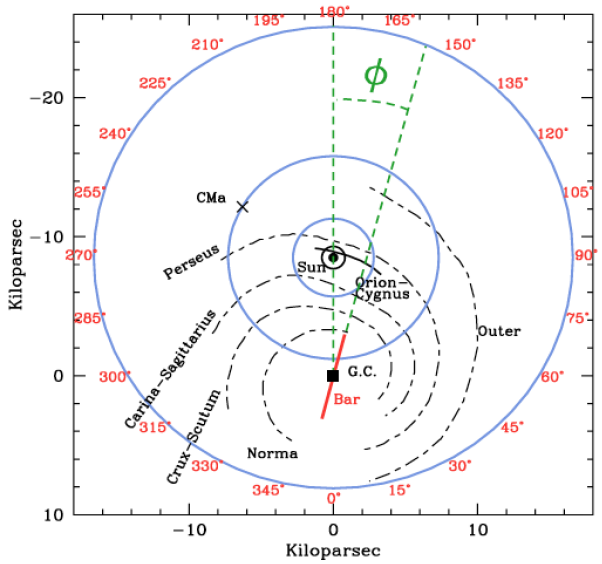


**Figure 11**

Plan elevation of the Galactic disk centred on the Sun's position showing the orientation and location of the main spiral arms. The numbered outer circle defines galactic longitude ($\ell$). The Canis Major (CMa) overdensity is in the same general direction as the maximum disk warp (Courtesy of Momany et al. 2006).

Freeman & Bland-Hawthorn (2002); Ivezić, Beers & Jurić (2012); Rix & Bovy (2013); the gaseous disk is discussed at length by Kalberla & Dedes (2008).

One of the most interesting developments is the recognition of a Galactic 'thick' disk that is distinct from the dominant thin disk through its unique chemistry (e.g. Bensby 2014; Masseron & Gilmore 2015; Hawkins et al. 2015), in addition to its older age and higher elevation. Originally recognized by Gilmore & Reid (1983), such disks appear to be ubiquitous in the local universe (Yoachim & Dalcanton 2006). In external galaxies, deep stellar photometry reveals that the thick and thin disks have approximately equal scale-lengths (e.g. Comerón et al. 2012). Whether these old red disks have a distinct formation history or have continuous properties with the old thin disk is unclear. Several authors have presented models where the Galactic thick disk arises from a combination of stellar migration and/or flaring of the old disk stars, such that its history is tied to the formation of the thin disk even though its mean metallicity may be different (e.g. Schönrich & Binney 2009; Loebman et al. 2011; Minchev et al. 2015). In view of the distinct chemical signature of the thick disk, it is worthwhile to quantify its properties separately from the thin disk regardless of its origins.

## 5.1. Stellar photometry

Early studies of the Galaxy fitted simple models to the projected star counts in a given optical or infrared band (e.g. Bahcall & Soneira 1980). Without distance information, these authors found that a variety of models fit the data (including many combinations of two exponential functions) due to degeneracies between structural parameters. Historically, fits

to star counts with vertical distance $z$ have used a variety of functions but, today, the exponential function is widely used to match both disk photometry (Patterson 1940) and the peaked star counts close to the plane (Wainscoat, Freeman & Hyland 1989).

By the end of the decade, we can expect accurate distances for millions of stars from the ESA GAIA survey. But for now, we are dependent on photometric parallaxes for determining stellar distances which have a long history in their application to Milky Way structure (Gilmore & Reid 1983; Kuijken & Gilmore 1989; Chen et al. 2001). The term 'parallax' echoes the use of nearby bright stars with established trigonometric parallaxes to calibrate the absolute magnitude-distance relation (e.g. Eggen 1951). (The term 'spectroscopic parallax' refers to the spectral classification used to determine the absolute magnitude, rather than photometric colours.)

**5.1.1. Scaleheights.** All photometric studies find an exponential scaleheight $z^{\rm t} = 220 - 450$ pc for the dominant old thin disk at the Sun's location. The low extreme comes from multiband optical studies (e.g. Ojha 2001) which include stellar populations with a wide range of (especially younger) ages. These surveys suffer from various biases that tend to suppress the scaleheight (see below). The upper extreme is from early M dwarf studies where confusion with halo M giants can lead to overestimates of the scaleheight (Reid 1993; Gould, Bahcall & Flynn 1996). M dwarfs, which account for roughly half of all stars in the solar neighbourhood (§ 5.4.2), trace the underlying total stellar mass. The much larger M star survey by Jurić et al. (2008), discussed below, finds $z^{\rm t} \approx 300$ pc (to within 20%) after various biasses are accounted for. This mid-range value is largely unchanged since Schmidt's early determination (Schmidt 1963).

An improvement is to use two or more well calibrated optical bands to compare the magnitude counts in different colour bins. This led to Gilmore & Reid's identification of the thick disk after constructing the $V$ and $I$ luminosity functions for stars at or above the main sequence turn-off (MSTO) at different distances from the plane, and by ruling out biases due to interstellar extinction or metallicity gradients perpendicular to the disk. This classic study observed 12500 stars towards the South Galactic Pole (SGP) brighter than $I = 18$ and provided the first reliable stellar densities vertical to the Galactic Plane – their density profile continues to compare well with modern derivations (§ 5.4.1). They estimated $z^{\rm t} \approx 300$ pc in line with modern estimates, and $z^{\rm T} \sim 1450$ pc, somewhat higher than what is believed today.

After 2000, the quality and angular extent of photometric data from wide-field CCDs improved dramatically (e.g. Finlator et al. 2000). The internal accuracies of the multiband data led to improved estimates of photometric parallax and metallicity (robust in the range -2 < [Fe/H] < 0) in wide-field surveys (see Ivezić, Beers & Jurić 2012). Notably, Siegel et al. (2002) observed select Kapteyn fields to derive photometric distances for 130,000 stars. They stressed the need to correct for unresolved multiplicities (of order 50%), otherwise stellar distances (and therefore scaleheights) are underestimated. The lower scaleheight estimates in the past are likely to have been underestimated for this reason. Even for old stars, there is some scaleheight variation among dwarfs: 280−300 pc for early-type dwarfs ($5.8 < M_R < 6.8$) rising to 350 pc for late-type dwarfs ($8.8 < M_R < 10.2$). When averaging over old dwarfs, before and after the correction, they obtain $z^{\rm t} \approx 290$ pc and $z^{\rm t} \approx 350$ pc respectively; for the thick disk, they find $z^{\rm T} = 700 - 1000$ pc and $z^{\rm T} = 900 - 1200$ pc respectively. (These are derived from exponential models; sech$^2$ fits lead to 10% smaller values after correction for the factor of two difference in scaleheight between the exponential

and sech$^2$ functions.)

For our subsequent disk analysis, we focus on the SDSS *ugriz* northern sky survey with its excellent photometric quality (∼0.02 mag). With photometric data for 48 millions stars over 6500 deg$^2$, this is the largest to date with precise colour−magnitude vs. metallicity relations made possible using cluster calibrations across the sky (Finlator et al. 2000; Chen et al. 2001). This survey gave rise to three major studies based on photometric parallax (Jurić et al. 2008), photometric metallicities (Ivezić et al. 2008) and kinematics (Bond et al. 2010) discussed in the next two sections.

Juric et al (2008) exploit the faint magnitude limit ($r \sim 22$ mag) of the SDSS survey and target two groups of M dwarfs: a late M group with $1.0 < r - i < 1.4$ and an early M/late K group with $0.65 < r - i < 1.0$. The late M group is favoured because it is less sensitive to the halo population and to local substructure. At the Solar circle, their formal model fits for both disk components are $z^{\rm t} \approx 245$ pc and $z^{\rm T} \approx 740$ pc before correction for multiplicity, and closer to $z^{\rm t} \approx 300$ pc and $z^{\rm T} \approx 900$ pc after correction, both with 20% uncertainty. These constitute the most reliable values to date because of the SDSS coverage in Galactic longitude and improved photometric distances over the required physical scales. While the SDSS and 2MASS surveys are widely used in star count analyses, neither survey is ideal for determining the properties of the thick and thin disks *simultaneously*. Rather than cross-matching sources common to both catalogues (e.g. Finlator et al. 2000), future studies will need to combine both surveys in order to provide better input catalogues (Robin et al. 2014).

While the thick disk was originally identified through stellar photometry, decompositions based on star counts are subject to degeneracies (§ 5.1.3). We include a limited discussion of the photometric estimates because of the historical context and because the thin disk values are broadly correct. But we stress that the thick and thin disk components are better separated through their distinct stellar chemistry. Numerous studies (§ 5.2) exploit either stellar abundances based on multiband photometry (large samples, large measurement errors) or spectroscopy (smaller samples, smaller errors).

**5.1.2. Scalelengths.** While vertical scaleheights are well determined at optical and IR wavebands due to the low extinction towards the poles, this is not true of disk radial scalelengths. We have analysed 130 refereed papers on disk parameters, with scalelengths ranging from 1.8 to 6.0 kpc. In order to combat the effects of extinction, for observations that preceded the SDSS survey, the infrared point source measurements are the most reliable because they tell a consistent story. This is particularly true for studies that target a broad extent in Galactic longitude and observe in the anti-centre direction to ensure they are less influenced by the presence of the central bar or by substructure. These include the SPACE SHUTTLE experiment (Kent, Dame & Fazio 1991), DENIS (Ruphy et al. 1996) in the anti-centre direction, COBE/FIRAS (Freudenreich 1998; Drimmel & Spergel 2001), 2MASS (López-Corredoira et al. 2002; Cabrera-Lavers, Garzón & Hammersley 2005; Reylé et al. 2009), and GLIMPSE (Benjamin et al. 2005). A statistical analysis of the main papers (15 in all) on this topic leads to $R^{\rm t} = 2.6 \pm 0.5$ kpc which includes the highest value (3.9 kpc) from the GLIMPSE mid-infrared survey. Our estimate drops to $R^{\rm t} = 2.5 \pm 0.4$ kpc if we exclude the GLIMPSE study.

We have already stressed the importance of M stars. Jurić et al. (2008) determine $R^{\rm t} \approx 2.6$ kpc (20% uncertainty) for the thin disk. Gould, Bahcall & Flynn (1996) and Zheng et al. (2001) used the HUBBLE SPACE TELESCOPE to measure a scalelength of $R^{\rm t} =$

$3.0 \pm 0.4$ kpc and $R^{\rm t} = 2.8 \pm 0.3$ kpc respectively. *All of these values are consistent with the IR measurements.* A short scalelength finds strong support from dynamical studies of the stellar kinematics in §5.4. From a study of mono-abundance populations (MAP), Bovy et al. (2012b) conclude that different populations give a scalelength that is smoothly changing from 2 kpc in the inner disk (older populations) to 3 kpc at $R = 12$ kpc (younger populations), or maybe even longer. However, the disk is dominated by old populations: a characteristic scale is meaningful when one considers the mass density profile of the disk. *The IR photometric estimate of radial scalelength is probably the most useful at the present time, although we recognize that an exponential decline in the mass distribution is a crude approximation* (Fig. 10). The thick disk scalelength is discussed in the next section.

For the past thirty years, some have argued for a longer disk scalelength when comparing the Galaxy, with its high mass and luminosity, to external galaxies (q.v. van der Kruit & Freeman 2011). The GAMA survey (Driver et al. 2011) includes the largest bulge/disk decomposition survey to date using the VIKING K-band imaging survey of 4300 disk galaxies (Lange et al. 2015). This volume-limited survey has a high level of completeness to a redshift limit of $z < 0.06$ ($M_\star > 10^9 {\rm M}_\odot$). Here only only a few percent of galaxy disks exceed the Milky Way's disk mass, and their IR *photometric* scalelengths have a large spread ($4 \pm 2$ kpc). The Galaxy's high luminosity and small scalelength may not be so unusual.

*Disk substructure.* We highlight one spectacular result from the SDSS survey. The team was able to extract tomographic slices through the Galaxy vertical to the plane (e.g. Fig. 12). Fig. 12 illustrates a problem with Galaxy model fits and goes some way to explaining the lack of convergence in disk parameters over three decades. Jurić et al. (2008) explicitly highlight important substructure across the Galaxy including the 'Virgo overdensity' and the 'Monoceros ring' (Newberg et al. 2002). Substructure is so prevalent that it is not possible to fit a smooth double exponential disk model in $R$ and $z$ to either the thick or thin disk without taking this component into account. This problem is well known for disk-halo fitting because the Sgr stream dominates so much of the halo.

**5.1.3. Thick disk normalization.** Several studies have tried to determine the local density normalization ($f_\rho = \rho^T/\rho^t$) of the thick disk compared to the thin disk with estimates ranging from 1% to 12% (e.g. Gilmore & Reid 1983; Siegel et al. 2002; Jurić et al. 2008). The large uncertainty in $f_\rho$ is largely due to its degeneracy with the derived scalelengths for both components (Siegel et al. 2002; Arnadottir et al. 2009): higher estimates of $z^{\rm T}$ are associated with lower estimates of $f_\rho$, and vice versa. To aid comparison with most published results, we prefer this form for $f_\rho$ rather than normalization to the total disk mass (e.g. Piffl et al. 2014a). We have analysed all results from photometric surveys (25 in all) since the discovery paper and arrive at $f_\rho = 4\% \pm 2\%$.

A detailed analysis of the degeneracy between disk parameters is given by Chen et al. (2001) for late-type dwarfs chosen from the SDSS survey where the data are separated into two hemispheres. Our value of $f_\rho$ is in line with their likelihood analysis (see their Fig. 9) for a thick disk scale height of $z^{\rm T} = 900 \pm 100$ kpc. It is also broadly consistent with dynamical fitting to the Solar cylinder (e.g. $f_\rho \approx 6 \pm 2\%$; Just & Jahreiss 2010).

The error is smaller when we compare the surface density of the thick and thin disks, i.e. $f_\Sigma = f_\rho z^{\rm T}/z^{\rm t}$. Here we find $f_\Sigma = 12\% \pm 4\%$. Our analysis excludes all papers that do not fit simultaneously for the thin and thick disk. At this point, no separation is made on the basis of detailed stellar abundance information. A high thick disk local density ($f_\rho \approx 6\%$) is also found when spectroscopic abundances are used to define the high [$\alpha$/Fe] population

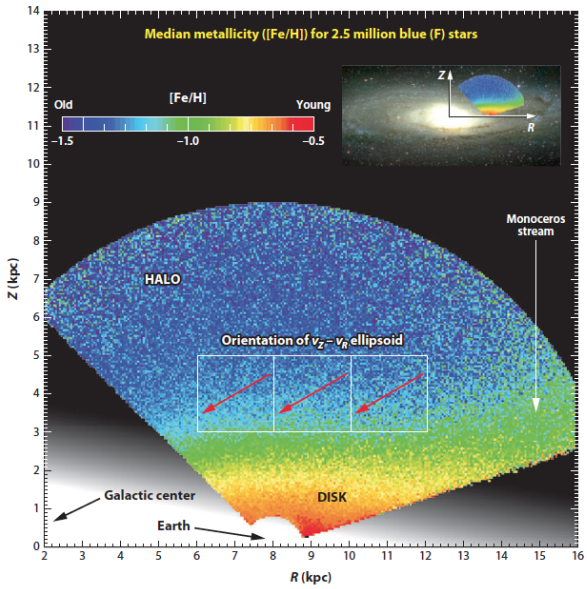


**Figure 12**

A tomographic slice showing the change in stellar metallicity through the Galaxy perpendicular to the Galactic plane and passing through the Galactic Centre and the Sun. The underlying stellar density is shown in half tone (Jurić et al. 2008). The dwarf star distances and metallicities are obtained from photometric parallax and photometric metallicities using the SDSS *ugriz* data calibrated using globular clusters over a range of metallicities (Ivezić et al. 2008). The photometric metallicities are robust within the range -2 < [Fe/H] < 0. This projection highlights the difficulty of fitting simple composite models to the stellar disk, particularly in the outer reaches where the Monoceros stream and other substructures become apparent. The direction of the halo vertex deviation taken from Bond et al. (2010) is also shown (Courtesy of Ivezić, Beers & Jurić 2012).

(Bovy et al. 2015) but this depends on how the abundance cut is made. A low value for $f_\rho$ is in conflict with Jurić et al. (2008) who determine the thick disk to be more massive ($f_\rho \approx 12\%$) at the Solar circle (cf. Fuhrmann 2008). Recent claims of a more massive thick disk may arise from the survey selection extending into the low [$\alpha$/Fe] population (e.g. Snaith et al. 2014) or from the use of a tiny survey volume (e.g. Fuhrmann 2008).

## 5.2. Stellar chemistry

**5.2.1. Photometric metallicity.** Ivezić et al. (2008) examined the vertical distribution in photometric metallicity of 2 million SDSS stars calibrated with SEGUE spectra of 60,000 F, G dwarfs ($0.2 < g - r < 0.6$). An additional refinement was to combine the Palomar Optical Sky Survey (POSS) and the SDSS data to derive proper motions (e.g. Munn et al. 2004). Here the tangential velocity accuracy for stars brighter than $g \sim 19$ is comparable to the radial velocity accuracy of the SDSS spectroscopic survey (15 km s$^{-1}$ for a star at 1 kpc; 100 km s$^{-1}$ at 7 kpc). The aim was to look for the thin disk-thick disk transition at ∼1 kpc, and the thick disk-halo transition at ∼2.5 kpc, in metallicity and velocity. The SDSS team confirm earlier trends in declining metallicity and increasing lag at larger elevations

$z^{\rm t}$: 300±50 pc, thin disk vertical scalelength at $R_0$

$z^{\rm T}$: 900±180 pc, thick disk vertical scalelength at $R_0$

$f_\rho$: 4%±2%, thick / thin disk local density ratio at $R_0$

$f_\Sigma$: 12%±4%, thick / thin disk surface density ratio at $R_0$

$R^{\rm t}$: 2.6±0.5 kpc, thin disk radial scalelength

$M^{\rm t}$: $3.5\pm1 \times 10^{10}\ M_\odot$, thin disk stellar mass

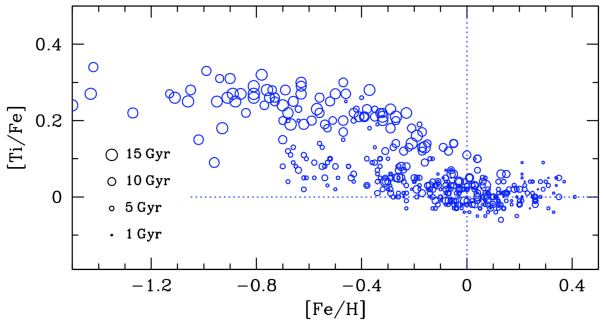


**Figure 13**

[Ti/Fe] vs. [Fe/H] for 700 F, G dwarf stars with age determinations showing a uniformly old population (thick disk) with enhanced [$\alpha$/Fe] abundance, and a dominant (thin) disk population with a spread of ages. The size of the circle scales with age and have uncertainties of order ∼Gyr; the metallicity uncertainties are smaller than 0.1 dex. Note how the two-component disk appears to exist at the solar metallicity extreme (Courtesy of Bensby 2014).

(Fig. 12), and find evidence for thick disk stars extending to $z > 5$ kpc. They could only discern a gradual transition in photometric metallicity and kinematics across the thin disk-thick disk divide, in conflict with the traditional two-component fit (cf. Bond et al. 2010). While no kinematic modelling was conducted at this stage (see § 5.3), the SDSS team find the data are more consistent with a gradual continuum from a thin young disk to an extended older disk. A better understanding of the thick disk vs. thin disk separation had to wait for spectroscopic surveys (§ 5.2) providing both improved elemental abundances and 3D space velocities (Steinmetz et al. 2006; Allende Prieto et al. 2008).

**5.2.2. Spectroscopic metallicity.** In the past, some researchers have questioned the existence of a thick disk with discrete properties − chemistry, age, kinematics − beyond the obvious characteristic of physical extent (e.g. Norris & Ryan 1991). This is a fundamental question because it hinges on the formation and evolution of the major baryonic component of our Galaxy. In Fig. 13, the stars of the thick disk are mostly older than the thin disk and have a distinct chemistry (Bensby, Feltzing & Lundström 2003; Schuster et al. 2006; Haywood 2006; Bensby 2014). It is recognized today that [$\alpha$/Fe] is enhanced for the thick disk compared to the thin disk over a wide range in [Fe/H], an effect that is easily seen in sufficiently high-resolution ($\mathcal{R} \gtrsim 20,000$) spectroscopic data (Fuhrmann 1998; Prochaska et al. 2000; Gratton et al. 2000; Reddy et al. 2003; Soubiran, Bienaymé & Siebert 2003; Reddy, Lambert & Allende Prieto 2006) even possibly at [Fe/H] $\gtrsim 0$ (Haywood et al. 2015; Hayden et al. 2015; Kordopatis et al. 2015). Recent studies show that the earlier counter claims likely suffered from underestimating measurement errors (e.g. Nidever et al. 2014) or incorrectly assumed that errors between measurements are uncorrelated (e.g. Schönrich, Asplund & Casagrande 2014).

The kinematic criteria often used to separate the disks inevitably lead to small stellar samples compared to photometric surveys. The Bensby studies exploit the Geneva-Copenhagen survey of 16000 nearby dwarfs with full 3D space velocities, and ages and metallicities from Strömgren photometry (Nordström et al. 2004). But a clean local separation is hampered in part by extensive kinematic substructure over the local volume: the

Hercules stream, for example, comprises both thick and thin disk stars (Bensby et al. 2007). But even without kinematic separation, the chemical signature of two distinct populations is evident (Adibekyan et al. 2012; Haywood et al. 2015).

A new signature has emerged from the APOGEE survey that may help to separate the disks further. Masseron & Gilmore (2015) show that C/N is enhanced in the thick disk compared to the thin disk, presumably due to the effects of dredge-up observed in old turn-off dwarfs and giants. The associated age (and mass) for the oldest stars is broadly consistent with Fig. 13. At the present time, it is not possible to separate the thick disk from the oldest thin disk stars through age-dating, assuming such a distinction even exists. The detailed chemistry of the thick disk may provide a better discriminator than the use of phase space (**x,v**) and be the defining characteristic of this component. Kinematic criteria will always lead to some overlap. Hawkins et al. (2015) emphasize that a more expanded chemical ($\mathcal{C}$) space may be called for to ensure that the thick disk can be separated from both the thin disk and the lower halo, i.e. $\mathcal{C}$([$\alpha$/Fe], [C+N/Fe], [Al/Fe], [Mg/Mn]). A high quality 'chemical tag' defined in this way requires both optical and infrared data at high spectroscopic resolution.

The use of chemistry to define thick disk stars now gives a different perspective on defining the relative density and scales of the two disks. Bensby et al. (2010) found that the bimodal [$\alpha$/Fe] distribution continues inside of the Solar Circle, in contrast to the outer disk where the enhanced [$\alpha$/Fe] population is not detected, which led Bensby et al. (2011) to infer a shorter scalelength for the thick disk. By dividing SEGUE dwarfs spectroscopically into MAPs, Bovy et al. (2012b) note the transition between a short scalelength, "high [$\alpha$/Fe], low [Fe/H] population," with a scaleheight up to 1000 pc, and a longer scalelength, "low [$\alpha$/Fe], high [Fe/H]" population, with a scaleheight below 400 pc. But the more extensive APOGEE survey of 70,000 red giants reveals that the picture is more complicated (Bovy et al. 2015; Hayden et al. 2015). Looking outwards, both tracks are evident, except the high [$\alpha$/Fe] sequence disappears beyond 11 kpc while the low sequence is seen to at least 15 kpc.

Towards the inner disk, the high [$\alpha$/Fe] track dominates over the low [$\alpha$/Fe] sequence even though an increasing fraction of stars pile up towards higher metallicity due to the thin disk abundance gradient. Over the innermost disk, the thick disk and bulge are more difficult to disentangle because they share kinematic and abundance characteristics, as observed in red giants (Alves-Brito et al. 2010; Ryde et al. 2010; Hill et al. 2011; Gonzalez et al. 2011b) and microlensed dwarf stars (Bensby et al. 2009, 2013).

In summary, estimates for the thick disk scalelength range from 1.8 to 4.9 kpc (12 papers) (e.g. Cheng et al. 2012; Larsen & Humphreys 2003) but few of these make a distinction based on chemistry. There exists now some convergence on $R^{\rm T}$ from surveys over very different volumes and sample sizes. Bensby et al. (2011) estimate an exponential scalelength of 2 kpc (≈10% accuracy), in good agreement with the high-[$\alpha$/Fe] MAPs from SEGUE (Bovy et al. 2012b), although Cheng et al. (2012) measure $R^{\rm T} \approx 1.8$ kpc using 7000 MSTO dwarfs from the same survey, albeit with larger errors. More recently, Bovy et al. (2015) find $R^{\rm T} = 2.2 \pm 0.2$ kpc for high-[$\alpha$/Fe] MAPs using APOGEE red clump giants. Overall, we conclude that $R^{\rm T} = 2.0 \pm 0.2$ kpc where the thick disk is defined in terms of the high-[$\alpha$/Fe] population. When extrapolated to the Galactic Centre, the ratios $f_\rho$ and $f_\Sigma$ are 2.6 times higher than the local values. Thus, taking into account the shorter scale length of the thick disk, we estimate $M^{\rm T} = 6 \pm 3 \times 10^9\ M_\odot$, or roughly one fifth of the thin disk mass.

$R^{\rm T}$: $2.0 \pm 0.2$ kpc, thick disk radial scalelength

$M^{\rm T}$: $6 \pm 3 \times 10^9\ M_\odot$, thick disk stellar mass

## 5.3. Stellar kinematics

The large photometric surveys, with their photometric distance estimates, provide us with initial estimates of the structural parameters for each of the major Galactic components. Over a decade ago, the community recognized that progress would require kinematic information for many stars over large swaths of the sky. Since that time, there has been extensive investment in wide-field stellar kinematic surveys, some of which are still in progress: GCS (Nordström et al. 2004); SEGUE (Yanny et al. 2009); RAVE (Steinmetz et al. 2006); APOGEE (Allende Prieto et al. 2008); LEGUE (Deng et al. 2012); GES (Gilmore et al. 2012); and GALAH (De Silva et al. 2015). These surveys look at different parts of the sky and go to different depths. Some have been rendered dynamically as 3D visualizations at the following website: https://www.rave-survey.org/project/gallery/movies. The GCS survey covers the full sky but is confined to the Solar Neighbourhood; the SEGUE, RAVE and APOGEE surveys penetrate deeper into the Galaxy than earlier stellar surveys. By far the largest of the new surveys, the ESA GAIA mission will obtain both spectra and astrometric information for up to ∼150 million stars (de Bruijne et al. 2015). By the end of the decade, we can expect to have radial velocities and stellar parameters for millions of stars, for dwarfs out to ∼1 kpc, and for giants out to the halo.

Here we review the main insights to emerge from these surveys. We make a distinction between dynamical models of the Galaxy (e.g. Rix & Bovy 2013, §6) and models that fit to the separate Galactic components without dynamical consistency (e.g. Catena & Ullio 2010), which we refer to as kinematic models. In a kinematic model, one specifies the stellar motions independently at each spatial location, and the gravitational field in which the stars move plays no role. In a dynamical model, the spatial density distribution of stars and their kinematics are self-consistently linked by the potential, under the assumption that the system is in steady state.

When fitting a model, there are important considerations. First, all surveys are defined by their selection function (e.g. magnitude, velocity, coordinates) and any biasses must be accomodated by the analysis. Secondly, it is important to make a stab at including a plausible star formation history into the analysis (e.g. Schönrich & Binney 2009). Making more stars in the past places more old stars at higher galactic latitudes today, and therefore higher kinematic dispersion through the age-velocity dispersion relation (e.g. Aumer & Binney 2009). But this adds to the complexity because (a) we are introducing new variables into an already crowded field; and (b) degeneracy exists between different parameters, e.g. the star formation rate and the slope of the initial mass function (Haywood, Robin & Crézé 1997).

An increasingly popular approach to fitting is to use Bayesian optimization over a broad set of free parameters (e.g. Catena & Ullio 2010). As a worked example, in Appendix A, we summarize the GALAXIA framework for fitting up to 20 disk parameters − this code is freely available at http://sourceforge.net/p/galaxia/wiki/Home/. The approach is theoretically simple and allows for useful constraints on local kinematic properties. The framework incorporates a constant star formation rate and a 3D Galactic dust model. Uniquely, it is designed to correct for an arbitrary survey selection function and can be used to fit data to analytic functions or numerical simulations (Sharma et al. 2011).

Sharma et al. (2014) apply the method in Appendix A to the RAVE and GCS surveys by assuming the structural form of the disk $f(r)$ and then attempting to fit for $f(v|r)$ from the surveys. They use *only* sky position and velocity for each star as these are the most accurate measurables. No distance information is supplied other than what is implicit in the model

fitting. They fit both the Gaussian DF and the dynamically-motivated Shu DF (Sharma & Bland-Hawthorn 2013); the latter performs better because it allows for asymmetric velocity distributions (relative to the Sun) due to non-circular motions experienced by most stars.

Groups that use Bayesian optimization (Bovy & Tremaine 2012; Sharma et al. 2014) typically fit for (i) the age-velocity dispersion relation (see below); (ii) the radial scalelengths ($R^{\rm t}_{\sigma,R}$, $R^{\rm T}_{\sigma,R}$) of the velocity dispersion profile; (iii) the mean stellar motion $\bar{v}_\phi$ with vertical height $z$; and (iv) the solar motion ($\mathbf{v}_\odot$). The RAVE team find that earlier estimates of the local standard of rest (LSR) are unreliable if they neglect the vertical dependence of the mean azimuthal motion for a given population. Ultimately, even after this correction, global kinematic measures like $\Theta_0$ are expected to have systematic uncertainties because of the initial assumption on $f(r)$ and the lack of dynamical consistency. We return to these measures in the next section.

**5.3.1. Age-velocity dispersion relation (AVR).** It is well established that the velocity dispersion of a disk stellar population $\sigma(R,\phi,z)$ increases with age (Strömberg 1925; Wielen 1977). Disks heat because a cold thin disk occupies a small fraction of phase space, and fluctuations in the gravitational field cause stars to diffuse through phase space to regions of lower phase space density. These effects are very difficult to model reliably through numerical simulations. For the thin disk, the AVR is sometimes approximated as a power-law in cosmic time (e.g. Aumer & Binney 2009) such that

$$\sigma(R,\phi,z) = \sigma_0(R,\phi,z)\left(\frac{\tau+\tau_{\rm min}}{\tau_{\rm max}+\tau_{\rm min}}\right)^{\beta_{R,\phi,z}} \quad (1)$$

where $(\tau_{\rm min},\tau_{\rm max})$ are priors. The power-law indices $(\beta_R,\beta_\phi,\beta_z)$ provide important information on disk heating parameters (Binney 2013; Sellwood 2013); a summary of estimates is given in Table 4. The widely used value of $\beta = 1/3$ dates back to the cloud scattering model of Spitzer & Schwarzschild (1953). While useful, this form is not universally accepted (e.g. Freeman 2001; Quillen & Garnett 2001); it makes no allowance for the thick disk which must be treated separately. From existing data, it is very difficult to distinguish a continually rising AVR from one that steps or saturates at old ages (Aumer & Binney 2009; Casagrande et al. 2011). Some groups attempt to fit for age-metallicity trends in the thin disk but such fits are less instructive at the present time (q.v. Freeman & Bland-Hawthorn 2002), although ultimately this information will need to be accommodated in a successful model (Sanders & Binney 2015).

**5.3.2. Velocity dispersion profile.** Pasetto et al. (2012) used the RAVE survey to learn about the variation of velocity dispersion in the $(R,z)$ plane. They used singular value decomposition to compute the moments of the velocity distribution. As expected, the thin disk stars follow near circular, co-rotational orbits with a low velocity dispersion (e.g. Edvardsson et al. 1993; Reddy et al. 2003). The velocity dispersion falls as a function of distance $R$ from the Galactic Centre, consistent with theoretical expectation (Cuddeford & Amendt 1992).

In an exponential disk, the stellar dispersion declines radially with the disk surface density $\Sigma^t$ and scale height $z^{\rm t}$ as $\sigma^t(R) \propto \sqrt{z^t(R)\,\Sigma^t(R)}$. Sharma et al. (2014) combined equation 1 with an exponential factor in radius (cf. van der Kruit 1986) in order to determine the radial scalelengths ($R^{\rm t}_{\sigma,R}$, $R^{\rm T}_{\sigma,R}$) of the dispersion profile (e.g. Lewis & Freeman 1989). For an isothermal disk, $R_\sigma$ is expected to be roughly twice the disk density scalelength

**Table 4 Comparison of measured or quoted $\beta$ indices in the age-velocity dispersion relation from stellar kinematic surveys. The quoted errors are statistical and do not include systematic errors that are typically larger.**

| Reference | Survey | $\beta_R$ | $\beta_\phi$ | $\beta_z$ |
|---|---|---|---|---|
| Nordstrom et al. (2004) | GCS | $0.31 \pm 0.05$ | $0.34 \pm 0.05$ | $0.47 \pm 0.05$ |
| Seabroke & Gilmore (2007) | GCS | - | - | $0.48 \pm 0.26$ |
| Holmberg et al. (2007) | GCS | 0.38 | 0.38 | 0.54 |
| Holmberg et al. (2009) | Hipparcos, GCS | 0.39 | 0.40 | 0.53 |
| Aumer & Binney (2009) | Hipparcos, GCS | 0.31 | 0.43 | 0.45 |
| Just & Jahrei$\beta$ (2010) | Hipparcos | - | - | 0.38 |
| Sharma et al. (2014) | GCS | 0.20±0.02 | 0.27±0.02 | 0.36±0.02 |
| Sharma et al. (2014) | RAVE | 0.19±0.02 | - | 0.3-0.4 |
| Sanders & Binney (2015) | SEGUE | 0.33 | - | 0.4 |

(Bottema 1993). The RAVE study confirms that the dispersion profile declines with radius, yielding estimates of $R^{\rm t}_{\sigma,R} \sim 14$ kpc and $R^{\rm T}_{\sigma,R} \sim 7.5$ kpc. The thick disk value is in good agreement with a full dynamical analysis which we return to below. The thin disk is insufficiently constrained in the RAVE survey because the elevated sightlines in latitude do not extend far enough in radius and are susceptible to vertical dispersion gradients (cf. Piffl et al. 2014a; Sanders & Binney 2015).

Bovy, Rix & Hogg (2012a) divided up the SEGUE survey into MAPs and argued that these constituted quasi-isothermal populations. (We refer the reader to Sanders & Binney (2015) for a different perspective on how to treat chemical information in fitting Galactic models.) Bovy found no break in vertical dispersion between the old thin and thick disk and suggested that the thick disk is a continuation of the thin disk rather than a separate entity (cf. Schönrich & Binney 2009). In contrast, kinematic and dynamic studies − which include a star formation history and an age-velocity dispersion relation explicitly for the thin disk − do tend to find a break in the vertical stellar dispersion (e.g. Table 5). Future studies that exploit improved stellar ages and chemistry will be needed to resolve this issue.

**5.3.3. Solar motion and LSR.** Delhaye (1965) determined the solar motion $\mathbf{v}_\odot$ with respect to the Local Standard of Rest (LSR) defined in the reference frame of a circular orbit that passes through the Sun's position today. Formally, for a coordinate system based at the Sun, where the $\mathbf{i}$ unit vector points towards the Galactic Centre, $\mathbf{j}$ in the direction of rotation, and $\mathbf{k}$ is upwards from the disk, $\mathbf{v}_\odot = U_\odot \mathbf{i} + V_\odot \mathbf{j} + W_\odot \mathbf{k}$. Delhaye studied different spectral classes and luminosity groups, and arrived at $\mathbf{v}_\odot \approx (9, 12, 7)$ km s$^{-1}$ that is very respectable by modern standards.

The random stellar motions of a given population is a strong function of their mean age, colour, metallicity and scaleheight. Care must be taken to account for the asymmetric drift of stellar populations in taking the limit to the zero-dispersion LSR orbit. Using Strömberg's relation, Dehnen & Binney (1998) measured $(U_\odot, V_\odot, W_\odot) = (10.0,\ 5.2,\ 7.2)$ km s$^{-1}$ from the HIPPARCOS survey, which for two ordinates are in excellent agreement with Delhaye's early estimates. $V_\odot$ was later revised upwards close to the original value (Binney 2010; Schönrich et al. 2010); the latter paper showed that Strömberg's linear asymmetric drift relation is invalidated by the metallicity gradient in the disk. Our values for $\mathbf{v}_\odot$ in the margin note are averaged over most estimates since Delhaye's original estimate. We have removed extreme outliers and ignored early values from any researcher who revised these at

a later stage using a similar method. Thus, the Sun is moving inwards towards the Galactic Centre, upwards toward the NGP and, given $z_0$, away from the plane.

While $(U_\odot, W_\odot)$ have converged on Delhaye's original values within the errors (see the margin note), some uncertainty surrounds $V_\odot$ when considered across the APOGEE, RAVE and LEGUE surveys (Bovy et al. 2012d; Sharma et al. 2014; Tian et al. 2015). One reason for this may arise from local kinematic substructure or any systematic streaming motion $\mathbf{v}_{\rm str}$ in the Sun's vicinity (Dehnen 2000; Antoja et al. 2014; Siebert et al. 2011; Williams et al. 2013). A local spiral arm density wave, for example, can impose kinematic fluctuations of order 10 km s$^{-1}$ (Siebert et al. 2012). In addition, because the corotation radius of the Galactic bar may be as close as $\sim$2 kpc inward from the Sun (§4.4), systematic streaming velocities may exist in the local Galactic disk due to perturbations from the bar and adjacent spiral arms. These could cause deviations of the zero-dispersion LSR orbit from the *average* circular velocity at $R_0$, defined as the angular rotation velocity of a 'fictitious' circular orbit in the axisymmetrically averaged gravitational potential, the so-called *rotational standard of rest* (RSR, see Shuter 1982; Bovy et al. 2012d). Analysing two mostly independent samples of stars from APOGEE, RAVE and GCS, Bovy et al. (2015) modelled the disk velocity field over $\sim$3-4 kpc scales and found such effects, with an implied tangential LSR streaming velocity of $14 \pm 3$ km s$^{-1}$ relative to the RSR. On the other hand, Sharma et al. (2014) find little difference in $V_\odot$ between the local GCS survey and the RAVE data which extends to $\sim$2 kpc, and Reid et al. (2014) when fitting their maser velocities with a circular orbit velocity field find no evidence for a deviation of the globally fitted $V_\odot$ from the locally determined value. Globally determined values of $U_\odot$ (Bovy et al. 2012d; Reid et al. 2014) agree well within errors with the locally determined $U_\odot = 10 \pm 1$ km s$^{-1}$. Here we adopt $|\mathbf{v}_{\rm str}| = 0^{+15}$ km s$^{-1}$ because we cannot establish clear agreement on the magnitude of the streaming motion at the present time. Future studies are anticipated which compare the impending GAIA data with models including the central bar and spiral density waves in view of understanding both the random and streaming motions in the disk.

$U_\odot$: 10.0±1 km s$^{-1}$, solar motion in $U$

$V_\odot$: 11.0±2 km s$^{-1}$, solar motion in $V$

$W_\odot$: 7.0±0.5 km s$^{-1}$, solar motion in $W$

$|\mathbf{v}_\odot|$: 15.5±3 km s$^{-1}$, solar vector motion

$|\mathbf{v}_{\rm str}|$: $0^{+15}$ km s$^{-1}$, LSR streaming motion

**5.3.4. Vertex deviation.** Binney et al. (2014) revisit the RAVE data but include distance estimates using Burnett et al. (2011). These were not employed by Sharma et al. (2014) because RAVE distances are susceptible to uncertainties in proper motions and stellar parameters, e.g. log-g (Zwitter et al. 2010; Anguiano et al. 2015). After excluding young stars, Binney finds that the velocity dispersion for a given stellar population increases as one moves vertically in $z$ from the plane (cf. Smith et al. 2009). Furthermore, at any location in $(R, z)$, the velocity ellipsoid's long axis (vertex deviation) points towards the Galactic Centre (see Fig. 12), indicating that the radial and vertical motions of stars are intimately coupled (cf. Siebert et al. 2008; Bond et al. 2010). This important result demonstrates that the stellar motions in $R$ and $z$ are entwined through the Galactic potential.

## 5.4. Stellar dynamics

Kinematic models offer greater freedom than physics really allows. This can lead to systematic errors in parameter estimation which typically swamp the statistical errors in the optimization scheme. The way forward is to consider dynamical models such that the spatial density distribution of stars and their kinematics are linked by the gravitational potential $\Phi$, under the assumption that the system is in steady state. At present, dynamical models are used to estimate a subset of parameters explored by kinematic methods

**Table 5 Parameter estimates from Galactic dynamical models with disk fitting[a].**

| Parameter | M11 | B12[a] | BR13[b] | P14 | SB15 | BP15 |
|---|---|---|---|---|---|---|
| Kinematic data | HI | GCS | SEGUE | RAVE | SEGUE | RAVE |
| $R_0$ (kpc) | 8.3 | [8.0-8.4] | [8.0] | [8.3] | [8.0] | [8.3] |
| $\Theta_0$ (km s$^{-1}$) | 239 | [220-241] | 218 | [240] | [220] | [240] |
| $M_{200}$ ($M_\odot$) | $1.3\times10^{12}$ | - | - | $1.3\times10^{12}$ | - | $1.4\times10^{12}$ |
| $M_{\rm bary}(M_\odot)^c$ | $7.1\times10^{10}$ | - | $6.8\times10^{10}$ | $5.6\times10^{10}$ | - | $6.2\times10^{10}$ |
| $f_{\rm bary}(\%)^d$ | 4.9 | - | - | 4.3 | - | 4.2 |
| $R^{\rm t}$ (kpc) | 3.0 | 2.7-3.1 | 2.2 | 2.7= | 2.3 | 3.7= |
| $R^{\rm T}$ (kpc) | 3.3 | 2.1-3.6 | - | 2.7= | 3.5 | 3.7= |
| $R^{\rm t}_{\sigma,R}$(kpc)$^e$ | - | 3.6-20 | - | 9.0= | 7.8= | $2\times R_{\rm d}$= |
| $R^{\rm t}_{\sigma,z}$ (kpc) | - | - | - | 9.0= | 7.8= | $2\times R_{\rm d}$= |
| $R^{\rm T}_{\sigma,R}$ (kpc) | - | - | - | 13 | 6.2= | 11.6 |
| $R^{\rm T}_{\sigma,z}$ (kpc) | - | - | - | 4.2 | 6.2= | 5.0 |
| $\sigma^{\rm t}_R$ (km s$^{-1}$) | - | 40-42 | - | 34 | 48 | 35 |
| $\sigma^{\rm t}_z$ (km s$^{-1}$) | - | 20-27 | - | 25 | 31 | 26 |
| $\sigma^{\rm T}_R$ (km s$^{-1}$) | - | 25-28 | - | 51 | 51 | 53 |
| $\sigma^{\rm T}_z$ (km s$^{-1}$) | - | 33-65 | - | 49 | 51 | 53 |

[a] The thin and thick disks are treated separately for two distinct potentials and parameter sets (b, c). [b] $M_{\rm bary}$ has been rescaled to $R_0$= 8.3 kpc for ease of comparison with other results. [c] $M_{\rm bary}$ includes the stellar disk, the bulge and the cold gas disk; the M11 total stellar mass has been corrected for a gas mass of $0.7\times10^{10}M_\odot$ in line with the other references, except that BP15 assumes a gas mass of $1.7\times10^{10}M_\odot$. $M_{200}$ assumes a spherical halo ($q = 1$) with $q < 1$ leading to higher values; $M_{\rm bary}$ does not include the Galactic corona; thin disk dispersions are evaluated at 10 Gyr. $df_{\rm bary}$ is the ratio of $M_{\rm bary}$ to the total galaxy mass. [e] $R_\sigma$ is a parameter that sets the scale of the outward radial decline in velocity dispersion within the disk. Note: All models (except M11) apply Bayesian fitting of action integrals. Key: [...] indicates a prior; '=' indicates values locked in fitting for $R_{\rm d}$. References: M11 - McMillan (2011); B12 - Binney (2012); BR13 - Bovy & Rix (2013); P14 - Piffl et al (2014a); SB15 - Sanders & Binney (2015); BP15 - Binney & Piffl (2015).

(see Table 5). While there has been good progress in recent years, with the first signs of dynamical self-consistency beginning to emerge, there is no fully consistent framework at the present time. We refer the reader to Rix & Bovy (2013, §6) for a useful summary of the dynamical methods on offer.

Early methods that operate locally or in annular bins (e.g. Bienayme, Robin & Creze 1987; Just & Jahreiss 2010) have given way to holistic treatments over one or more dynamical components of the Galaxy (e.g. Piffl et al. 2014a; Sanders & Binney 2015). Dynamical models assume an equilibrium figure such that the phase space density of stars $f(\mathbf{x},\mathbf{v})$ links only to the phase space coordinates through the constants of motion (Jean's theorem).

Binney (2010, 2012) has argued that action integrals ($\mathbf{J}$) are ideal for building dynamical models because they are adiabatic invariants. The most convenient action integrals are (i) $L_z$, the approximate symmetry axis of the Galaxy's angular momentum, (ii) $J_z$, to describe the action of a star perpendicular to the plane, and (iii) $J_R$, to describe the radial action of the star. The DF at any point in the Galaxy has the form $f(L_z, J_z, J_R)$. $\Phi$ is derived through an iterative process starting with an initial guess $\Phi_i$ to get to the density $\rho_i = \int f\ d^3v$ integrated over the phase-space volume $v$. Poisson's equation is used to compute an updated $\Phi_{i+1}$ and the process is repeated until convergence is achieved. The numerical procedures are non-trivial and computationally expensive, but entirely feasible

for surveys involving thousands of stars (Binney & McMillan 2011).

Of the few action integral studies of the disk to date, we highlight the work of Binney (2012) using GCS; Bovy & Rix (2013) and Sanders & Binney (2015) using SEGUE; Piffl et al. (2014a) and Binney & Piffl (2015) using the RAVE survey. In Table 5, these studies attempt to arrive at unbiassed parameter estimates through fitting the data with a consistent dynamical model. Binney (2012) introduced important new ideas in model fitting, including the use of the quasi-isothermal DF to model the disk. But his focus on a very local sample led to the disk dispersions being underestimated due to the GCS bias towards younger stars. As we return to below, this work has been superseded by Piffl et al. (2014a) who determined the DF from the RAVE giants. The RAVE survey comprises roughly equal numbers of dwarfs and giants, most within about 2.5 kpc of the Sun, and is thus more representative of the extended disk (Sharma et al. 2011).

Bovy & Rix (2013) build on Binney (2012) using 16300 G dwarfs from the SEGUE survey. They divide stars in the $(\alpha, \mathrm{Fe})$ abundance plane into MAPs: the more metal-rich MAPs trace the inner disk whereas the metal-poor populations trace the disk beyond the Solar Circle. Their goal is to measure the Galactic disk's mass profile by identifying a radius for each MAP where the modelling gives a tight (statistical) constraint on the local surface density. It is unclear whether (a) most MAPs can be treated as quasi-isothermal populations; and (b) the constraints at different radii from the MAPs are mutually consistent, i.e. free of systematic errors (e.g. Sanders & Binney 2015). The disk scalelength is the most important unknown in disentangling the contributions from the disk and the dark halo to the mass distribution near the disk. In contrast to the photometric radial profile, without dynamical consistency, *the mass-weighted radial profile cannot have been reliably measured in earlier kinematic studies.*

Sanders & Binney (2015) revisit the SEGUE analysis and instead treat the chemical (and phase) space as a continuous distribution. They introduce the idea of an 'extended distribution function' (EDF) $f(\mathbf{J}, \mathbf{Z})$ in place of the DF $f(\mathbf{J})$ where $\mathbf{Z}$ defines the chemical domain. While different abundance groups can have very diverse kinematics, they all necessarily reside within the same Galactic potential; the extra information in the EDF allows for a more accurate treatment of the selection function and associated errors across the survey. They determine that the thick disk vertical dispersion $\sigma_z^{\mathrm{T}}$ is a factor of two larger than the thin disk value ($\sigma_z^{\mathrm{t}} \approx 25$ km s$^{-1}$), in agreement with Sharma et al. (2014) and Piffl et al. (2014a). Unlike either of these studies, they obtain sensible numbers for both $R_{\sigma,R}^{\mathrm{t}}$ and $R_{\sigma,R}^{\mathrm{T}}$ for the first time, with a disk scalelength $R^{\mathrm{t}}$ ($\approx 2.3$ kpc) 35% smaller than the thick disk $R^{\mathrm{T}}$ (Table 5), but in conflict with the APOGEE survey (Hayden et al. 2015). (While $R_\sigma$ defines the scale of the outward decline of the stellar dispersion, it is not the exponential radial scalelength used in the kinematic studies because DFs are expressed in terms of integrals of motion, not radii.) Sanders & Binney state that their analysis is only preliminary because $\Phi$ was kept fixed throughout. Arguably, this study comes closest to the ideal of chemodynamical self-consistency. In the margin note, we adopt the RAVE velocity dispersions (Piffl et al. 2014a) as these are consistent across studies and extend further into the lower latitudes of the disk.

$\sigma_R^{\mathrm{t}}$: 35±5 km s$^{-1}$, old thin disk radial velocity dispersion at $R_0$

$\sigma_z^{\mathrm{t}}$: 25±5 km s$^{-1}$, old thin disk vertical velocity dispersion at $R_0$

$\sigma_R^{\mathrm{T}}$: 50±5 km s$^{-1}$, thick disk radial velocity dispersion at $R_0$

$\sigma_z^{\mathrm{T}}$: 50±5 km s$^{-1}$, thick disk vertical velocity dispersion at $R_0$

**5.4.1. Vertical density and acceleration.** Measurements of the local baryon and dark matter density have a long tradition in astronomy (Kapteyn 1922). From a survey of K giants towards the SGP, (Kuijken & Gilmore 1989) went further and attempted to derive the vertical density profile $\rho(z)$ and the gravitational acceleration $K_z$ induced by the local disk

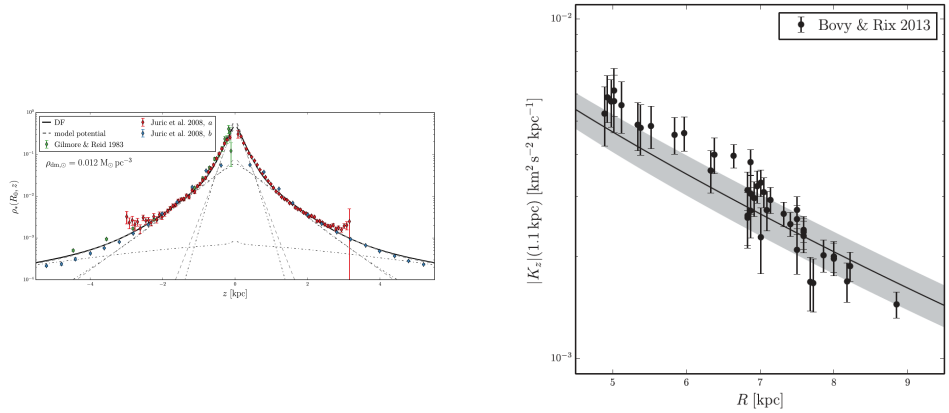


**Figure 14**

(Left) The vertical density profile at the position of the Sun where the data points are from Gilmore & Reid (1983) and Jurić et al. (2008). The total density from the potential (sum of disk, bulge and halo), shown as a dashed line, follows the predicted total density from the DF using the dynamical model shown as a solid line. The model fit exhibits a high degree of dynamical consistency over the local disk. (Right) Estimates of $K_z$ over the radial range $5 < R < 9$ kpc at a vertical height of $z = 1.1$ kpc. The data points are from the SEGUE dwarf survey (Bovy & Rix 2013) and the solid line (grey band) (uncertainty) is a dynamical model fit to the RAVE survey (Piffl et al. 2014a). While the data have a slightly shorter scale length compared to the RAVE model, there is a moderate dynamical consistency between them (Courtesy of Piffl et al. 2014a).

that are related through Poisson's equation $\nabla.K_z = -4\pi G\rho$. This is transformed into a surface density $\Sigma$ such that

$$\Sigma = -\frac{K_z}{2\pi G} + \Delta\Sigma \tag{2}$$

evaluated over the column $z = \pm 1.1$ kpc or $z = \pm\infty$. As McKee, Parravano & Hollenbach (2015) point out, this must be done with care. The usual assumption that $\Delta\Sigma = 0$ for a flat rotation curve at the midplane leads to an error because, in this instance, the rotation curve cannot be flat at a fixed height off the plane. In any event, this is a difficult measurement to get right because stellar surveys are strongly biassed towards more distant stars (cf. Zheng et al. 2001).

We can be confident that we *do* understand the local acceleration of the disk and the make-up of the local density (§ 5.4.2) over a vertical distance of $|z| = 1.1$ kpc (Kuijken & Gilmore 1989; Bovy & Tremaine 2012). A dynamical fit to 200,000 giants in the RAVE survey (Piffl et al. 2014a) leads to a local determination of $K_z$ and its local gradient (Fig. 5.4) which are in generally good agreement with the SEGUE dwarf analysis.

The vertical density profile $\rho(z)$ determined by Gilmore & Reid for dwarf stars has survived the test of time. Modern surveys are either too shallow (e.g. 2MASS) or too deep (e.g. SEGUE) to properly represent the disk although good agreement is found with the SDSS dwarf photometry (Jurić et al. 2008) after careful re-analysis (Piffl et al. 2014a). Binney et al. (2014) note that the kinematics of the cool dwarfs and giants in RAVE are consistent, such that dynamical model fits for giants or dwarfs can reasonably adopt Gilmore & Reid (1983) as a starting point, as has been done by most dynamical studies.

Given Gilmore & Reid (1983) or a similar density profile (e.g. Kuijken & Gilmore 1989),

the dynamical modelling attempts to find a self-consistent mass model-DF pair. *This means that the mass distribution of the stellar disk implied by the DF in the potential is consistent with the mass distribution of the stellar disk assumed in the mass model.* The action integral analysis of Piffl et al. (2014a) used ∼200,000 giants in the RAVE survey. In Fig. 5.4, they find remarkable dynamic self-consistency in the local disk as defined above. Moving away from the solar neighbourhood, they infer a declining vertical force with $R$ as expected, in good agreement with the Bovy & Rix (2013) analysis of SEGUE dwarfs ($5 < R < 9$ kpc). The latter study derived a mass-weighted scalelength of $R_{\rm M} = 2.15 \pm 0.14$ kpc, smaller than the $R_{\rm M} = 2.68$ kpc (without a quoted error) inferred by the RAVE analysis. $R_{\rm M}$ is dynamical by nature and is blind to the separate contributions of the ISM and the thin/thick disks.

**5.4.2. Local mass budget.** In a new study, McKee, Parravano & Hollenbach (2015) revise the local baryon inventory of Flynn et al. (2006) in light of new observations. Inter alia, they update the present day stellar mass function, and the vertical distributions and extents of both gas and stars. They find the baryon surface density integrated to infinity is $\Sigma_{\rm bary} \approx 47 \pm 3$ M$_\odot$ pc$^{-2}$ comprising brown dwarfs (1.2 M$_\odot$ pc$^{-2}$), white dwarfs (4.9 M$_\odot$ pc$^{-2}$), ISM gas (13.7 M$_\odot$ pc$^{-2}$), main sequence and giants (27.0 M$_\odot$ pc$^{-2}$). Interestingly, that least understood of main sequence stars - the M dwarf - makes up more than half of all stars by mass locally. Over the column $z = \pm 1.1$ kpc, there is general agreement that the *total* surface density (baryons + dark matter) is $\Sigma_{\rm tot} \approx 70 \pm 5$ M$_\odot$ pc$^{-2}$ (Kuijken & Gilmore 1989; Catena & Ullio 2010; McMillan 2011; Bovy & Rix 2013; Piffl et al. 2014a).

In terms of *local* density, the proportion of each mass constituent is very different due to the wide spread in scaleheights. McKee, Parravano & Hollenbach (2015) give the local mass density as $\rho_{\rm tot} \approx 0.097 \pm 0.013$ M$_\odot$ pc$^{-3}$ ($0.49 \pm 0.13$ GeV cm$^{-3}$) comprising stars ($0.043 \pm 0.04$ M$_\odot$ pc$^{-3}$), gas ($0.041 \pm 0.04$ M$_\odot$ pc$^{-3}$), baryons ($0.084 \pm 0.04$ M$_\odot$ pc$^{-3}$), and dark matter ($0.013 \pm 0.003$ M$_\odot$ pc$^{-3}$).

$\Sigma_{\rm tot}$: 70±5 M$_\odot$ pc$^{-2}$, total mass surface density $|z| \leq 1.1$ kpc at $R_0$

$\rho_{\rm tot}$: 0.097±0.013 M$_\odot$ pc$^{-3}$, local mass density at $R_0$

$\epsilon_{\rm tot}$: 0.49±0.13 GeV cm$^{-3}$, local dark matter energy density at $R_0$

## 5.5. Outer disk

The physical extent and detailed structure of the outer disk is highly uncertain. Over the years, different authors have claimed evidence for an "edge" in the stellar disk in the range $R_{\rm GC} = 10 - 15$ kpc from both optical and infrared surveys (Habing 1988; Robin, Creze & Mohan 1992; Ruphy et al. 1996; Minniti et al. 2011). When looking at external galaxies, what appear to be edges can be inflexions in the stellar density, i.e. a break in the exponential density profile. Such "breaks" are common (Pohlen & Trujillo 2006) but "continuously exponential" disks are also known and the stars can extend to the observed edge of the HI disk (Bland-Hawthorn et al. 2005; Irwin et al. 2005; Ellis & Bland-Hawthorn 2007).

Many new observations confirm that the outer disk is very complicated. The outer disk warps slowly away from the Galactic Plane in both HI (May et al. 1993) and stars (Carney & Seitzer 1993). In addition to the warp, the outer disk flares in both stars and gas and possesses a fair degree of substructure. Moni Bidin, Carraro & Méndez (2012) review the contradicting claims for the flaring stellar disk, but the comprehensive study of Momany et al. (2006) puts the issue beyond doubt. Carraro (2015) reviews the evidence for flaring in the outer disk in both young (HII regions, open clusters) and old stellar populations (cepheids, pulsars). The earlier claims of a disk edge did not consider the effect of a warping, flaring disk such that there is *no* strong evidence for a truncation to date

in either old or young populations (López-Corredoira et al. 2002; Sale et al. 2009; Carraro et al. 2010).

A complicating factor is the presence of the near-planar Monoceros Ring at $R_{\rm GC} \approx 15-20$ kpc (radial width $\approx 2$ kpc) which appears to corotate at roughly the speed of the outer disk (Newberg et al. 2002; Ibata et al. 2003). The nature of this stream is unknown (cf. Xu et al. 2015): unlike the Canis Major overdensity which may be related to the warp, the ring appears to have its own identity after correcting for the warp (Momany et al. 2006), and may even rotate slightly faster than the disk (Ivezić et al. 2008).

Before the optical studies, HI observations by Burton (1988) and Diplas & Savage (1991) identified Galactic gas out to at least $R_{\rm GC} \sim 25-30$ kpc (see also Hartmann & Burton 1997). Molecular gas clouds are seen to $R_{\rm GC} \gtrsim 20$ kpc, some with ongoing star formation (Yasui et al. 2008; Kobayashi et al. 2008). Further evidence for recent star formation out to these distances is the presence of young stars and open clusters (Carraro et al. 2010; Magrini et al. 2015). Remarkably, Kalberla & Dedes (2008) have pushed the HI frontier to $R_{\rm GC} \sim 60$ kpc which is within range of the orbiting Magellanic Clouds. The stellar/gaseous warp may be highly transient, triggered by the passage of the MC or Sgr dwarfs, with bending waves that travel at $\pi G\Sigma/\omega \sim 20$ kpc Gyr$^{-1}$ near the Solar Circle; $\Sigma$ and $\omega$ are the local surface density and angular velocity of the disk respectively.

## 6. Halo

In this section, we review the stellar, gaseous, and dark matter halos of the Galaxy, and finally put together a global rotation curve for the Milky Way. This analysis brings together many of the key themes of the review. The stellar and dark matter halos share the property that they are three-dimensional structures surrounding the disk and still grow by accreting matter. However, they do not necessarily share the same structural properties or formation histories. The gaseous halo is an important repository for a part of the Galaxy's baryonic mass, and interacts with the environment through inflows and outflows.

All three components live in the same gravitational potential, which at intermediate radii ($\sim R_0$) is shaped by the Galactic bulge, disk and dark halo, and at large ($\sim 100$ kpc) radii is completely dominated by the dark matter. One important goal of studying the halo and the satellites around the Milky Way is to map out the large-scale gravitational potential - this is a major science goal of the ongoing GAIA mission.

### 6.1. Stellar halo

The Milky Way's stellar halo, although containing just $\sim 1\%$ of the total stellar mass, is an important component for unravelling our Galaxy's formation history. It was first identified as a population of old, high-velocity, metal poor stars near the Sun, similar to the stars in globular clusters. The halo stars showed large random motions, little if any rotation, and a spheroidal to spherical spatial distribution. Following the influential paper of Eggen, Lynden-Bell & Sandage (1962), the classical view of the halo developed, of a smooth envelope of ancient stars from the time when the Galaxy first collapsed. Subsequently, Searle & Zinn (1978) suggested that the halo is built up from independent infalling fragments, based on their observation that halo globular clusters showed a wide range of metal abundances independent of Galactocentric distance.

Modern data from large stellar surveys show that the stellar halo has a complex structure

with multiple components and unrelaxed substructures, and continues to accrete matter in the form of smaller galaxies which are then tidally disrupted in the gravitational field (e.g., Ibata et al. 1997; Belokurov et al. 2006; Schlaufman et al. 2009). This confirms the predictions of hierarchical galaxy formation models. Because of the long dynamical timescales in the halo, tidal tails, shells, and other overdensities arising from accreted dwarf galaxies remain observable over Gyrs, thus constituting a fossil record of the Milky Way's accretion history. Previous reviews on this subject can be found in Helmi (2008); De Lucia (2012); Belokurov et al. (2013).

Cosmological simulations reveal that the Galaxy should have accreted $\sim 100$ satellite galaxies which would mostly have been disrupted by the tidal field, causing the build-up of the stellar halo. Irregular density distributions are predicted in the outer halo due to shells and tidal streams, with a large variance between different galaxies of the same dark matter halo mass. In these models, the majority of the halo is often built at early times, $\sim 10\,$Gyr ago, and most of the stellar halo stars come from the disruption of one or a few massive satellites accreted early-on. The outer halo is built more recently than the inner halo and the halo properties evolve, reflecting the history of accretion (Bullock & Johnston 2005; Font et al. 2006; De Lucia & Helmi 2008; Cooper et al. 2010; Pillepich et al. 2014).

Part of the inner halo may have formed *in situ*, i.e., within the main body of the Galaxy (Abadi, Navarro & Steinmetz 2006). Recent simulations suggest that a fraction of stars formed in the early Galactic disk could have been ejected into the inner halo, and further in situ halo stars could have formed from gas stripped from infalling satellites (Font et al. 2011; McCarthy et al. 2012; Tissera et al. 2013; Pillepich, Madau & Mayer 2015; Cooper et al. 2015), but the quantitative importance of these processes is not yet fully understood. Observationally, evidence for a *dual halo* has been put forward by Carollo et al. (2007); Beers et al. (2012), but see Schönrich, Asplund & Casagrande (2014).

In this section we review the structural parameters of the Milky Way's stellar halo and put them in the context of these hierarchical models. Determination of the mass of the dark matter halo based on these data is discussed in §6.3.

**6.1.1. Halo flattening and average density profile.** The stellar density of the halo is important because it reflects the cumulative past accretion history of the Milky Way. It has been extensively studied using several tracers for which good distances can be determined, including RR Lyrae (typical distance accuracy $\sim 7\%$, Vivas & Zinn 2006), blue horizontal branch (BHB) stars ($\sim 5\%$, Belokurov et al. 2013), red giants (RGB, $\sim 16\%$, Xue et al. 2014), and near-main sequence turnoff stars (nMSTO, $\sim 10\%$ with multiple colors, Ivezić et al. 2008). RR Lyrae and BHB stars, which trace the old metal-poor populations, are rarer than RGB and nMSTO stars, but can reach to $r \sim 100\,$kpc galactocentric radius. RGB trace all halo populations and currently reach to about $r \sim 50\,$kpc, whereas nMSTO stars are abundant and best for the inner halo, i.e. $r \lesssim 20\,$kpc.

A significant fraction of these halo tracer stars is found in large substructures (§6.1.2). Subtracting these leads to an estimate of a *smooth halo* component (e.g., Deason, Belokurov & Evans 2011), which however may contain smaller, yet unresolved substructures (e.g., Sesar et al. 2013). The spatial distributions of the halo stars are typically fitted by spherical or axisymmetric density models with single (SPL) or double (DPL) power-law or Sersic radial profiles, and with one or two flattening parameters for the inner and outer halo; Table 6 shows recent results based on DPL models. The inner halo flattening is found $q_{\rm in} = 0.65 \pm 0.05$ across various studies based on data reaching down to $R \sim 5\,$kpc (see

**Table 6 Recent measurements of stellar halo density parameters**

| Reference | Tracer | $r$ [kpc] | -$\alpha_{\rm in}$ | $q_{\rm in}$ | $r_s$ [kpc] | -$\alpha_{\rm out}$ |
|---|---|---|---|---|---|---|
| Xue et al. 2015 | RGB | $10-60$ | $2.1\pm0.3$ | $0.70\pm0.02$ | $18\pm1$ | $3.8\pm0.1$ |
| Pila-Diez et al. 2015 | nMSTO | $10-60$ | $2.5\pm0.04$ | $0.79\pm0.02$ | $19.5\pm0.4$ | $4.85\pm0.04$ |
| Sesar et al. 2011 | nMSTO | $5-35$ | $2.62\pm0.04$ | $0.70\pm0.02$ | $27.8\pm0.8$ | $3.8\pm0.1$ |
| Deason et al. 2011 | BHB/S | $10-45$ | $2.3\pm0.1$ | $0.59\pm0.03$ | $27.1\pm1$ | $4.6\pm0.15$ |
| Faccioli et al. 2014 | RRL | $9-49$ | $2.8\pm0.4$ | 0.7 fixed | $28.5\pm5.6$ | $4.4\pm0.7$ |
| Sesar et al. 2013 | RRL | $5-30$ | $1-2.7$ | $0.63\pm0.05$ | $16\pm1$ | $2.7\pm0.3$ |
| Sesar et al. 2010 | RRL | $9-49$ | $2.8\pm0.2$ | 0.7 fixed | $34.6\pm2.8$ | $5.8\pm0.9$ |
| Watkins et al. 2009 | RRL | $9-49$ | $2.1\pm0.3$ | 0.59 fixed | $26.9\pm3.1$ | $4.0\pm0.3$ |

Halo density parameters from recent studies of halo tracer stars with oblate double power-law models. Columns give reference, tracer used, covered Galactic radius range, inner power law slope, inner halo axis ratio, break radius, and outer power-law slope (in these models, the outer $q_{\rm out} = q_{\rm in}$). Watkins et al. (2009) and Sesar et al. (2010) considered spherical DPL models; the numbers given in these lines are from a reanalyis by Faccioli et al. (2014).

**Halo density:**

$\alpha_{\rm in}$: $-2.5\pm0.3$ Inner density slope

$\alpha_{\rm out}$: $-$(3.7-5.0) Outer density slope

$r_s$: $25\pm10$ kpc Break radius

$q_{\rm in}$: $0.65\pm0.05$ Inner halo flattening

$q_{\rm out}$: $0.8\pm0.1$ Outer halo flattening

also Bell et al. 2008; Jurić et al. 2008). The inner power-law slope is encompassed by $\alpha_{\rm in}=-2.5\pm0.3$. (The quoted formal fit errors are often quite small, but this could easily depend on the chosen parametric form, the data volume, and on remaining substructures in the data.) No evidence is found for an outward gradient in $q$ for the RR Lyrae and BHB samples, but Xue et al. (2015) with RGB and Pila-Díez et al. (2015) with nMSTO find an increase to $q_{\rm out}=0.8$ by $r=30$ kpc.

There is clear evidence that the stellar halo profile steepens with radius; see Table 6. In the context of DPL models based on data reaching $r\sim50$ kpc, the break radius between the inner and outer components scatters in the range $r_s=25\pm10$ kpc. For RRL and BHB, the outer power-law slope is in the range $\alpha_{out}=-4.5\pm0.5$, and Deason et al. (2014) found an even steeper profile beyond 50 kpc. For RGB the slope is somewhat shallower, $\alpha_{\rm out}=-3.8\pm0.1$. The overall density profile is similar to an Einasto function (e.g., Xue et al. 2015), and qualitatively similar to density profiles predicted by halo formation models (Bullock & Johnston 2005; Cooper et al. 2010). Deason et al. (2013) use simulations to show that a distinct density break may be related to the accumulation of stars at their apocenters, following relatively massive accretion events. Lowing et al. (2014) point out that the measured density parameters depend strongly on the surveyed sightlines and halo accretion history.

**6.1.2. Stellar halo mass and substructure fraction.** Estimating the stellar halo mass from these density distributions is non-trivial, requiring determination of the mass normalisation per halo tracer star from stellar population models and calibrations, as well as extrapolating beyond the survey volume through models. Bell et al. (2008) fitted DPL models to SDSS nMSTO stars and found a best-fit stellar halo mass within $r=1-40$ kpc of $\sim(3.7\pm1.2)\times10^8\,M_\odot$. Deason, Belokurov & Evans (2011) gave an estimate for the ratio of BHB stars per luminosity of $\sim10^{-3}$, using data for Galactic globular clusters. With a mass-to-light ratio $M/L_V=1.4\pm0.5$ for metal-poor Galactic globular clusters (Kimmig et al. 2015), the estimated stellar halo mass within $10-45$ kpc becomes $\sim3\times10^8\,M_\odot$.

The Milky Way halo contains numerous substructures which contain a significant fraction of its stellar mass (see Belokurov et al. 2013, for a review). The four largest stellar structures are the Sagittarius Stream, the Galactic Anti-Center Stellar Structure, the Virgo

Overdensity, and the Hercules-Aquila Cloud. Estimated masses for these structures are, respectively, $\sim 0.8 - 1.5 \times 10^8\ M_\odot$ based on the luminosity from Niederste-Ostholt et al. (2010) and $M/L_V = 1.4 \pm 0.5$ from Kimmig et al. (2015); $\sim 10^8\ M_\odot$ (Yanny et al. 2003; Belokurov et al. 2013), $\lesssim 10^6\ M_\odot$ (Bonaca et al. 2012) (iv) $\sim 10^7\ M_\odot$ based on Belokurov et al. (2007), alltogether summing to $\sim$ 2-3 $\times\ 10^8\ M_\odot$. A significant fraction of this substructure mass is within the volume traced by the SDSS nMSTO stars. We therefore add $\sim 50\%$ of this mass to the result of Bell et al. (2008) to obtain a rough estimate for the total stellar halo mass $M_s =$ 4-7 $\times\ 10^8\ M_\odot$. This is somewhat lower than the classical value based on Morrison (1993).

**Halo mass:**

$M_{\rm sub}$: 2-3 $\times\ 10^8\ M_\odot$
Substructure mass

$M_s$: 4-7 $\times\ 10^8\ M_\odot$
Total stellar halo mass

Bell et al. (2008) also quantified the fraction of mass in substructures from the ratio of the rms deviation of the density of nMSTO stars to the total density given through a smooth halo model. They find $\sigma/{\rm total} = 40\%$, arguing that much of the halo was accreted from satellite galaxies. In their study of BHB stars, Deason, Belokurov & Evans (2011) found a lower $\sigma/{\rm total} \sim 5 - 20\%$ with some increase for fainter stars (larger distances); on this basis they argue for a smooth halo with superposed additional substructures. Reasons for the discrepancy between both studies could be the less accurate nMSTO distances, leading to blurring of compact substructures, the lower resolution with the rarer BHB stars, or because the BHB stars trace an older, more mixed population of stars (Deason, Belokurov & Evans 2011). Resolving this issue requires large samples of stars with accurate distances and velocities. The problem is that even a fully accreted halo will eventually mix to be smooth above a given scale, and that mixing times are shortest in the high-density inner regions.

**6.1.3. Halo rotation, velocity dispersion and anisotropy.** Bond et al. (2010) analyzed the largest sample so far of halo star velocities within $\sim$ 10 kpc from the Sun, including $\sim 10^5$ SDSS stars with three velocity components. They found (i) a mean rotation of halo stars (their Fig. 5) of $\overline{v}^{\rm s}_\phi \simeq \Theta_0 + V_\odot - 205$ km s$^{-1}$ $\simeq 40$ km s$^{-1}$ for our adopted $\Theta_0 = 238$ km s$^{-1}$ and $V_\odot = 10.5$ km s$^{-1}$ (§6.4); (ii) a velocity ellipsoid whose principal axes align well with spherical coordinates; and (iii) corresponding halo velocity dispersions $(\sigma^{\rm s}_r, \sigma^{\rm s}_\theta, \sigma^{\rm s}_\phi) = (141, 75, 85)$ km s$^{-1}$, with a total error in each component of $\sim 5$ km s$^{-1}$. These values are in excellent agreement with results from Smith et al. (2009). Note that the close alignment of the halo velocity ellipsoids with spherical coordinates does not imply a spherical potential (see Evans et al. 2016).

**Local halo kinematics:**

$(\sigma^{\rm s}_r, \sigma^{\rm s}_\theta, \sigma^{\rm s}_\phi)$:
$(141, 72, 85)$ km s$^{-1}$ ($\pm 5$ km s$^{-1}$)
Spherical velocity ellipsoid

$\overline{v}^{\rm s}_\phi$: $\sim 40$ km s$^{-1}$
Mean rotation

Fig. 15 shows the radial velocity dispersion profile in the outer halo based on several data sets. $\sigma_r(r)$ sharply decreases from the local 141 km s$^{-1}$ to 100 km s$^{-1}$ at $r \sim 20$ kpc, then remains approximately flat until $r \sim 70$ kpc, and finally decreases to about 35 km s$^{-1}$ at $\sim 150$ kpc. At the largest radii, where the stellar density profile is largely unknown (see Table 6), the very low $\sigma_r$ values are consistent with a tidal truncation of an extrapolated steep $n \propto r^{-4.5}$ power-law (Kafle et al. 2014).

Tangential velocities can be estimated from the variation of LOS velocities across the sky and from proper motions. Fermani & Schönrich (2013) used BHB stars reaching to $r \sim 50$ kpc and with both kinds of methods find no rotation in either the inner or outer halo, and no trend with metallicity. Tangential velocity dispersions and the spherical anisotropy parameter $\beta(r)$ were determined in the outer halo by several authors and are shown in Fig. 15. The radial anisotropy $\beta = 0.5 - 0.7$ at small and large radii is consistent with predictions for accreted halos (Abadi, Navarro & Steinmetz 2006). The tangential anisotropy at radii around $r \sim 17$ kpc was confirmed by King et al. (2015) but was suggested to be

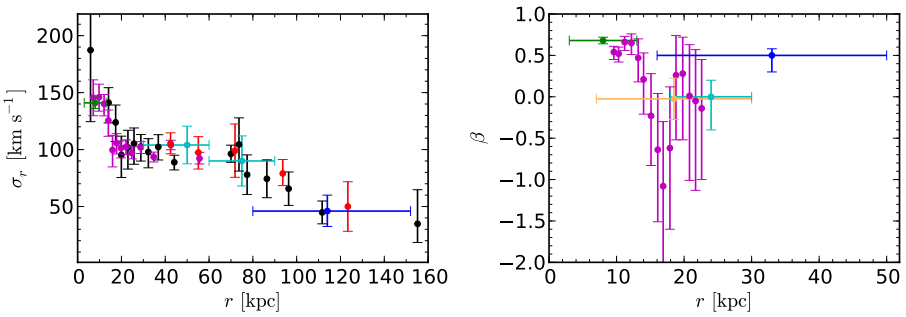


**Figure 15**

Left: radial velocity dispersion profile for several outer halo tracers, including nMSTO stars (Bond et al. 2010, green), BHB stars (Kafle et al. 2012, purple) and (Deason et al. 2013, blue), blue straggler stars (Deason et al. 2012, cyan), K-giants (Kafle et al. 2014, black), and mixed tracers (Battaglia et al. 2005, red). Right: measurements of orbital anisotropy in the halo, for nearby (Bond et al. 2010, green) and distant nMSTO stars (Deason et al. 2013, cyan), and BHB stars (Kafle et al. 2012, purple), (Sirko et al. 2004, yellow), and (Deason et al. 2012, blue).

transient based on orbit simulations (Bird & Flynn 2015), perhaps due to a yet unknown substructure in the halo.

## 6.2. Hot halo

The existence of a diffuse hot plasma (or corona) surrounding the Galactic disk has been widely discussed since Spitzer's early observation that the ubiquitous HI clouds must be confined by an external medium (Spitzer 1956). But it remains uncertain how much of the gas lies close to the Galactic plane, and how much of it extends into the halo. Strong evidence for extended coronae have come from the first reliable detections of hot halos around nearby massive disk galaxies (e.g. Anderson & Bregman 2011). The Galactic corona also explains the remarkable observation of gas depletion in all dwarfs within a radius of about 270 kpc, with the exception of the high-mass LMC and SMC dwarfs (Grcevich & Putman 2009), which is well understood in terms of ram-pressure stripping by a hot medium (Nichols & Bland-Hawthorn 2011; Gatto et al. 2013). Such an extended hot phase is supported by numerical simulations (Nuza et al. 2014) which focus on the properties and distribution of the multiphase gas in and around two simulated galaxies chosen as an M31-Galaxy analogue. They found the hot ($T \gtrsim 10^5$K) gas has a uniform temperature profile around each of the simulated galaxies, and good agreement between the observed profile (Miller & Bregman 2015) and the density profile of the simulated Galaxy.

We tabulate the most recent observations of the Galactic corona in Table 7. The best evidence for a hot corona comes from bright AGN sight lines with detections of OVII and OVIII in absorption, and in high-resolution x-ray spectra (Paerels & Kahn 2003) of a nearly ubiquitous soft x-ray background (SXRB) with energies $0.1 - 1.0$ keV (implying temperatures $\sim 10^{6-7}$ K), with some contribution of OVII and OVIII in emission (Snowden et al. 1997; Henley & Shelton 2012). The sensitivity of current x-ray spectroscopy limits OVII and OVIII detections to a handful ($\sim 30$) of sight lines. There is an additional difficulty in disentangling the contribution of the Local Bubble, a supernova remnant in which the Solar

**Table 7 Estimates of gas density and temperature in the Galactic halo (corona).**

| Reference | $d$ [kpc] | $n_p$ [$10^{-5}$cm$^{-3}$] | $T_e$ [$10^6$K] | $M_{\rm hot}$[$10^{10}$M$_\odot$] | Method |
|---|---|---|---|---|---|
| BR00 | $\lesssim 250$ | $\gtrsim 2.4^a$ | $1-1.4$ | 1 | ram-pressure stripping of gas in dwarf spheroidals |
| S+02 | $15^b$ | 100 | $1^d$ | – | pressure equilibrium between HVCs (MS) and coronal gas |
| | $45^b$ | 30 | $1^d$ | | |
| S+03 | $\approx 70$ | $1-10$ | $>1$ | – | OVI absorption (100 LOS) |
| BR07 | $<20$ | $90^c$ | $2^d$ | $0.04^f$ | OVII absorption (25 LOS) uniform spherical halo |
| AB10 | $50^e$ | $50^{a,c}$ | 3.5 | $1.2-1.5$ | LMC pulsar dispersion measures |
| G+13 | $50-90$ | $36-13^a$ | $1.8^d$ | $3.4-4.8$ | ram-pressure stripping of gas in Carina and Sextans |
| MB15 | $10-100$ | $200-4^a$ | $2^d$ | $2.7-4.7$ | OVII / OVIII emission (650 LOS) |
| S+15 | $48.2\pm5$ | $11\pm4.5$ | – | $2.6\pm1.4^g$ | ram-pressure stripping of the LMC disk |

Unless otherwise indicated, all coronal masses $M_{\rm hot}$ are integrated out to $r_{\rm vir}$; the gas density is quoted as a total particle density unless otherwise indicated. Notation: [a]Average density out to the given distance; [b]Distance from the Galactic plane; [c]Electron density; [d]Assumed; [e]Distance from the Sun; [f]Mass enclosed within 20 kpc; [g]Mass enclosed within $\sim 300$ kpc. References: BR00 - Blitz & Robishaw (2000); S+02 - Stanimirović et al. (2002); S+03 - Sembach et al. (2003); BR07 - Bregman & Lloyd-Davies (2007); AB10 - Anderson & Bregman (2010); G+13 - Gatto et al. (2013); MB15 - Miller & Bregman (2015); S+15 - Salem et al. (2015).

System is embedded (Snowden et al. 1990), and the contribution from solar wind charge exchange processes, which produce soft x-ray emission throughout the Solar System (Cravens, Robertson & Snowden 2001). Consequently, the detailed structure (density, temperature, entropy profile) of the Galactic corona, and hence its total mass, is uncertain.

The Galactic hot halo is likely to comprise two main components: one, exponentially decaying, high-metallicity ($Z > 0.3\ Z_\odot$) component with a scale height of a few kpc, which dominates the x-ray observations; and an extended ( $\gtrsim 100$ kpc), more diffuse, low-metallicity halo (Yao & Wang 2007). Purely exponential gas density profiles (i.e. not characterised by a single temperature) overpredict the coronal temperature and x-ray surface brightness by factors of a few (Fang, Bullock & Boylan-Kolchin 2013).

Early attempts to model the corona using x-ray observations assumed (unphysically) that it was isothermal and at a constant density (Bregman & Lloyd-Davies 2007; Gupta et al. 2012). The studies arrived at wildly different conclusions: the first study derived an electron density $n_e = 9\times10^{-4}\,{\rm cm}^{-3}$ at $r = 19$ kpc; the second found $n_e \geq 2\times10^{-4}\,{\rm cm}^{-3}$ at $r \geq 139$ kpc (cf. Wang & Yao 2012). Fang, Bullock & Boylan-Kolchin (2013) favoured a picture in which the corona is composed of adiabatic (isentropic) gas in hydrostatic equilibrium with the Galactic potential, in conflict with evidence that the Galactic halo is far from having a constant entropy profile (Miller & Bregman 2015; Crain et al. 2010). It is now well established that the halo temperature as inferred from x-ray observations is fairly uniform across the sky and with little scatter around $T \approx 2\times10^6$ K (Henley et al. 2010) although this does not demand that the halo is strictly isothermal.

A new all-sky catalog of OVII and OVIII emission lines (Henley & Shelton 2012) has

been studied by Miller & Bregman (2013) and Miller & Bregman (2015). They used this catalogue in combination with x-ray measurements to determine that the halo density is of order $10^{-5}\,\mathrm{cm}^{-3}$ to $10^{-4}\,\mathrm{cm}^{-3}$ at 10 kpc $\lesssim r \lesssim$ 100 kpc. They determine a coronal gas mass of $\sim 10^{10}\,M_\odot$ within $r \approx 250$ kpc. These results rely on key assumptions: (i) the density profile of the hot gas is well described by a spherically symmetric $\beta$-model of the form $n(r) \propto r^{-\beta/2}$, consistent with a truncated King model for the halo potential; (ii) the halo is isothermal with a temperature $T = 2 \times 10^6$ K; (iii) the gas is in collisional ionisation equilibrium. Miller & Bregman's model can be justified if the dark matter halo of the Galaxy is well described by a spherically symmetric isothermal sphere with a core radius $r_c \sim 0.1$ kpc, and if the gas is quasi-isothermal and in approximate hydrostatic equilibrium with the potential.

Tepper-Garcia, Bland-Hawthorn & Sutherland (2015) bring all of this work together and search for a physically plausible corona that is consistent with the observed stellar halo dynamics and with the UV/x-ray measurements (Table 7). They normalise the dark matter halo to the density profile and total mass inferred from the kinematics of halo stars (Kafle et al. 2012). If the dark matter halo is isothermal, the core radius is somewhat larger than inferred from Miller & Bregman's model, i.e. $r_c \approx 0.5$ kpc. The halo velocity dispersion implies a gas temperature of $T \sim 10^6$ K, leading to a density profile which is in broad agreement with Miller & Bregman (2015) and Nuza et al. (2014) with about the same total gas mass. The most likely baryonic mass range for the Galactic corona is $M_{\rm hot}$ $\sim 2.5 \pm 1 \times 10^{10}\,M_\odot$.

$M_{\rm hot}$: $2.5 \pm 1 \times 10^{10}\,M_\odot$; Galactic corona baryonic mass ($r \lesssim r_{\rm vir}$)

$M_{\rm bary,tot}$: $8.5 \pm 1.2 \times 10^{10}\,M_\odot$; Galactic total baryonic mass ($r \lesssim r_{\rm vir}$)

$f_{\rm bary}$: $7 \pm 1\%$; Galactic baryonic mass fraction

*The Galaxy's baryonic mass fraction.* The dynamical analyses presented in § 5.4 are relatively consistent in their estimates of the baryonic mass fraction of the Galaxy (stars + cold gas), i.e. $M_{\rm bary} \sim 6.3 \pm 0.5 \times 10^{10}\,M_\odot$ (Table 5). We now add the likely contribution from the hot corona $M_{\rm hot}$ within $R_{\rm vir}$ to arrive at a *total* baryonic mass, $8.8 \pm 1.2 \times 10^{10}\,M_\odot$. This leads to a baryonic mass fraction out to $R_{\rm vir}$ of $f_{\rm bary} = M_{\rm bary,tot}/M_{\rm vir} \approx 6 \pm 1\%$ which falls well short of the Universal value (≈16%; Hinshaw et al. 2003).

## 6.3. Dark halo

An accurate measurement of the Galaxy's total mass is central to our understanding of how it fits into the Cold Dark Matter paradigm. We need to know the mass of the dark matter which has had time to virialize in the Galaxy, the so-called virial mass $M_{\rm vir}$ defined within the virial radius $R_{\rm vir}$. There is some confusion in the literature on the convention for a galaxy's total mass, i.e. how it should be defined and at what epoch (Shull 2014). $M_{\rm vir}$ is usually expressed as the mass within a region around the centre in which the average density exceeds a multiple of the mean density of the Universe (either the closure density or the mass density). We follow the definition of Klypin et al. (2002) and Kafle et al. (2014) where $\rho_{\rm vir} = \Delta_{\rm vir}\Omega_{\rm M}\rho_{\rm crit}$ ($\Delta_{\rm vir} = 340$) such that

$$R_{\rm vir} = 258 \left(\frac{\Delta_{\rm vir}\Omega_{\rm M}}{102}\right)^{-1/3} \left(\frac{M_{\rm vir}}{10^{12}\,M_\odot}\right)^{1/3} \quad \mathrm{kpc} \tag{3}$$

Since the mass enclosed depends on the product $\Delta_{\rm vir}\Omega_{\rm M}$, our values are within 5% of estimators that use $(\Delta_{\rm vir}, \Omega_{\rm M}) = (360, 0.27)$ (e.g. van der Marel et al. 2012a). Note that if the dark matter can be represented by an NFW halo, its scalelength is $r_h \approx 25$ kpc assuming a concentration parameter $c \approx 10$ (Fig. 1; van der Marel et al. 2012a). Another widely used mass estimator is $M_{200}$ where the average density within $r_{200}$ is $\rho_{200} = 200\rho_{\rm crit}$,

**Table 8 Total mass estimates for the Galaxy.**

| Reference | Method | $M_{200}$ | $M_{100}$ | $M^r_{\rm kpc}$ | $R_{200}$ | $R_{100}$ | $r$ |
|---|---|---|---|---|---|---|---|
| Wilkinson et al. 1999 | Distribution function based | 1.67 | 2.39 | 0.54 | 243.9 | 346.0 | 50 |
| Sakamoto et al. 2003 | Mixed halo object kinematics | 1.67 | 2.39 | 0.54 | 243.9 | 346.0 | 50 |
| Dehnen et al. 2006 | Halo star kinematics | 1.75 | 1.96 | 1.05 | 247.7 | 324.3 | 120 |
| Smith et al. 2007 | Escape velocity | 1.03 | 1.43 | 0.39 | 207.7 | 291.7 | 50 |
| Xue et al. 2008 | Halo star kinematics | 0.87 | 0.91 | 0.40 | 196.1 | 267.0 | 60 |
| Gnedin et al. 2010 | Hypervelocity star kinematics | 1.33 | 1.74 | 0.69 | 226.4 | 311.3 | 80 |
| Watkins et al. 2010 | Satellite galaxy kinematics | 2.62 | 3.05 | 2.70 | 283.4 | 375.4 | 300 |
| McMillan 2011 | Modeling local observables | 1.26 | 1.76 | 0.84 | 222.0 | 312.7 | 100 |
| Kafle et al. 2012 | Halo star kinematics | 1.21 | 1.99 | 0.21 | 219.1 | 325.5 | 25 |
| Deason et al. 2012 | Halo star kinematics | 0.87 | 1.03 | 0.75 | 196.0 | 261.9 | 150 |
| Gonzalez et al. 2013 | Satellite galaxy kinematics | 1.15 | 1.39 | - | 215.3 | 289.0 | - |
| Kafle et al. 2014 | Halo star kinematics | 0.72 | 0.80 | - | 184.2 | 239.1 | - |
| Piffl et al. 2014b | Escape velocity | 1.60 | 1.90 | - | 235.0 | 322.0 | - |
| Gibbons et al. 2014 | Stream modeling | 0.55 | 0.68 | 0.41 | 168.7 | 227.3 | 100 |

$M_\Delta$ is the mass within the radius defined with respect to the overdensity $\Delta$ (see text); the radius computed by the author is indicated by $R_\Delta$. $M^r_{\rm kpc}$ is the mass within radius $r$ in kpc as indicated. All masses are in units of $10^{12}{\rm M}_\odot$; all radii are in units of kpc.

which is 16% smaller than $M_{\rm vir}$ for our adopted parameters (Bryan & Norman 1998; Klypin et al. 2002). $M_{\rm vir}$ is not strictly a total mass because the dark matter profiles are thought to extend (and rapidly truncate) beyond the virial radius.

One constraint for the total mass of the Milky Way comes from the 'timing mass' argument (Kahn & Woltjer 1959): the masses of M31 and the Galaxy must be sufficient to overcome universal expansion to explain their present-day kinematics consistent with a head-on collision and a future merger in ∼6 Gyr (van der Marel et al 2012b). Timing mass estimates in early work (e.g. Li & White 2008) are now thought to be consistently too high. These have come down significantly due to improved relative motions for both galaxies and a more accurate estimate of the solar reflex motion (§6.4). By selecting galaxy pairs in the Millennium simulations (after Li & White), van der Marel et al. (2012a) determine a (virial) timing mass of $4.9 \pm 1.6 \times 10^{12}$ M$_\odot$ for the mass within the virial radius of both galaxies ($4.1 \pm 1.4 \times 10^{12}$ M$_\odot$ for r $\leq r_{200}$). After considering the orbit of M33 about M31, they further reduce the total timing mass to $M_{\rm vir,timing} = 3.2 \pm 0.6 \times 10^{12}$ M$_\odot$. Modern mass estimates for M31 reveal that it is comparable to the Milky Way (van der Marel et al. 2012a) such that the timing mass provides an upper limit of $M_{\rm vir} \lesssim 1.6 \times 10^{12}$ M$_\odot$ for the Galaxy.

Unlike the timing mass, most mass estimators are limited to the region explored by the available tracer population, whose spatial distribution and kinematics are used to estimate the enclosed mass. Estimates of the Milky Way's mass have been obtained based on the kinematics of halo stars, the kinematics of satellite galaxies and globular clusters, the evaluation of the local escape velocity, and the modelling of satellite galaxy tidal streams. Dynamical analysis of halo star kinematics typically results in relatively low total mass, $M_{200} \lesssim 10^{12}\ M_\odot$ (Xue et al. 2008; Deason et al. 2012; Kafle et al. 2012; Kafle et al. 2014). The main uncertainties in such determinations are the lack of stellar tangential velocities

from proper motions, and/or the need to extrapolate from spatially limited samples to the scale of the virial radius. Such extrapolation is often done using simulated galaxy halos, which then fixes the dark matter density profile, or by assuming parametric forms for the density distribution and fitting for the best parameters.

A list of direct mass determinations is compiled in Table 8. Mass estimates based on satellite and globular cluster kinematics typically result in higher values, $M_{200} = 1 - 2 \times 10^{12}\ M_\odot$ when the Leo I dwarf satellite galaxy is assumed to be bound to the Milky Way; on the other hand, if Leo I with its large line-of-sight velocity is considered unbound, values more similar to $M_{200} \lesssim 10^{12}\ M_\odot$ result (Wilkinson & Evans 1999; Li & White 2008; Watkins, Evans & An 2010). Satellite galaxies reach to larger radii, but here the main uncertainties come from small numbers and similarly lack of proper motion information. Determinations of the escape velocity from radial velocities of stars near the Sun also lead to $M_{200} = 1-2\times10^{12}\ M_\odot$ (Smith et al. 2007; Piffl et al. 2014b), again with the uncertainties of extrapolating the mass distributions to large radii. Modelling stellar positions and velocities along the orbit of the Sagittarius dwarf galaxy, or matching the apocentre radii of its trailing and leading arms, leads to a range of enclosed mass $M^{100}_{\rm kpc} = 0.4 - 2 \times 10^{11}\ M_\odot$ (Gibbons, Belokurov & Evans 2014). The Galaxy's mass can also be estimated by comparing Milky Way properties with various predictions of a CDM simulation, such as the number of satellite galaxies larger than a given mass (Cautun et al. 2014). But these estimates are not reliable until the models improve. Finally, McMillan (2011) determined a value for the Milky Way mass from fitting parameterized mass models to a range of observations.

$r_{\rm vir}$: $282 \pm 30$ kpc, Galactic virial radius scaled to $\Omega_M = 0.3$

$M_{200}$: $1.1 \pm 0.3 \times 10^{12}\ M_\odot$, Galactic mass within $R_{200}$

$M_{\rm vir}$: $1.3 \pm 0.3 \times 10^{12}\ M_\odot$, Galactic virial mass

The halo stellar kinematic studies comprise the largest and, arguably, the most reliable data sets. These estimates lead to a straight average for $M_{200} = 1.1 \pm 0.3 \times 10^{12}\ M_\odot$, or equivalently $M_{\rm vir} = 1.3 \pm 0.3 \times 10^{12}\ M_\odot$, consistent with the upper limit from the timing mass. Interestingly, if we derive M31's mass from a simple scaling of peak rotation, i.e. $(260\ \ {\rm km\ s^{-1}}/\Theta_0)^4 M_{\rm vir}$, or a mass that is 40% higher than the Galaxy, this leads to a virial timing mass for the Galaxy that is equal to our estimate for $M_{\rm vir}$ above. The Galaxy's virial mass cannot be much lower than $10^{12}\ M_\odot$ if it is to provide sufficient angular momentum to the observed baryons over its lifetime.

**6.3.1. Halo shape.** Besides the total halo mass, another property of considerable interest is the shape of the dark matter halo. In dark matter only simulations, halo shapes are strongly flattened, prolate-triaxial, with mean $< c/a >= 0.5 \pm 0.1$ (e.g., Dubinski & Carlberg 1991; Allgood et al. 2006). When baryons are included, the halos become more spherical and evolve towards oblate at all radii, but mostly in their inner parts (e.g., Kazantzidis et al. 2004; Bailin et al. 2005; Abadi et al. 2010). In the Milky Way, constraints on the shape of the dark halo are based on the Sgr orbit, tidal streams, on SDSS kinematics, on flaring of the HI layer, and on combining rotation curve and vertical acceleration measurements (see review by Read 2014).

The orbit of the Sgr dwarf, whose leading and trailing arms can each be followed $\sim 180^\circ$ across the sky, constrain the halo shape in the range $R =$ 20-100 kpc (Belokurov et al. 2013). The geometry of the stream on the sky has been shown to require an oblate near-spherical halo (Ibata et al. 2001; Johnston, Law & Majewski 2005), whereas line-of-sight velocities favour a prolate shape (Helmi 2004). Thus Law & Majewski (2010) proposed a triaxial halo model for the MW, in fact nearly oblate but with short axis in the plane of the disk, with questionable stability. For this reason, most authors continue to use spherical models for the outer halo (Ibata et al. 2013; Gibbons, Belokurov & Evans 2014).

On 20 kpc scales, Koposov, Rix & Hogg (2010) and Küpper et al. (2015) determined the flattening of the dark halo to be $q_z = 0.95 \pm 0.15$, i.e., essentially spherical, from modelling of the tidal streams of GD-1 and Pal 5. Loebman et al. (2012) claimed evidence for a strongly oblate shape from SDSS data. Kalberla et al. (2007) found evidence from HI data for a ring-like distribution of dark matter around $R \sim 15$ kpc. Near the Sun, the local shape of the dark matter halo is constrained by the ratio of the local dark matter density to the average enclosed spherical dark matter density (Garbari et al. 2012; Read 2014). Within large error bars the measurements are most consistent with a spherical or even prolate local halo shape (Garbari et al. 2012; Zhang et al. 2013; Bovy & Rix 2013), i.e., no dark disk (Read 2014). On the whole, constraints on the dark matter halo shape in the Milky Way are still weak and no consistent picture has yet emerged.

## 6.4. Rotation curve and baryon fraction profile

Compared to the extended distribution of dark matter, the baryonic mass component in the Milky Way is centrally concentrated and dominates the mass in the central few kpc. In this section, we review the total circular velocity at $R_0$ and the rotation curve of the Milky Way, and then use illustrative dynamical models to estimate the contribution of stars and gas to the rotation curve, as well as the baryon fraction as a function of radius.

**6.4.1. Solar tangential velocity.** We recall from §3.4 the total angular velocity of the Sun, $\Omega_{g,\odot} = 30.24 \pm 0.12$ km s$^{-1}$kpc$^{-1}$, derived from the VLBI PM of Sgr A$^*$ in the Galactic plane and the assumption that Sgr A$^*$ is at rest at the Galactic Center. For $R_0 = 8.2 \pm 0.1$ kpc (§ 3.2), the corresponding total solar tangential velocity is $V_{g,\odot} = 248 \pm 3$ km s$^{-1}$. These values agree within errors with a number of independent recent measurements: Modelling trigonometric parallaxes and PM of masers in HMSFR in the Galactic disk, Reid et al. (2014) derive $\Omega_{g,\odot} = 30.57 \pm 0.43$ km s$^{-1}$kpc$^{-1}$, giving $V_{g,\odot} = 251 \pm 5$ km s$^{-1}$. The analysis of the nearby velocity field from SEGUE by Schönrich (2012), at fixed $R_0 = 8.2$ kpc, results in $V_{g,\odot} = 248 \pm 6$ km s$^{-1}$. Bovy et al. (2012d) determine $V_{g,\odot} = 242^{+10}_{-3}$ km s$^{-1}$ from APOGEE data, while Sharma et al. (2014) obtain $V_{g,\odot} = 244$ km s$^{-1}$ from fitting RAVE data. Here we interpolated to $R_0 = 8.2$ kpc and estimate a systematic error $\sim 5$ km s$^{-1}$ from their results. Küpper et al. (2015) find $V_{g,\odot} = 254 \pm 16$ km s$^{-1}$ from modelling the tidal stream of Pal 5. In what follows we will use $V_{g,\odot} = 248 \pm 3$ km s$^{-1}$ from the PM of Sgr A$^*$.

**6.4.2. Circular velocity at $R_0$.** In an axisymmetric Galaxy, the circular velocity $\Theta_0$ is simply related to $V_{g,\odot} = (\Theta_0 + V_\odot)$. Here $V_\odot$ is the Sun's peculiar velocity along the direction of rotation with respect to the LSR, with the LSR defined as the streaming velocity of local stellar populations relative to the Sun in the limit of vanishing velocity dispersion (e.g., Schönrich et al. 2010). In §5.3.3 we estimated $V_\odot = 10.5 \pm 1.5$ km s$^{-1}$. In our barred Galaxy, the LSR could itself have an additional streaming velocity $V_{\rm LSR}$ relative to the circular velocity in the axisymmetrically averaged gravitational potential (the RSR, see §5.3.3), due to perturbations from the bar and spiral arms. As discussed in §5.3.3, our estimate for the total LSR streaming velocity is $|\mathbf{v}_{\rm str}| = 0^{+15}$ km s$^{-1}$, which could mostly be directed in the forward direction of rotation. If we take $V_{\rm LSR} = \pm|\mathbf{v}_{\rm str}| = 0 \pm 15$ km s$^{-1}$, $V_{g,\odot}$ and $\Theta_0$ are now related by $V_{g,\odot} = (\Theta_0 + V_{\rm LSR} + V_\odot)$; this results in $\Theta_0 = 238 \pm 15$ km s$^{-1}$ and $\Omega_0 = \Theta_0/R_0 = 29.0 \pm 1.8$ km s$^{-1}$kpc$^{-1}$.

*Oort's constants.* Traditionally, Oort's constants $A$ and $B$ were defined for the local disk as

$V_{g,\odot} = \Theta_0 + V_{\rm LSR} + V_\odot$: $248 \pm 3$km s$^{-1}$, Sun's total tangential velocity relative to Sgr A$^*$

$V_{\rm LSR}$: $0 \pm 15$km s$^{-1}$, tangential velocity of LSR relative to RSR

$\Theta_0$: $238 \pm 15$ km s$^{-1}$, circular rotation velocity at the Sun

$\Omega_o$: $29.0 \pm 1.8$ km s$^{-1}$kpc$^{-1}$, circular orbit frequency at the Sun

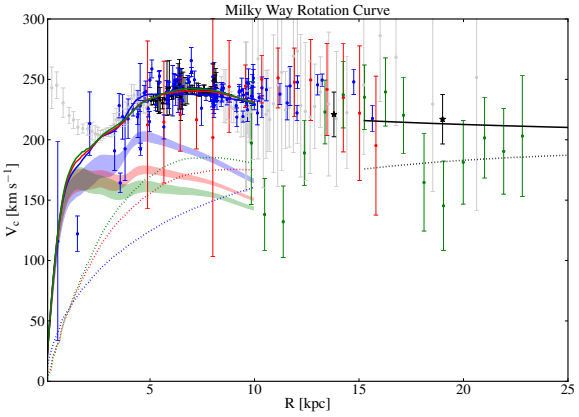


**Figure 16**

Galactic rotation curve. Sources for data points are: maser PM and RV associated with high mass disk stars (Reid et al. 2014, blue), inner Galaxy terminal velocities and outer disk velocities collected by Sofue, Honma & Omodaka (2009, black ($5\,\mathrm{kpc} < R < R_0$) and grey (elsewhere)), PM of disk RCG from López-Corredoira (2014, red), Jeans-equation converted RV data for BHB stars (Kafle et al. 2012, green), and stream modelling for GD-1 (Koposov, Rix & Hogg 2010) and Pal-5 (Küpper et al. 2015, black stars). All data were approximately converted to ($R_0 = 8.2$ kpc, $\Theta_0 = 238$ km s$^{-1}$). The coloured bands show azimuthally averaged circular velocities for illustrative dynamical models with bulge, long bar, disk, and dark halo (Portail et al. 2016). In the bulge region, these models are based on stellar kinematic data (Portail et al. 2015) and thus are more reliable than the (misleading) terminal velocities. The bulge and long bar *stellar* mass in these models corresponds to a Kroupa IMF ±10%, whereas the disk has fixed local stellar surface density 38 $M_\odot$ pc$^{-2}$ and scalelength $R_\mathrm{d} = (2.15, 2.6, 3.0)$ kpc (blue, red, green) and includes a gas disk with surface density 13 $M_\odot$ pc$^{-2}$ and twice the stellar scalelength. In each case, the lower band shows the rotation curve from the baryonic component, the dotted line shows the median dark halo profile, and the upper band shows the total rotation curve. In these models, the baryonic component provides $(86\%, 73\%, 65\%)$ of the circular velocity at $2.2R_\mathrm{d}$. The outer dotted and full lines show the rotation curves for an NFW halo with virial mass $M_\mathrm{vir} = 1.3 \times 10^{12}\,M_\odot$ (§6.3) and concentration $c = 16$ which matches with the inner halo at $R \simeq 12$ kpc, and for this NFW halo combined with the $R_\mathrm{d} = 2.6$ kpc disk.

a means to estimate the circular velocity $\Theta_0(R_0)$ and its gradient from radial velocity and PM data for nearby stellar populations, viz.

$$A - B = \Theta_0/R_0; \quad A + B = -(\partial\Theta/\partial R)_{R_0}. \tag{4}$$

The quantity $A - B$ has been measured by many authors for different stellar populations (Feast & Whitelock 1997; Uemura et al. 2000; Elias, Alfaro & Cabrera-Caño 2006) with values in the range $27 - 32$ km s$^{-1}$kpc$^{-1}$. For the rotation gradient $-(A + B)$, different authors find positive, zero and negative values. Catena & Ullio (2010) argue for $A + B = 0.18 \pm 0.47$ km s$^{-1}$kpc$^{-1}$ from an SDSS study of M stars (Fuchs et al. 2009).

**6.4.3. Rotation curve.** Figure 16 assembles rotation velocity measurements from various sources as explained in the caption. The data indicate a nearly flat rotation curve in the range $R = 5 - 13$ kpc (Reid et al. 2014) with a slight decrease at larger radii (Küpper et al. 2015; Kafle et al. 2012). PM data from GAIA will clarify this. The rotation velocities

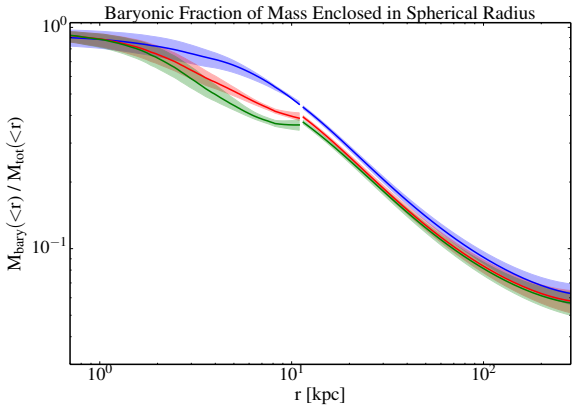


**Figure 17**

Fraction of baryonic mass within radius $r$ including the stellar and cold gas mass from the dynamical models shown in Fig. 16 and the additional mass in hot gas predicted by Tepper-Garcia, Bland-Hawthorn & Sutherland (2015) with an assumed uncertainty of 35% (§6.2).

determined by Sofue, Honma & Omodaka (2009, see also original references therein) from terminal velocities and a circular rotation model are unreliable in the region dominated by the Galactic bar (e.g., Englmaier & Gerhard 1999; Fux 1999), as is clearly visible in the central $\sim 3$ kpc. Points inside $R = 5$ kpc (the half-length of the Galactic bar, §4.3) are therefore plotted in light shade.

*Is the disk maximal?* As shown with the illustrative models in Fig. 16, the answer to this question largely depends on the disk (mass) scalelength. These models include a bulge with dynamical mass fitted to the BRAVA kinematic data and stellar mass corresponding to a Kroupa IMF $\pm 10\%$ (Portail et al. 2015). The disk has local stellar surface density $38\, M_\odot/\,\mathrm{pc}^2$ (Bovy & Rix 2013) and scalelengths $R_\mathrm{d} = 2.15$ kpc (Bissantz & Gerhard 2002; Bovy & Rix 2013), 2.6 kpc (Robin et al. 2003; Jurić et al. 2008) and 3.0 kpc (Kent, Dame & Fazio 1991; Gould, Bahcall & Flynn 1996) and includes a gas disk with surface density $13\, M_\odot/\,\mathrm{pc}^2$ and twice the stellar scalelength. A short scalelength $R_\mathrm{d}$ has important implications: the Galaxy's disk (summed over all stellar and gaseous components) is then *maximal* (Sackett 1997) in the sense that the disk and bulge dominate the rotation curve, i.e. contribute 85% of the rotational velocity and $\sim 70\%$ of the rotational support at $2.2R_\mathrm{d}$. We included the bulge in the definition here because it mostly originates from the disk, §4.2. For the three scalelengths shown, the baryonic component provides a median fraction $f_v = (86\%, 73\%, 65\%)$ of the circular velocity and $(74\%, 53\%, 42\%)$ of the radial force at $2.2R_\mathrm{d}$. Thus the Milky Way's disk is maximal only for the shortest scalelength (see also Sackett 1997; Gerhard 1999; Bovy & Rix 2013; Piffl et al. 2014a), but even for the longer $R_\mathrm{d}$ its contribution to the rotational velocity is at the upper limit of that inferred for typical spiral galaxies by Martinsson et al. (2013, $f_v = 0.4$-$0.7$), but see Aniyan et al. (2016).

**6.4.4. Baryonic mass fraction with radius.** The dynamical models shown in Fig. 16 have median total stellar masses of $(5.7, 5.0, 4.7) \times 10^{10}\, M_\odot$. Of this, the stellar mass of the bulge and the disk embedded in the bulge region is $\sim 1.5 \times 10^{10}\, M_\odot$, and the estimated mass

of the long bar is $\sim 1 \times 10^{10}\, M_\odot$ (§4). The remaining disk mass is nominally lower than given in §5 but the total mass is consistent with other dynamical mass estimates in the literature (Piffl et al. 2014a; Licquia, Newman & Brinchmann 2015). Adding the mass in cold gas and the $2.9 \times 10^{10}\, M_\odot$ in hot gas resulting from Tepper-Garcia, Bland-Hawthorn & Sutherland (2015) for the NFW halo shown in Fig. 16 ($M_{\rm vir} = 1.3 \times 10^{12}\, M_\odot$, §6.3, $c = 16$), the total baryonic mass fraction of the Galaxy becomes again $0.06 \pm 0.01$. The resulting total baryonic mass fraction within radius $r$ from stars, cold gas, and hot gas is shown in Fig. 17.

## 7. CONCLUDING REMARKS

The ultimate goal of Galactic research is to understand how the Milky Way has evolved from cosmological initial conditions to its present state, and how its future evolution will proceed. Our first task is to describe its current state in some detail; this allows us to connect to similar galaxies nearby and to studies of galaxies at high redshift. Characterizing the Galaxy's dominant components and measuring their main parameters is an important step in this process.

The last few years have seen significant progress in several areas, driven by the impressive data from past and on-going surveys such as SDSS, VVV, APOGEE and RAVE. We now have a quantitative description of the box/peanut structure of the Galactic bulge and, to a lesser extent, of its continuation into the Galactic plane, the long bar. We know that the thin and thick disks are distinct sequences in abundance ratios and age. The velocity field in the disk near the Sun has been charted, and dynamical models have been developed to link these data self-consistently to the gravitational potential. In the Galactic halo, multiple satellites and substructures have been discovered and density and velocity measurements have been made to beyond $> 50$ kpc. On the other hand, we still lack good understanding of, e.g., the radial scale-length of the large-scale Galactic disk, the transition region between the Galactic bar and the surrounding disk, the properties of the nuclear disk, the mass of the stellar halo, and the outer rotation curve of the Milky Way. Constructing a complete structural model for the Milky Way is one of the main challenges for the coming years.

Half of all stars in the Universe formed before a redshift of unity. Detailed chemistry for millions of stars will provide important new information on the early formation of the different components. Until recently, most of our understanding of stars has come from the solar neighbourhood, but high-resolution stellar surveys have now begun to reach more representative regions of the Galaxy. We still do not have a complete chemical inventory for any component over its full physical extent. In principle, such data for enough stars will enable chemical tagging of dynamically distinct sub-systems. If even a few disrupted stellar systems with different ages can be recovered, we can learn about the role of secular evolution and stellar migration over cosmic time from their dispersal across the disk (Bland-Hawthorn, Krumholz & Freeman 2010). But accurate elemental abundances are hampered by the difficulty of measuring good stellar parameters (e.g. log-g, effective temperature). The differential abundance technique shows great promise but this works best if the stars have a similar spectral type, thereby limiting the sample size. But we are encouraged by the revolution that is now under way to improve the state of the art in achieving consistent stellar abundances (Jofré et al. 2014; Ness et al. 2015).

We are looking forward to a golden age for Galactic research exemplified by ESA GAIA, the astrometric space mission that was successfully deployed at the end of 2013. The ongoing

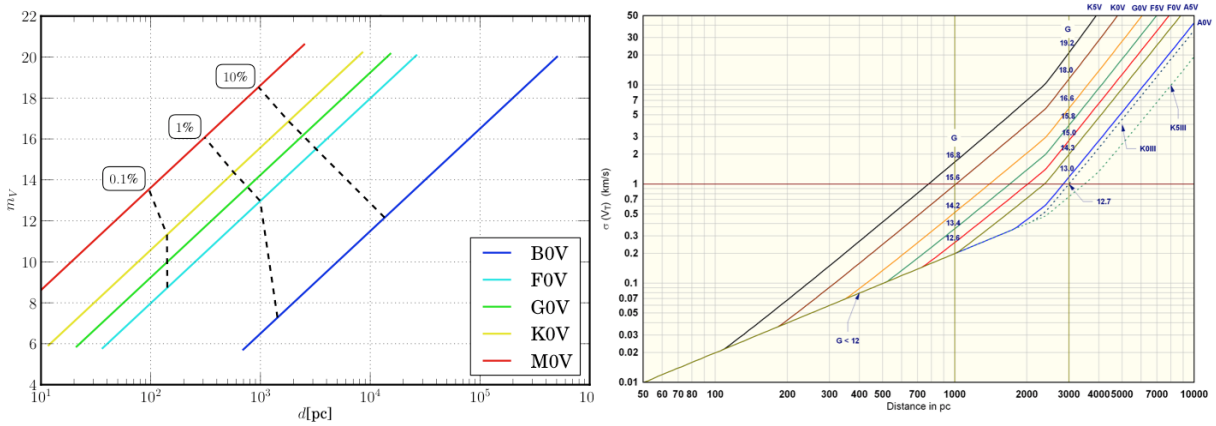


**Figure 18**

(Left) The distance accuracy of GAIA for dwarf stars: the 0.1%, 1% and 10% 'accuracy horizons' are shown as dashed lines as a function of $V$ magnitude. The different dwarf types are indicated by coloured lines. This figure is made with the `Pygaia` package developed by A.G.M. Brown (courtesy of Read 2014). (Right) The accuracy in the GAIA transverse velocity for dwarf stars as a function of their distance; the uncertainties arise from errors in both the proper motions and parallaxes (courtesy of Mignard 2011).

or upcoming deep all-sky photometric (DES, LSST, JWST, WFIRST), spectroscopic (APOGEE-2, GALAH, WEAVE, PFS, 4MOST) and seismological surveys (COROT, K2, TESS, PLATO) are well placed to advance our understanding of stellar populations. The large and extremely large telescopes will also play an important role, particularly with high-resolution spectroscopy (e.g. MOONS on VLT, G-CLEF on GMT).

The LSST co-added survey will reach up to four magnitudes deeper than SDSS: for stars with $0.2 < g - r < 0.6$ and $g < 23.5$, LSST will achieve a metallicity error of 0.1 dex for metal-rich stars and 0.2 dex for metal-poor stars for about 200 million F/G main sequence stars (Ivezić et al. 2008). In a single exposure, LSST will detect metal-poor MSTO stars to ∼140 kpc and horizontal branch stars and RR Lyrae to ∼500 kpc, going several times further in the final co-added data. LSST will also provide proper-motion measurements and parallaxes for stars below $r \sim 20$ where GAIA lacks sensitivity (Ivezić, Beers & Jurić 2012). This will revolutionize photometric parallax and metallicity studies such as reviewed in §4.

The GAIA astrometric mission will be even more far reaching for Galactic research. GAIA will have an enormous impact on our understanding of 6D phase space ($\mathbf{x}$, $\mathbf{v}$) for the stars, particularly in the near field, but with important new information for giants extending into the outer halo. By the end of the decade, it will have obtained positions and velocities for up to two billion stars, i.e. phase space information for a few percent of stars that dominate the visible light in the Galaxy. In Fig. 18(left), many F/G dwarfs to be observed by LSST will have distances and proper motions with 10% accuracy out to ∼ 3 kpc from the Sun. Moreover, in Fig. 18(right), dwarfs brighter than $V \sim 15$ will have transverse velocities at least as good as the measured radial velocities. Such precise 6D phase space information will allow us to unravel the complex chemistry and dynamics of the local disk components to unprecedented levels.

Putting all the different strands together is not going to be easy. Increasingly sophisticated dynamical methods will be needed to accommodate the 6D phase space information

in a complex multi-component potential, and to combine this with the chemical information $\mathcal{C}$([Fe/H],[$\alpha$/Fe], ...), but good progress is already being made (Hunt & Kawata 2014; Sanders & Binney 2015). Eventually, we will need to consider the departures from dynamical equilibrium which arise from internal evolution and interactions with the outside (Binney 2013).

The Galaxy resembles a complex organism which evolves in a self-regulated fashion according to the laws of gravity, star formation, dynamics, and chemical evolution, while subject to mass accretion and external influences from its cosmological neighbourhood. Its low gas content, position in the green valley of the colour-magnitude diagram, and secularly evolved central parts of old stars indicate that it is in its late stages of evolution.

N-body and hydrodynamic simulations are becoming increasingly useful to help understand both formation and evolutionary processes (Stinson et al. 2013; Minchev, Chiappini & Martig 2014; Feng et al. 2016; Scannapieco et al. 2015). These simulations will need to continue to grow in size to resolve smaller particle masses in both gas and dark matter, and to ultimately resolve individual star clusters. More thought must be given to how we "evaluate" the goodness of fit of a complex dynamical model, or a numerical simulation, when comparing to the high-dimensional data space available to Galactic researchers (Sharma et al. 2011). Through these comparisons Galactic studies will improve galaxy formation simulations and lead to a understanding of galaxy formation processes in general.

Ultimately, we may never arrive at a complete understanding of the Galaxy, much like any complex physical system. Most often, we learn about the physical laws through a series of approximations that become progressively more refined. But our search for understanding is noble all the same as we seek answers to the many wonders around us.

## 8. ONLINE VERSION: Analytic framework for fitting a parametric model to the Galaxy

We describe an analytic framework to model the Galaxy that is defined by a large set of kinematic parameters (Sharma et al. 2014). The framework is designed for rapid Bayesian optimization (e.g. Catena & Ullio 2010) and shares important features with most studies of this kind (e.g. Rix & Bovy 2013). The stellar content is modelled as a set of distinct components: the thin disk, the thick disk, the stellar halo and the bulge. The distribution functions, i.e., the number density of stars as a function of position ($\mathbf{r}$), velocity ($\mathbf{v}$), age ($\tau$), metallicity ($Z$), and mass ($m$) for each component, is assumed to be specified a priori as a function $f_j(\mathbf{r}, \mathbf{v}, \tau, Z, m)$ where $j$ ($= 1, 2, 3, 4$) runs over the four components. The form of $f_j$ that correctly describes all the properties of the Galaxy and is self-consistent is still an open question.

For a given Galactic component, we assume stars form at a rate $\Psi_j(\tau)$ with a mass distribution $\xi(m|\tau)$ (IMF) that is a function of age $\tau$, where the present day spatial distribution of stars $p(\mathbf{r}|\tau)$ is conditional on age only. For a velocity distribution $p(\mathbf{v}|\mathbf{r}, \tau)$ and metallicity distribution $p(Z|\tau)$, we have

$$f_j(\mathbf{r}, \mathbf{v}, \tau, m, Z) = \frac{\Psi(\tau)}{\langle m \rangle} \xi(m|\tau) p(\mathbf{r}|\tau) p(\mathbf{v}|\mathbf{r}, \tau) p(Z|\tau). \quad (5)$$

The functions take different forms for each Galactic component (Sharma et al. 2011). The IMF is normalized such that $\int_{m_{\rm min}}^{m_{\rm max}} \xi(m|\tau) dm = 1$ and $\langle m \rangle = \int_{m_{\rm min}}^{m_{\rm max}} m \xi(m|\tau) dm$ is

the mean stellar mass. The metallicity distribution is modeled as a log-normal distribution,

$$p(Z|\tau) = \frac{1}{\sigma_{\log Z}(\tau)\sqrt{2\pi}} \exp\left[-\frac{(\log Z - \log \bar{Z}(\tau))}{(2\sigma^2_{\log Z}(\tau))}\right], \tag{6}$$

the mean and dispersion of which are given by age-dependent functions $\bar{Z}(\tau)$ and $\sigma_{\log Z}(\tau)$. The $\bar{Z}(\tau)$ is widely referred to as the age-metallicity relation (AMR). For the thin disk, the well known "age-scale height" relation is given by the axis ratio $\epsilon$, viz.

$$\epsilon(\tau) = \mathrm{Min}\left(0.0791, 0.104\left(\frac{\tau/\mathrm{Gyr} + 0.1}{10.1}\right)^{0.5}\right). \tag{7}$$

*Kinematic model.* For a useful kinematic model, we want to constrain the velocity distribution $p(\mathbf{v}|\mathbf{r},\tau)$. We assume that everything except for $p(\mathbf{v}|\mathbf{r},\tau)$ on the rhs of Eq. (5) is known. The functional form for $p(\mathbf{v}|\mathbf{r},\tau)$ is restricted because the spatial density distribution and the kinematics are linked to each other via the potential. The accuracy of a pure kinematic model depends upon our ability to supply functional forms of $p(\mathbf{v}|\mathbf{r},\tau)$ that are a good approximation to the actual velocity distribution of the system. A proper way to handle this problem would be to use dynamically self consistent models, but such models are still under development. Here we explore kinematic models that provide a reasonable approximation to the actual velocity distribution.

*Gaussian velocity ellipsoid model.* In this model, the velocity distribution is assumed to be a triaxial Gaussian,

$$p(\mathbf{v}|\mathbf{r},\tau) \;=\; \frac{1}{\sigma_R\sigma_\phi\sigma_z(2\pi)^{3/2}} \exp\left[-\frac{v_R^2}{2\sigma_R^2}\right] \exp\left[-\frac{v_z^2}{2\sigma_z^2}\right] \times \exp\left[-\frac{(v_\phi - \overline{v_\phi})^2}{2\sigma_\phi^2}\right], \tag{8}$$

where $R, \phi, z$ are cylindrical coordinates. The $\overline{v_\phi}$ is the asymmetric drift and is given by

$$\overline{v_\phi}^2(\tau, R) \;=\; v_\mathrm{c}^2(R) + \sigma_R^2 \times \left(\frac{d\ln\rho}{d\ln R} + \frac{d\ln\sigma_R^2}{d\ln R} + 1 - \frac{\sigma_\phi^2}{\sigma_R^2} + 1 - \frac{\sigma_z^2}{\sigma_R^2}\right) \tag{9}$$

This follows from Eq. 4.227 in Binney & Tremaine (2008) assuming $\overline{v_R\, v_z} = (v_R^2 - v_z^2)(z/R)$. This is valid for the case where the principal axes of velocity ellipsoid are aligned with the $(r, \theta, \phi)$ spherical coordinate system. If the velocity ellipsoid is aligned with the cylindrical $(R, \phi, z)$ coordinate system, then $\overline{v_R\, v_z} = 0$. Recent results using the RAVE data suggest that the velocity ellipsoid is aligned with the spherical coordinates (Siebert et al. 2008; Binney et al. 2014). One can parametrize our ignorance by writing the asymmetric drift as follows:

$$\overline{v_\phi}^2(\tau, R) \;=\; v_\mathrm{c}^2(R) + \sigma_R^2 \left(\frac{d\ln\rho}{d\ln R} + \frac{d\ln\sigma_R^2}{d\ln R} + 1 - k_\mathrm{ad}^2\right) \tag{10}$$

This is the form used by Bovy & Tremaine (2012).

The dispersions of the $R, \phi$ and $z$ components of velocity increase as a function age due to secular heating in the disk, and there is a radial dependence such that the dispersion increases towards the Galactic Center. We model these effects after Aumer & Binney (2009) using the functional form

$$\sigma^{\mathrm{thin}}_{R,\phi,z}(R,\tau) \;=\; \sigma^{\mathrm{thin}}_{R,\phi,z,\odot} \exp\left[-\frac{R - R_0}{R^{\mathrm{thin}}_\sigma}\right] \times \left(\frac{\tau + \tau_{\min}}{\tau_{\max} + \tau_{\min}}\right)^{\beta_{R,\phi,z}} \tag{11}$$

$$\sigma^{\mathrm{thick}}_{R,\phi,z}(R) \;=\; \sigma^{\mathrm{thick}}_{R,\phi,z,\odot} \exp\left[-\frac{R - R_0}{R^{\mathrm{thick}}_\sigma}\right]. \tag{12}$$

The choice of the radial dependence is motivated by the desire to produce disks in which the scale height is independent of radius. For example, under the epicyclic approximation, if $\sigma_z/\sigma_R$ is assumed to be constant, then the scale height is independent of radius for $R_\sigma = 2R_d$ (van der Kruit & Freeman 2011). In reality there is also a $z$ dependence of velocity dispersions which we have chosen to ignore in our present analysis. This means that for a given mono age population the asymmetric drift is independent of $z$. However, the velocity dispersion and asymmetric drift of the combined population of stars are functions of $z$. This is because the scale height of stars for a given isothermal population is an increasing function of its vertical velocity dispersion.

*Shu distribution function model.* The Gaussian velocity ellipsoid model has its limitations. In particular, the distribution of $v_\phi$ is strongly non-Gaussian, being highly skew to low $v_\phi$. For a two-dimensional disk, a much better approximation to the velocity distribution is provided by the Shu (1969) distribution function. Moreover, the Shu DF, being dynamical in nature, connects the radial and azimuthal components of velocity dispersion to each other and to the mean-streaming velocity, thus lowering the number of free parameters in the model.

Assuming the potential is separable as $\Phi(R,z) = \Phi_R(R) + \Phi_z(z)$ we can write the distribution function as

$$f(E_R, L_z, E_z) = \frac{F(L)}{\sigma_R^2(L_z)} \exp\left[-\frac{E_R}{\sigma_R^2(L_z)}\right] \times \frac{\exp\left[-(E_z)/(\sigma_z^2(L_z))\right]}{\sigma_z(L_z)\sqrt{2\pi}},$$

where $L = Rv_\phi$ is the angular momentum,

$$E_z = \frac{v_z^2}{2} + \Phi_z(z) \tag{13}$$

$$E_R = \frac{1}{2}v_R^2 + \Phi_{\rm eff}(R, L_z) - \Phi_{\rm eff}(R_g, L_z) \tag{14}$$

with

$$\Phi_{\rm eff}(R, L_z) = \frac{L_z^2}{2R^2} + \Phi(R) \simeq \frac{L_z^2}{2R^2} + v_c^2 \ln R \tag{15}$$

being the effective potential. Let $R_g(L_z) = L_z/v_{\rm c}$ be the radius of a circular orbit with specific angular momentum $L_z$. In Schönrich (2012) (q.v. Sharma & Bland-Hawthorn 2013), it was shown that the joint distribution of $R$ and $R_g$ can be written as

$$P(R, R_g) = \frac{(2\pi)^2 \Sigma(R_g)}{g(\frac{1}{2a^2})} \exp\left[\frac{2\ln(R_g/R) + 1 - R_g^2/R^2}{2a^2}\right], \tag{16}$$

where $\Sigma(R)$ is a function that controls the disk's surface density and

$$a = \sigma_R(R_g)/v_{\rm c} \tag{17}$$

$$g(c) = \frac{e^c \Gamma(c - 1/2)}{2c^{c-1/2}}. \tag{18}$$

We assume $a$ to be specified as

$$a = a_0(\tau) \exp\left[-\frac{R_g}{R_\sigma}\right] = \frac{\sigma_{R,\odot}}{v_{\rm c}} \left(\frac{\tau + \tau_{\rm min}}{\tau_{\rm max} + \tau_{\rm min}}\right)^{\beta_R} \exp\left[-\frac{R_g - R_0}{R_\sigma}\right] \tag{19}$$

and $\sigma_z$ to be specified as

$$\sigma_{z0}(R_g, \tau) \;=\; \sigma_{z,\odot} \left( \frac{\tau + \tau_{\min}}{\tau_{\max} + \tau_{\min}} \right)^{\beta_z} \exp\left[ -\frac{R_g - R_0}{R_\sigma} \right]. \tag{20}$$

Now this leaves us to choose $\Sigma(R_g)$. This should be done so as to produce disks that satisfy the observational constraint given by $\Sigma(R)$, i.e., an exponential disk (or disks) with scale length $R_d$. A simple way to do this is to let

$$\Sigma(R_g) \;=\; \frac{e^{-R_g/R_d}}{2\pi R_d^2}. \tag{21}$$

However, this matches the target surface density only approximately. An alternative approach is to use the fast optimization formula proposed in Sharma & Bland-Hawthorn (2013) such that

$$\Sigma(R_g) \;=\; \frac{e^{-R_g/R_d}}{2\pi R_d^2} - \frac{0.00976 a_0^{2.29}}{R_d^2} s\left[ \frac{R_g}{(3.74 R_d (1 + q/0.523)} \right] \tag{22}$$

where $q = R_d/R_\sigma$ and $s$ is a function of the following form

$$s(x) \;=\; k e^{-x/b}((x/a)^2 - 1), \tag{23}$$

with $(k, a, b) = (31.53, 0.6719, 0.2743)$.

*The gravitational potential* $\Phi$. So far we have described kinematic models in which the potential is separable in $R$ and $z$. In such cases, the energy associated with the vertical motion $E_z$ can be assumed to be the third integral of motion. In reality, the potential generated by a double exponential disk is not separable in $R$ and $z$. For example, the hypothetical circular speed defined as $\sqrt{R \partial \Phi(R,z)/\partial R}$ can have both a radial and a vertical dependence, i.e.

$$v_c(R, z) \;=\; \sqrt{R \frac{\partial \Phi}{\partial R}} = \frac{\Theta_0 + \alpha_R (R - R_\odot)}{1 + \alpha_z |z/\text{ kpc}|^{1.34}}. \tag{24}$$

The parameters $\alpha_R$ and $\alpha_z$ control the radial and vertical dependencies, respectively. The motivation for the vertical term comes from the fact that the above formula with $\alpha_z = 0.0374$ provides a good fit to the $v_c(R_0, z)$ profile of Milky Way potential (Dehnen & Binney 1998; Law & Majewski 2010). Both references have bulge, halo and disk components. The former has two double exponential disks while the later has a Miyamoto-Nagai disk.

To model systems where the potential is not separable in $R$ and $z$, a simpler approach is motivated by the fact that, for realistic Galactic potentials, we expect the $\overline{v_\phi}$ of a single age population to fall with $z$. Binney (2012) finds that when vertical motion is present, the effective potential for radial motion (see Eq. 15) needs to be modified because the vertical motion also contributes to the centrifugal potential. Neglecting this effect leads to an overestimation of $\overline{v_\phi}$. As one moves away from the plane, this effect becomes increasingly important. Furthermore, as shown by Schönrich (2012), in a given solar annulus, stars with smaller $R_g$ will have larger vertical energy and hence larger scale height. Moreover, stars with smaller $R_g$ are more likely to be found at higher $z$, consequently $\overline{v_\phi}$ should also decrease with height.

The fall of $\overline{v_\phi}$ with height is also predicted by the Jeans equation for an axisymmetric system

$$\overline{v_\phi}^2(R, z) \;=\; \left[ R \frac{\partial \Phi}{\partial R} \right] + \sigma_R^2 \left[ 1 - \frac{\sigma_\phi^2}{\sigma_R^2} + \frac{\partial \ln(\rho \sigma_R^2)}{\partial \ln R} \right] + R \left[ \frac{\partial \overline{v_R v_z}}{\partial z} + \overline{v_R v_z} \frac{\partial \ln \rho}{\partial z} \right]. \tag{25}$$

The $\overline{v_\phi}$ at high $z$ will be lower both because $R\,\partial\Phi/\partial R$ is lower and because the term in the third square bracket decreases with $z$, e.g., assuming $\overline{v_R v_z} = (\sigma_R^2 - \sigma_z^2)z/R$.

For the Gaussian model, Sharma et al. (2014) simulate the overall reduction of $\overline{v_\phi}$ with $z$ by introducing a parametrized form for $v_c(R, z)$ as given by Eq. (24) in Eq. (9). Given this prescription we expect $\alpha_z > 0.03744$, so as to account for effects other than that involving the first term in Eq. (25). In reality, the velocity dispersion tensor $\sigma^2$ will have a more complicated dependence on $R$ and $z$ than the exponential dependence on $R$.

For the Shu model, Sharma et al. (2014) replace $v_c$ in Eq. (17) by the form in Eq. (24). However, the prescription breaks the dynamical self-consistency of the model and turns it into a fitting formula. In reality, the $\overline{v_\phi}$ may not exactly follow the functional form for the vertical dependence predicted by our model, but is better than completely neglecting it.

## DISCLOSURE STATEMENT

The authors are not aware of any conflicts that might be perceived as affecting the objectivity of this review.

## ACKNOWLEDGMENTS

The initial idea for a review on the Galaxy's global and structural parameters came from John Kormendy. It has been challenging to write not least because this is a vibrant and dynamic field of research, and major uncertainties still exist. But our motto throughout − keep calm and carry on − has sustained us even when no clear picture has emerged at times. Inevitably, with imposed page limits, there will be missing topics and references for which we apologize in advance. We thank our referee Tim Beers for his oversight of the review, and Ken Freeman, Rosie Wyse and James Binney for their historical perspective, wisdom and insight. We are indebted to various colleagues for their support and help with figures and tables: C. Correa, P. Kafle, T. Licquia, F. Mignard, Y. Momany, M. Portail, J. Read, T. Tepper-Garcia, D. Webster, C. Wegg, and for additional advice, perspectives and comments: M. Arnaboldi, B. Benjamin, T. Bensby, J. Bovy, M. Boylan-Kolchin, R. Drimmel, S. Gillessen, Z. Ivezic, R. Lange, P. McMillan, D. Nataf, M. Reid, R. Schödel and R. Schönrich. JBH acknowledges the Kavli Institute, UC Santa Barbara for their hospitality during the early planning of this review. JBH is supported by an ARC Australian Laureate Fellowship. OG is grateful for the support of the Max Planck Institute for Extraterrestrial Physics, and acknowledges a visiting fellowship from the Hunstead Fund for Astrophysics at the University of Sydney and the hospitality of Mount Stromlo Observatory during the final stages of the review.

## LITERATURE CITED

Abadi M, Navarro J, Fardal M, Babul A, Steinmetz M. 2010. *MNRAS* 407:435
Abadi MG, Navarro JF, Steinmetz M. 2006. *MNRAS* 365:747
Adibekyan VZ, Santos NC, Sousa SG, Israelian G, Delgado Mena E, et al. 2012. *A&A* 543:89
Aguerri AL, Méndez-Abreu J, Falcón-Barroso J, Amorin A, Barrera-Ballesteros J, et al. 2015. *A&A* 576:A102
Aguerri JAL, Debattista VP, Corsini EM. 2003. *MNRAS* 338:465
Aihara H, Allende Prieto C, An D, Anderson S, Aubourg É, et al. 2011. *ApJS* 193:29
Alard C. 2001. *A&A* 379:L44

Allende Prieto C, Majewski S, Schiavon R, Cunha K, Frinchaboy P, et al. 2008. *Astronomische Nachrichten* 329:1018
Allgood B, Flores R, Primack J, Kravtsov A, Wechsler R, et al. 2006. *MNRAS* 367:1781
Alves-Brito A, Meléndez J, Asplund M, Ramírez I, Yong D. 2010. *A&A* 513:A35
Anderson M, Bregman J. 2010. *ApJ* 714:320
Anderson M, Bregman J. 2011. *ApJ* 737:22
Anguiano B, Zucker DB, Scholz RD, Grebel EK, Seabroke G, et al. 2015. *MNRAS* 451:1229
Aniyan S, Freeman KC, Gerhard OE, Arnaboldi M, Flynn C. 2016. *MNRAS* 456:1484
Antoja T, Helmi A, Dehnen W, Bienaymé O, Bland-Hawthorn J, et al. 2014. *A&A* 563:A60
Antonini F, Capuzzo-Dolcetta R, Mastrobuono-Battisti A, Merritt D. 2012. *ApJ* 750:111
Arnadottir AS, Feltzing S & Lundstrom I. 2009. *IAU Symp* 254:5
Athanassoula E. 1992. *MNRAS* 259:328
Athanassoula E. 2005. *MNRAS* 358:1477
Aumer M, Binney JJ. 2009. *MNRAS* 397:1286
Aumer M, Schönrich R. 2015. *MNRAS* 454:3166
Babusiaux C, Gilmore G. 2005. *MNRAS* 358:1309
Babusiaux C, Gómez A, Hill V, Royer F, Zoccali M, et al. 2010. *A&A* 519:A77
Bahcall J, Soneira R. 1980. *ApJS* 44:73
Bailin J, Kawata D, Gibson B, Steinmetz M, Navarro J, et al. 2005. *ApJ* 627:L17
Bajkova AT, Bobylev VV. 2015. *Balt Astron* 24:43
Balick B, Brown RL. 1974. *ApJ* 194:265
Bartko H, Martins F, Fritz TK, Genzel R, Levin Y, et al. 2009. *ApJ* 697:1741
Battaglia G, Helmi A, Morrison H, Harding P, Olszewski EW, et al. 2005. *MNRAS* 364:433
Beaulieu SF, Freeman KC, Kalnajs AJ, Saha P, Zhao H. 2000. *AJ* 120:855
Becklin EE, Neugebauer G. 1968. *ApJ* 151:145
Beers TC, Carollo D, Ivezić Ž, An D, Chiba M, et al. 2012. *ApJ* 746:34
Bell EF, Zucker DB, Belokurov V, Sharma S, Johnston KV, et al. 2008. *ApJ* 680:295
Beloborodov AM, Levin Y, Eisenhauer F, Genzel R, Paumard T, et al. 2006. *ApJ* 648:405
Belokurov V, Evans NW, Bell EF, Irwin MJ, Hewett PC, et al. 2007. *ApJ* 657:L89
Belokurov V, Koposov SE, Evans NW, Penarrubia J, Irwin MJ, et al. 2013. *MNRAS* 437:116
Belokurov V, Zucker DB, Evans NW, Gilmore G, Vidrih S, et al. 2006. *ApJ* 642:L137
Benjamin R, Churchwell E, Babler B, Indebetouw R, al. E. 2005. *ApJ* 630:L149
Bensby T. 2014. *A&A* 562:A71
Bensby T, Alves-Brito A, Oey M, Yong D, Meléndez J. 2010. *A&A* 516:L13
Bensby T, Alves-Brito A, Oey M, Yong D, Meléndez J. 2011. *ApJ* 735:L46
Bensby T, Feltzing S, Lundström I. 2003. *A&A* 410:527
Bensby T, Johnson J, Cohen J, Feltzing S, Udalski A, et al. 2009. *A&A* 499:737
Bensby T, Oey M, Feltzing S, Gustafsson B. 2007. *ApJ* 655:L89
Bensby T, Yee J, Feltzing S, Johnson J, Gould A, et al. 2013. *A&A* 549:A147
Benson A, Bower R, Frenk C, Lacey C, Baugh C, Cole S. 2003. *ApJ* 599:38
Bica E, Bonatto C, Barbuy B, Ortolani S. 2006. *A&A* 450:105
Bienayme O, Robin A, Creze M. 1987. *A&A* 180:94
Binney J. 2010. *MNRAS* 401:2318
Binney J. 2012. *MNRAS* 426:1328
Binney J. 2013. *New Astronomy Reviews* 57:29
Binney J, Burnett B, Kordopatis G, Steinmetz M, Gilmore G, et al. 2014. *MNRAS* 439:1231
Binney J, Gerhard O, Spergel D. 1997. *MNRAS* 288:365
Binney J, Gerhard OE, Stark AA, Bally J, Uchida KI. 1991. *MNRAS* 252:210
Binney J, McMillan P. 2011. *MNRAS* 413:1889
Binney, J., & Piffl, T. 2015, *MNRAS*, 454:3653
Bird SA, Flynn C. 2015. *MNRAS* 452:2675

Bissantz N, Englmaier P, Gerhard O. 2003. *MNRAS* 340:949
Bissantz N, Gerhard O. 2002. *MNRAS* 330:591
Blaauw A, Gum CS, Pawsey JL, Westerhout G. 1959. *ApJ* 130:702
Blaauw A, Gum CS, Pawsey JL, Westerhout G. 1960. *MNRAS* 121:123
Bland-Hawthorn J & Cohen M. 2003. *ApJ* 582:246
Bland-Hawthorn J, Krumholz M, Freeman K. 2010. *ApJ* 713:166
Bland-Hawthorn J, Vlajić M, Freeman K, Draine B. 2005. *ApJ* 629:239
Blanton M, Moustakas J. 2009. *ARA&A* 47:159
Blanton M, Roweis S. 2007. *AJ* 133:734
Blitz L, Robishaw T. 2000. *ApJ* 541:675
Bobylev VV. 2013. *Astron Lett* 39:95
Böker T. 2010. *IAU Symp* 266:58
Bonaca A, Jurić M, Ivezić Ž, Bizyaev D, Brewington H, et al. 2012. *AJ* 143:105
Bond NA, Ivezić Ž, Sesar B, Jurić M, Munn JA, et al. 2010. *ApJ* 716:1
Bottema R. 1993. *A&A* 275:16
Bovy J, Bird JC, Pérez AEG, Majewski SR, Nidever DL, Zasowski G. 2015. *ApJ* 800:83
Bovy J, Rix HW. 2013. *ApJ* 779:115
Bovy J, Allende Prieto C, Beers TC, Bizyaev D, da Costa LN, et al. 2012d. *ApJ* 759:131
Bovy J, Rix HW, Hogg DW. 2012a. *ApJ* 751:131
Bovy J, Rix HW, Liu C, Hogg DW, Beers TC, Lee YS. 2012b. *ApJ* 753:148
Bovy J, Tremaine S. 2012. *ApJ* 756:89
Bower GC, Falcke H, Herrnstein RM, Zhao JH, Goss WM, Backer DC. 2004. *Science* 304:704
Bregman J, Lloyd-Davies E. 2007. *ApJ* 669:990
Brook C, Stinson G, Gibson B, Kawata D, House E, et al. 2012. *MNRAS* 426:690
Bryan GL & Norman, ML. 1998. *ApJ* 495:80
Buchholz RM, Schödel R, Eckart A. 2009. *A&A* 499:483
Bullock JS, Johnston KV. 2005. *ApJ* 635:931
Bureau M, Aronica G, Athanassoula E, Dettmar RJ, Bosma A, Freeman KC. 2006. *MNRAS* 370:753
Burnett B, Binney J, Sharma S, Williams M, Zwitter T, et al. 2011. *A&A* 113:14
Burton WB. 1988. *Galactic and extragalactic radio astronomy (2nd Ed)*, Berlin New York, 295
Cabrera-Lavers A, Garzón F, Hammersley P. 2005. *A&A* 433:173
Cabrera-Lavers A, González-Fernández C, Garzón F, Hammersley P, López-Corredoira M. 2008. *A&A* 491:781
Cabrera-Lavers A, Hammersley P, González-Fernández C, López-Corredoira M, al. E. 2007. *A&A* 465:825
Calamida A, Sahu KC, Casertano S, Anderson J, Cassisi S, et al. 2015. *ApJ* 810:8
Cao L, Mao S, Nataf D, Rattenbury NJ, Gould A. 2013. *MNRAS* 434:595
Carney B, Seitzer P. 1993. *AJ* 105:2127
Carollo D, Beers TC, Lee YS, Chiba M, Norris JE, et al. 2007. *Nature* 450:1020
Carraro G. 2015. *Bull. Assoc. Argentina Astron.* 57:7
Carraro G, Vázquez RA, Costa E, Perren G, Moitinho A. 2010. *ApJ* 718:683
Casagrande L, Schönrich R, Asplund M, Cassisi S, Ramírez I, et al. 2011. *A&A* 530:A138
Catelan M, Pritzl BJ, Smith HA. 2004. *ApJS* 154:633
Catena R, Ullio P. 2010. *J Cosmol Astropart Phys* 2010:4
Cautun M, Frenk CS, van de Weygaert R, Hellwing WA, Jones BJT. 2014. *MNRAS* 445:2049
Chabrier G. 2003. *Publ Astron Soc Pacific* 115:763
Chakrabarty D. 2007. *A&A* 467:145
Chatzopoulos S, Fritz TK, Gerhard O, Gillessen S, Wegg C, et al. 2015. *MNRAS* 447:948
Chen B, Figueras F, Torra J, Jordi C, Luri X, Galadí-Enríquez D. 1999 *A&A* 352:459
Chen B, Stoughton C, Smith JA, Uomoto A, Pier JR, et al. 2001. *ApJ* 553:184
Cheng J, Rockosi C, Morrison H, Lee Y, Beers T, et al. 2012. *ApJ* 752:51

Chomiuk L, Povich M. 2011. *AJ* 142:197
Clarkson W, Sahu K, Anderson J, Smith T, Brown T, et al. 2008. *ApJ* 684:1110
Combes F, Debbasch F, Friedli D, Pfenniger D. 1990. *A&A* 233:82
Comerón S, Elmegreen, BG, Salo H et al. 2012. *ApJ* 759:98
Conti PS, Vacca WD. 1990. *AJ* 100:431
Contopoulos G. 1980. *A&A* 81:198
Cooper AP, Cole S, Frenk CS, White SDM, Helly J, et al. 2010. *MNRAS* 406:744
Cooper AP, Parry OH, Lowing B, Cole S, Frenk C. 2015. *MNRAS* 454:3185
Correa C, Wyithe J, Schaye J, Duffy A. 2015. *MNRAS* 452:1217
Cox T, Loeb A. 2008. *MNRAS* 386:461
Crain R, McCarthy I, Frenk C, Theuns T, Schaye J. 2010. *MNRAS* 407:1403
Cravens T, Robertson I, Snowden S. 2001. *J. Geophys. Res.* 106:24883
Cuddeford P, Amendt P. 1992. *MNRAS* 256:166
Dambis AK. 2009. *MNRAS* 396:553
de Bruijne J, Allen M, Azaz S, Krone-Martins A, Prod'homme T, Hestroffer D. 2015. *A&A* 576:A74
De Lucia G. 2012. *Astron Nachrichten* 333:460
De Lucia G, Helmi A. 2008. *MNRAS* 391:14
de Rossi M, Tissera P, De Lucia G, Kauffmann G. 2009. *MNRAS* 395:210
De Silva GM, Freeman KC, Bland-Hawthorn J, Martell S, de Boer EW, et al. 2015. *MNRAS* 449:2604
de Vaucouleurs G. 1983. *ApJ* 268:468
de Vaucouleurs G, Pence W. 1978. *AJ* 83:1163
Deason AJ, Belokurov V, Evans NW. 2011. *MNRAS* 416:2903
Deason AJ, Belokurov V, Evans NW, An J. 2012. *MNRAS* 424:L44
Deason AJ, Belokurov V, Evans NW, Johnston KV. 2013. *ApJ* 763:113
Deason AJ, Belokurov V, Koposov SE, Rockosi CM. 2014. *ApJ* 787:30
Debattista VP, Gerhard O, Sevenster MN. 2002. *MNRAS* 334:355
Dehnen W. 1998. *AJ* 115:2384
Dehnen W. 2000. *AJ* 119:800
Dehnen W, Binney JJ. 1998. *MNRAS* 298:387
Dékány I, Minniti D, Catelan M, Zoccali M, Saito RK, et al. 2013. *ApJ* 776:L19
Dékány I, Minniti D, Majaess D, Zoccali M, Hajdu G, et al. 2015. *ApJ* 812:L29
Delhaye J. 1965. In *Galactic Structure*, 61 (eds. A Blaauw, M Schmidt)
Deng LC, Newberg H, Liu C, Carlin J, Beers T, et al. 2012. *Research in A&A* 12:735
Di Matteo P, Haywood M, Gómez A, van Damme L, Combes F, et al. 2014. *A&A* 567:A122
Diplas A, Savage B. 1991. *ApJ* 377:126
Do T, Martinez GD, Yelda S, Ghez A, Bullock J, et al. 2013. *ApJ* 779:L6
Doeleman SS, Weintroub J, Rogers AEE, Plambeck R, Freund R, et al. 2008. *Nature* 455:78
Drimmel R, Spergel D. 2001. *ApJ* 556:181
Driver SP, Hill DT, Kelvin LS, Robotham ASG, Liske J, et al. 2011. *MNRAS* 413:971
Dubinski J, Carlberg R. 1991. *ApJ* 378:496
Dwek E, Arendt R, Hauser M, Kelsall T, al. E. 1995. *ApJ* 445:716
Eckart A, Genzel R. 1997. *MNRAS* 284:576
Eckart A, Genzel R, Hofmann R, Sams BJ, Tacconi-Garman LE. 1995. *ApJ* 445:L23
Edvardsson B, Andersen J, Gustafsson B, Lambert D, Nissen P, Tomkin J. 1993. *A&A* 275:101
Efremov Y. 2011. *Astronomy Reports* 55:108
Eggen O. 1951. *ApJ* 113:657
Eggen OJ, Lynden-Bell D, Sandage AR. 1962. *ApJ* 136:748
Eisenhauer F, Schdel R, Genzel R, Ott T, Tecza M, et al. 2003. *ApJ* 597:L121
Elias F, Alfaro EJ, Cabrera-Caño J. 2006. *AJ* 132:1052
Ellis SC, Bland-Hawthorn J. 2007. *MNRAS* 377:815

Englmaier P, Gerhard O. 1999. *MNRAS* 304:512
Evans NW, Sanders JL, Williams AA, An J, Lynden-Bell D, Dehnen W. 2016. *MNRAS* 456:4506
Faccioli L, Smith MC, Yuan HB, Zhang HH, Liu XW, et al. 2014. *ApJ* 788:105
Fang T, Bullock J, Boylan-Kolchin M. 2013. *ApJ* 762:20
Feast M, Whitelock P. 1997. *MNRAS* 291:683
Feldmeier A, Neumayer N, Seth A, Schödel R, Lützgendorf N, et al. 2014. *A&A* 570:A2
Feng Y, Di Matteo TD, Croft R, Tenneti A, Bird S, Battaglia N. 2015. *MNRAS* 455:2778
Fermani F, Schönrich R. 2013. *MNRAS* 432:2402
Finlator K, Ivezić Ž, Fan X, Strauss M, Knapp G, et al. 2000. *AJ* 120:2615
Flynn C, Holmberg J, Portinari L, Fuchs B, Jahreiss H. 2006. *MNRAS* 372:1149
Font AS, Johnston KV, Bullock JS, Robertson BE. 2006. *ApJ* 638:585
Font AS, McCarthy IG, Crain RA, Theuns T, Schaye J, et al. 2011. *MNRAS* 416:2802
Forero-Romero JE, Hoffman Y, Bustamante S, Gottloeber S, Yepes G. 2013. *ApJ* 767:5
Fox AJ, Wakker BP, Barger KA, Hernandez AK, Richter P, et al. 2014. *ApJ* 787:147
Francis C, Anderson E. 2014. *MNRAS* 441:1105
Freeman K. 2001. *ASP Conf* 230:91
Freeman K, Bland-Hawthorn J. 2002. *Annu Rev A&A* 40:487
Freudenreich HT. 1998. *ApJ* 492:495
Fritz TK, Chatzopoulos S, Gerhard O, Gillessen S, Genzel R, et al. 2014. *IAU Symp* 303:248
Fritz TK, Gillessen S, Dodds-Eden K, Lutz D, Genzel R, et al. 2011. *ApJ* 737:73
Fuchs B, Dettbarn C, Rix HW, Beers TC, Bizyaev D, et al. 2009. *AJ* 137:4149
Fuhrmann K. 1998. *A&A* 330:626
Fuhrmann K. 2008. *MNRAS* 384:173
Fux R. 1999. *A&A* 345:787
Garbari S, Liu C, Read JI, Lake G. 2012. *MNRAS* 425:1445
Gatto A, Fraternali F, Read J, Marinacci F, Lux H, Walch S. 2013. *MNRAS* 433:2749
Genzel R, Eisenhauer F, Gillessen S. 2010. *Rev Mod Phys* 82:3121
Genzel R, Pichon C, Eckart A, Gerhard OE, Ott T. 2000. *MNRAS* 317:348
Gerhard O, Martinez-Valpuesta I. 2012. *ApJ* 744:L8
Gerhard OE. 1999. *ASP Conf* 182:307
Ghez AM, Klein BL, Morris M, Becklin EE. 1998. *ApJ* 509:678
Ghez AM, Salim S, Weinberg NN, Lu JR, Do T, et al. 2008. *ApJ* 689:1044
Gibbons SLJ, Belokurov V, Evans NW. 2014. *MNRAS* 445:3788
Gillessen S, Eisenhauer F, Fritz TK, Bartko H, Dodds-Eden K, et al. 2009a. *ApJ* 707:L114
Gillessen S, Eisenhauer F, Fritz TK, Pfuhl O, Ott T, Genzel R. 2013. *IAU Symp* 289:29
Gillessen S, Eisenhauer F, Trippe S, Alexander T, Genzel R, et al. 2009b. *ApJ* 692:1075
Gilmore G, Randich S, Asplund M, Binney J, Bonifacio P, et al. 2012. *The Messenger* 147:25
Gilmore G, Reid N. 1983. *MNRAS* 202:1025
Gonzalez O, Rejkuba M, Minniti D, Zoccali M, Valenti E, Saito R. 2011a. *A&A* 534:L14
Gonzalez O, Rejkuba M, Zoccali M, Valenti E, Minniti D, et al. 2012. *A&A* 543:A13
Gonzalez OA, Gadotti DA. 2016. *Astr Space Sci Lib* 418:199
Gonzalez OA, Rejkuba M, Zoccali M, Hill V, Battaglia G, et al. 2011b. *A&A* 530:A54
Gonzalez OA, Rejkuba M, Zoccali M, Valent E, Minniti D, Tobar R. 2013. *A&A* 552:A110
Goodman AA, Alves J, Beaumont CN, Benjamin RA, Borkin MA, et al. 2014. *ApJ* 797:53
Gould A, Bahcall JN, Flynn C. 1996. *ApJ* 465:759
Gratton R, Carretta E, Matteucci F, Sneden C. 2000. *A&A* 358:671
Grcevich J, Putman M. 2009. *ApJ* 696:385
Groenewegen MAT. 2008. *A&A* 488:935
Groenewegen MAT, Blommaert JADL. 2005. *A&A* 443:143
Guedes J, Mayer L, Carollo M, Madau P. 2013. *ApJ* 772:36
Gupta A, Mathur S, Krongold Y, Nicastro F, Galeazzi M. 2012. *ApJ* 756:L8

Habing H. 1988. *A&A* 200:40
Habing HJ, Sevenster MN, Messineo M, van de Ven G, Kuijken K. 2006. *A&A* 458:151
Hammer F, Puech M, Flores H et al. 2012. *European Physical Journal Web of Conferences*, 19:01004
Hammersley P, Garzón F, Mahoney T, López-Corredoira M, Torres M. 2000. *MNRAS* 317:L45
Harris WE. 2010. *arXiv*:1012.3224
Hartmann D, Burton W. 1997. *Atlas of Galactic Neutral Hydrogen.*
Hawkins K, Jofre P, Masseron T, Gilmore G. 2015. *MNRAS* 453:758
Hayden MR, Bovy J, Holtzman JA, Nidever DL, Bird JC, et al. 2015. *ApJ* 808:132
Haywood M. 2006. *MNRAS* 371:1760
Haywood M, Matteo PD, Snaith O, Lehnert MD. 2015. *A&A* 579:5
Haywood M, Robin AC, Crézé M. 1997. *A&A* 320:428
Helmi A. 2004. *ApJ* 610:L97
Helmi A. 2008. *A&ARev* 15:145
Henley D, Shelton R. 2012. *ApJS* 202:14
Henley D, Shelton R, Kwak K, Joung M, Mac Low MM. 2010. *ApJ* 723:935
Hill V, Lecureur A, Gómez A, Zoccali M, Schultheis M, et al. 2011. *A&A* 534:A80
Hinshaw G, Spergel D, Verde L, Hill R, Meyer S, et al. 2003. *ApJS* 148:135
Honma M, Bushimata T, Choi YK, Hirota T, Imai H, et al. 2007. *PASJ* 59:889
Honma M, Nagayama T, Ando K, Bushimata T, Choi YK, et al. 2012. *PASJ* 64:136
Hopkins P, Kereš D, Oñorbe J, Faucher-Giguère CA, Quataert E, et al. 2014. *MNRAS* 445:581
Humphreys RM, Larsen JA. 1995. *AJ* 110:2183
Hunt JAS, Kawata D. 2014. *MNRAS* 443:2112
Ibata R, Irwin M, Lewis G, Ferguson A, Tanvir N. 2003. *MNRAS* 340:L21
Ibata R, Lewis GF, Irwin M, Totten E, Quinn T. 2001. *ApJ* 551:294
Ibata R, Lewis GF, Martin NF, Bellazzini M, Correnti M. 2013. *ApJ* 765:L15
Ibata RA, Wyse RFG, Gilmore G, Irwin MJ, Suntzeff NB. 1997. *AJ* 113:634
Irwin M, Ferguson A, Ibata R, Lewis G, Tanvir N. 2005. *ApJ* 628:L105
Ivezić Ž, Beers TC, Jurić M. 2012. *Annu Rev A&A* 50:251
Ivezić Ž, Sesar B, Jurić M, Bond N, Dalcanton J, et al. 2008. *ApJ* 684:287
Jofré P, Heiter U, Soubiran C, Blanco-Cuaresma S, Worley C, et al. 2014. *A&A* 564:A133
Johnson CI, Rich MR, Fulbright JP, Valenti E, McWilliam A. 2011. *ApJ* 732:108
Johnston KV, Law DR, Majewski SR. 2005. *ApJ* 619:800
Jurić M, Ivezić Ž, Brooks A, Lupton RH, Schlegel D, et al. 2008. *ApJ* 673:864
Just A, Jahreiss H. 2010. *MNRAS* 402:461
Kafle PR, Sharma S, Lewis GF, Bland-Hawthorn J. 2012. *ApJ* 761:98
Kafle, P. R., Sharma, S., Lewis, G. F., & Bland-Hawthorn, J. 2014. *ApJ* 794:59
Kalberla PMW, Dedes L. 2008. *A&A* 487:951
Kalberla PMW, Dedes L, Kerp J, Haud U. 2007. *A&A* 469:511
Kalnajs AJ. 1991. *Dynamics of Disc Galaxies*, 323 (ed. B. Sundelius)
Kapteyn J. 1922. *ApJ* 55:302
Kazantzidis S, Kravtsov A, Zentner A, Allgood B, Nagai D, Moore B. 2004. *ApJ* 611:L73
Kent SM. 1992. *ApJ* 387:181
Kent SM, Dame TM, Fazio G. 1991. *ApJ* 378:131
Kerr FJ, Lynden-Bell D. 1986. *MNRAS* 221:1023
Kimmig B, Seth A, Ivans II, Strader J, Caldwell N, et al. 2015. *AJ* 149:53
King C, Brown WR, Geller MJ, Kenyon SJ. 2015. *ApJ* 813:89
Klypin A, Zhao H & Somerville RS. 2002. *ApJ* 573:597
Kobayashi N, Yasui C, Tokunaga A, Saito M. 2008. *ApJ* 683:178
Koposov SE, Rix HW, Hogg DW. 2010. *ApJ* 712:260
Kordopatis G, Wyse RFG, Gilmore G, Recio-Blanco A, de Laverny P, et al. 2015. *A&A* 582:122
Kormendy J, Barentine JC. 2010. *ApJ* 715:L176

Kormendy J, Drory N, Bender R, Cornell M. 2010. *ApJ* 723:54
Kormendy J, Ho LC. 2013. *Annu Rev A&A* 51:511
Kormendy J. 2013. *Secular Evolution in Disk Galaxies*, XXIII Canary Islands Winter School of Astrophysics, ed. J. Falcon-Barroso & J. H. Knapen (Cambridge: Cambridge Univ. Press), p. 1.
Krabbe A, Genzel R, Eckart A, Najarro F, Lutz D, et al. 1995. *ApJ* 447
Kroupa P. 2001. *MNRAS* 322:231
Kuijken K, Gilmore G. 1989. *MNRAS* 239:571
Kunder A, Koch A, Rich R, de Propris R, Howard C, et al. 2012. *AJ* 143:57
Küpper AHW, Balbinot E, Bonaca A, Johnston KV, Hogg DW, et al. 2015. *ApJ* 803:80
Lacy JH, Townes CH, Geballe TR, Hollenbach DJ. 1980. *ApJ* 241:132
Lange R, Driver S, Robotham A, Kelvin L, Graham A, et al. 2015. *MNRAS* 447:2603
Larsen JA, Humphreys RM. 2003. *AJ* 125:1958
Launhardt R, Zylka R, Mezger PG. 2002. *A&A* 384:112
Laurikainen E, Salo H, Athanassoula E, Bosma A, Herrera-Endoqui M. 2014. *MNRAS* 444:L80
Laurikainen E, Salo H, Buta R, Knapen JH. 2011. *MNRAS* 418:1452
Law DR, Majewski SR. 2010. *ApJ* 714:229
Lewis JR, Freeman KC. 1989. *AJ* 97:139
Li YS, White SDM. 2008. *MNRAS* 384:1459
Li ZY, Shen J. 2012. *ApJ* 757:L7
Licquia TC, Newman JA. 2015. *ApJ* 806:96
Licquia TC, Newman JA, Brinchmann J. 2015, *apj* 809:96
Lindqvist M, Habing HJ, Winnberg A. 1992. *A&A* 259:118
Loebman, S. R., Roškar, R., Debattista, V. P., et al. 2011, *ApJ*, 737:8
Loebman SR, Ivezić Ž, Quinn TR, Governato F, Brooks AM, et al. 2012. *ApJ* 758:L23
Long RJ, Mao S, Shen J, Wang Y. 2012. *MNRAS* 428:3478
López-Corredoira M. 2014. *A&A* 563:A128
López-Corredoira M, Cabrera-Lavers A, Garzón F, Hammersley P. 2002. *A&A* 394:883
López-Corredoira M, Cabrera-Lavers A, Gerhard O. 2005. *A&A* 439:107
Lowing B, Wang W, Cooper A, Kennedy R, Helly J, et al. 2014. *MNRAS* 446:2274
Magrini L, Randich S, Donati P, Bragaglia A, Adibekyan V, et al. 2015. *A&A* 580:A85
Maíz-Apellániz J. 2001. *AJ* 121:2737
Majaess D. 2010. *Acta Astron* 60:55
Malhotra S, Spergel D, Rhoads J, Li J. 1996. *ApJ* 473:687
Malkin Z. 2013. *IAU Symp* 289:406
Martinez-Valpuesta I, Gerhard O. 2013. *ApJ* 766:L3
Martinsson TPK, Verheijen MAW, Westfall KB, Bershady MA, Andersen DR, Swaters RA. 2013. *A&A* 557:A131
Masseron T, Gilmore G. 2015. *MNRAS* 453:1855
Matsunaga N, Feast MW, Kawadu T, Nishiyama S, Nagayama T, et al. 2013. *MNRAS* 429:385
Matsunaga N, Kawadu T, Nishiyama S, Nagayama T, Hatano H, et al. 2009. *MNRAS* 399:1709
Matsunaga N, Kawadu T, Nishiyama S, Nagayama T, Kobayashi N, et al. 2011. *Nature* 477:188
May J, Bronfman L, Alvarez H, Murphy D, Thaddeus P. 1993. *A&AS* 99:105
McCarthy IG, Font AS, Crain RA, Deason AJ, Schaye J, Theuns T. 2012. *MNRAS* 420:2245
McKee C, Williams J. 1997. *ApJ* 476:144
McKee CF, Parravano A, Hollenbach DJ. 2015. *ApJ* 814:1
McMillan PJ. 2011 *MNRAS* 414:2446
McWilliam A, Zoccali M. 2010. *ApJ* 724:1491
Mendez RA, van Altena WF. 1998. *A&A* 330:910
Merritt D. 2013. *Dynamics and Evolution of Galactic Nuclei.*
Merritt D, Berczik P, Laun F. 2007. *AJ* 133:553
Mignard F. 2011. ftp://ftp.oca.eu/pub/mignard/TN_Gaia/GAIA-CA-TN-OCA-FM-048.pdf

Mihalas D, Binney J. 1981. Galactic Astronomy: Structure and Kinematics. (San Francisco: WH Freeman)
Miller M, Bregman J. 2013. *ApJ* 770:118
Miller M, Bregman J. 2015. *ApJ* 800:14
Minchev I, Chiappini C, Martig M. 2014. *A&A* 572:A92
Minchev I & Famaey B. 2010. *ApJ* 722:112
Minchev I, Martig M, Streich D et al. 2015. *ApJ* 804:L9
Minchev I, Nordhaus J, Quillen AC. 2007. *ApJ* 664:L31
Minniti D, Lucas PW, Emerson JP, Saito RK, Hempel M, et al. 2010. *New Astronomy* 15:433
Minniti D, Saito R, Alonso-García J, Lucas P, Hempel M. 2011. *ApJ* 733:L43
Molinari S, Bally J, Noriega-Crespo A, Compiègne M, Bernard JP, et al. 2011. *ApJ* 735:L33
Momany Y, Zaggia S, Gilmore G, Piotto G, Carraro G, et al. 2006. *A&A* 451:515
Moni Bidin C, Carraro G, Méndez RA. 2012. *ApJ* 747:101
Morris MR, Meyer L, Ghez AM. 2012. *Res A&A* 12:995
Morrison HL. 1993. *AJ* 106:578
Munn J, Monet D, Levine S, Canzian B, Pier J, et al. 2004. *AJ* 127:3034
Mutch SJ, Croton DJ, Poole GB. 2011. *ApJ* 736:84
Nataf DM, Udalski A, Gould A, Fouqué P, Stanek K. 2010. *ApJ* 721:L28
Nataf DM, Gould A, Fouqué P, Gonzalez OA, Johnson JA, et al. 2013. *ApJ* 769:88
Nataf DM, Udalski A, Skowron J, Szyma ski MK, Kubiak M, et al. 2015. *MNRAS* 447:1535
Ness M, Freeman K, Athanassoula E, Wylie-De-Boer E, Bland-Hawthorn J, et al. 2012. *ApJ* 756:22
Ness M, Freeman K, Athanassoula E, Wylie-de-Boer E, Bland-Hawthorn J, et al. 2013a. *MNRAS* 430:836
Ness M, Freeman K, Athanassoula E, Wylie-de-Boer E, Bland-Hawthorn J, et al. 2013b. *MNRAS* 432:2092
Ness M, Hogg D, Rix HW, Ho A, Zasowski G. 2015. *ApJ* 808:16
Newberg H, Yanny B, Rockosi C, Grebel E, Rix HW, et al. 2002. *ApJ* 569:245
Nichols M, Bland-Hawthorn J. 2011. *ApJ* 732:17
Nidever DL, Bovy J, Bird JC, Andrews BH, Hayden M, et al. 2014 *ApJ* 796:3
Niederste-Ostholt M, Belokurov V, Evans NW, Peñarrubia J. 2010. *ApJ* 712:516
Nishiyama S, Nagata T, Baba D, Haba Y, Kadowaki R, et al. 2005. *ApJ* 621:L105
Nishiyama S, Nagata T, Sato S, Kato D, Nagayama T, et al. 2006. *ApJ* 647:1093
Nishiyama S, Nagata T, Tamura M, Kandori R, Hatano H, et al. 2008. *ApJ* 680:1174
Nishiyama S, Yasui K, Nagata T, Yoshikawa T, Uchiyama H, et al. 2013. *ApJ* 769:L28
Nissen PE & Schuster WJ. 2011. *A&A* 530, A15
Nordström B, Mayor M, Andersen J, Holmberg J, Pont F, et al. 2004. *A&A* 418:989
Norris J, Ryan S. 1991. *ApJ* 380:403
Nuza S, Parisi F, Scannapieco C, Richter P, Gottlöber S, Steinmetz M. 2014. *MNRAS* 441:2593
Obreja A, Domínguez-Tenreiro R, Brook C, Martínez-Serrano FJ, Doménech-Moral M, et al. 2013. *ApJ* 763:26
Ojha DK. 2001. *MNRAS* 322:426
Oort JH, Rougoor GW. 1960. *MNRAS* 121
Ortolani S, Renzini A, Gilmozzi R, Marconi G, Barbuy B, et al. 1995. *Nature* 377:701
Paczynski B, Stanek KZ. 1998. *ApJ* 494:L219
Paerels F, Kahn S. 2003. *ARA&A* 41:291
Pandey AK, Bhatt BC, Mahra HS. 1988. *A&A* 189:66
Parkinson H, Cole S, Helly J. 2008. *MNRAS* 383:557
Pasetto S, Grebel EK, Zwitter T, Chiosi C, Bertelli G, et al. 2012. *Astron. Astrophys.* 547:A70
Patterson FS. 1940. *Harvard College Observatory Bulletin* 914:9
Paumard T, Genzel R, Martins F, Nayakshin S, Beloborodov AM, et al. 2006. *ApJ* 643:1011
Peebles P, Tully R. 2013. *arXiv*:1302.6982

Perryman M, Spergel DN, Lindegren L. 2014. *ApJ* 789:166
Pfenniger D, Friedli D. 1991. *A&A* 252:75
Pfuhl O, Fritz TK, Zilka M, Maness H, Eisenhauer F, et al. 2011. *ApJ* 741:108
Piddington JH, Minnett HC. 1951. *Aust J Sci Res* A4:459
Pietrukowicz P, Kozlowski S, Skowron J, Soszynski I, Udalski A, et al. 2015. *ApJ* 811:113
Piffl T, Binney J, McMillan PJ, Steinmetz M, Helmi A, et al. 2014a. *MNRAS* 445:3133
Piffl T, Scannapieco C, Binney JJ, Steinmetz M, et al. 2014b. *A&A* 562:A91
Pila-Díez B, de Jong JTA, Kuijken K, van der Burg RFJ, Hoekstra H. 2015. *A&A* 579:A38
Pillepich A, Madau P, Mayer L. 2015. *ApJ* 799:184
Pillepich A, Vogelsberger M, Deason A, Rodriguez-Gomez V, Genel S, et al. 2014. *MNRAS* 444:237
Pipino A, Matteucci F, D'Ercole A. 2008. *IAU Symp* 245:19
Pohlen M, Trujillo I. 2006. *A&A* 454:759
Portail M, Wegg C, Gerhard O. 2015. *MNRAS* 450:L66
Portail M, Wegg C, Gerhard O, Martinez-Valpuesta I. 2015. *MNRAS* 448:713
Prada F, Klypin A, Simonneau E, Betancort-Rijo J, Patiri S, et al. 2006. *ApJ* 645:1001
Prochaska J, Naumov S, Carney B, McWilliam A, Wolfe A. 2000. *AJ* 120:2513
Putman M, Gibson B, Staveley-Smith L, Banks G, Barnes D, et al. 1998. *Nature* 394:752
Quillen A, Garnett D. 2001. *ASP Conf* 230:87
Raha N, Sellwood JA, James RA, Kahn FD. 1991. *Nature* 352:411
Rattenbury NJ, Mao S, Sumi T, Smith MC. 2007. *MNRAS* 378:1064
Read JI. 2014. *J Phys G Nucl Part Phys* 41:63101
Reddy B, Lambert D, Allende Prieto C. 2006. *MNRAS* 367:1329
Reddy B, Tomkin J, Lambert D, Allende Prieto C. 2003. *MNRAS* 340:304
Reid MJ. 1993. *Annual Review of A&A* 31:345
Reid MJ. 2008. *IAU Symp* 248:141
Reid MJ. 2009. *Int J Mod Phys D* 18:889
Reid MJ, Brunthaler A. 2004. *ApJ* 616:872
Reid MJ, Menten KM, Brunthaler A, Zheng XW, Dame TM, et al. 2014. *ApJ* 783:130
Reid MJ, Menten KM, Genzel R, Ott T, Schodel R, Eckart A. 2003. *ApJ* 587:208
Reid MJ, Menten KM, Zheng XW, Brunthaler A, Moscadelli L, et al. 2009a. *ApJ* 700:137
Reid MJ, Menten KM, Zheng XW, Brunthaler A, Xu Y. 2009b. *ApJ* 705:1548
Reylé C, Marshall D, Robin A, Schultheis M. 2009. *A&A* 495:819
Rich RM. 2013. *Planets, Stars and Stellar Systems*. vol. 5 (Dordrecht: Springer Netherlands)
Rix HW, Bovy J. 2013. *A&ARev* 21:61
Robin A, Creze M, Mohan V. 1992. *ApJ* 400:L25
Robin A, Reylé C, Fliri J, Czekaj M, Robert C, Martins A. 2014. *A&A* 569:A13
Robin AC, Reylé C, Derrière S, Picaud S. 2003. *A&A* 409:523
Robotham ASG, Baldry IK, Bland-Hawthorn J, Driver SP, Loveday J, et al. 2012. *MNRAS* 424:1448
Rodriguez-Fernandez N, Combes F. 2008. *A&A* 489:115
Rojas-Arriagada A, Recio-Blanco A, Hill V, de Laverny P, Schultheis M, et al. 2014. *A&A* 569:A103
Ruphy S, Robin A, Epchtein N, Copet E, Bertin E, et al. 1996. *A&A* 313:L21
Ryde N, Gustafsson B, Edvardsson B, Meléndez J, Alves-Brito A, et al. 2010. *A&A* 509:A20
Sackett PD. 1997. *ApJ* 483:103
Saglia RP, Opitsch M, Erwin P, Thomas J, Beifiori A, et al. 2016. *arXiv*:1601.00974
Saha K, Martinez-Valpuesta I, Gerhard O. 2012. *MNRAS* 421:333
Saito R, Minniti D, Dias B, Hempel M, Rejkuba M, et al. 2012. *A&A* 544:A147
Salaris M, Girardi L. 2002. *MNRAS* 337:332
Sale SE, Drew JE, Unruh YC, Irwin MJ, Knigge C, et al. 2009. *MNRAS* 392:497
Salem M, Besla G, Bryan G, Putman M, van der Marel RP, Tonnesen S. 2015
Samland M, Gerhard O. 2003. *A&A* 399:961
Sanders J, Binney J. 2015 *MNRAS* 449:3479

Sato M, Reid MJ, Brunthaler A, Menten KM. 2010. *ApJ* 720:1055
Scannapieco C, Creasey P, Nuza SE, Yepes G, Gottloeber S, Steinmetz M. 2015 :12
Schechtman-Rook A, Bershady MA. 2013. *ApJ* 773:45
Schlaufman KC, Rockosi CM, Prieto CA, Beers TC, Bizyaev D, et al. 2009. *ApJ* 703:2177
Schmidt M. 1963. *ApJ* 137:758
Schödel R, Feldmeier A, Kunneriath D, Stolovy S, Neumayer N, et al. 2014a. *A&A* 566:A47
Schödel R, Feldmeier A, Neumayer N, Meyer L, Yelda S. 2014b. *Class Quantum Gravity* 31:244007
Schönrich R. 2012. *MNRAS* 427:274
Schönrich R, Asplund M, Casagrande L. 2014. *ApJ* 786:7
Schönrich R, Binney J. 2009. *MNRAS* 396:203
Schönrich R, Binney JJ & Dehnen W. 2010. *MNRAS*, 403:1829
Schönrich R, Aumer M, Sale SE. 2015. *ApJ* 812:L21
Schuster W, Moitinho A, Márquez A, Parrao L, Covarrubias E. 2006. *A&A* 445:939
Searle L, Zinn R. 1978. *ApJ* 225:357
Sellwood J, Binney J. 2002. *MNRAS* 336:785
Sellwood Ja. 2013. *ApJ* 769:L24
Sembach K, Wakker B, Savage B, Richter P, Meade M, et al. 2003. *ApJS* 146:165
Sesar B, Ivezić Ž, Grammer SH, Morgan DP, Becker AC, et al. 2010. *ApJ* 708:717
Sesar B, Ivezić Ž, Stuart JS, Morgan DM, Becker AC, et al. 2013. *AJ* 146:21
Shapley H. 1918. *ApJ* 48:154
Sharma S, Bland-Hawthorn J. 2013. *ApJ* 773:183
Sharma S, Bland-Hawthorn J, Binney J, Freeman KC, Steinmetz M, et al. 2014. *ApJ* 793:51
Sharma S, Bland-Hawthorn J, Johnston KV, Binney J. 2011. *ApJ* 730:3
Shen J, Li ZY. 2015. *arXiv*:1504.05136
Shen J, Rich RM, Kormendy J, Howard CD, De Propris R, Kunder A. 2010b. *ApJ* 720:L72
Shen ZQ, Lo KY, Liang MC, Ho PTP, Zhao JH. 2005. *Nature* 438:62
Shull JM. 2014. *ApJ* 784:142
Shuter WLH. 1982. *MNRAS* 199:109
Siebert A, Bienaymé O, Binney J, Bland-Hawthorn J, Campbell R, et al. 2008. *MNRAS* 391:793
Siebert A, Famaey B, Binney J, Burnett B, Faure C, et al. 2012. *MNRAS* 425:2335
Siebert a, Famaey B, Minchev I, Seabroke GM, Binney J, et al. 2011. *MNRAS* 412:2026
Siegel MH, Majewski SR, Reid IN, Thompson IB. 2002. *ApJ* 578:151
Sirko E, Goodman J, Knapp GR, Brinkmann J, Ivezi E, et al. 2004. *AJ* 127:914
Skrutskie M, Cutri R, Stiening R, Weinberg M, Schneider S, et al. 2006. *AJ* 131:1163
Skrutskie MF, Cutri RM, Stiening R, Weinberg MD, et al. 2006. *AJ* 131:1163
Smith MC, Evans NW, Belokurov V, Hewett PC, Bramich DM, et al. 2009. *MNRAS* 399:1223
Smith MC, Ruchti GR, Helmi A, Wyse RFG, Fulbright JP, et al. 2007. *MNRAS* 379:755
Snaith O, Haywood M, Di Matteo P, Lehnert M, Combes F, et al. 2014. *ApJ* 781:L31
Snowden S, Cox D, McCammon D, Sanders W. 1990. *ApJ* 354:211
Snowden S, Egger R, Freyberg M, McCammon D, Plucinsky P, et al. 1997. *ApJ* 485:125
Sofue Y, Honma M, Omodaka T. 2009. *PASJ* 61:227
Sofue Y, Nagayama T, Matsui M, Nakagawa A. 2011. *PASJ* 63:867
Sormani MC, Binney J, Magorrian J. 2015
Soto M, Rich RM, Kuijken K. 2007. *ApJ* 665:L31
Soubiran C, Bienaymé O, Siebert A. 2003. *A&A* 398:141
Spitzer L. 1956. *ApJ* 124:20
Spitzer L, Schwarzschild M. 1953. *ApJ* 118:106
Stanek K, Udalski A, Szymanski M, Kaluzny J, Kubiak M, et al. 1997. *ApJ* 477:163
Stanimirović S, Dickey J, Krčo M, Brooks A. 2002. *ApJ* 576:773
Steinmetz M, Zwitter T, Siebert A, Watson FG, Freeman KC, et al. 2006. *AJ* 132:1645
Stewart K, Bullock J, Wechsler R, Maller A, Zentner A. 2008. *ApJ* 683:597

Stinson G, Bovy J, Rix HW, Brook C, Roškar R, et al. 2013. *MNRAS* 436:625
Stothers R, Frogel JA. 1974. *AJ* 79:456
Strömberg G. 1925. *ApJ* 61:363
Tepper-Garcia T, Bland-Hawthorn J, Sutherland RS. 2015. *ApJ* 813:94
Tian HJ, Liu C, Carlin JL, Zhao YH, Chen XL, et al. 2015 *ApJ* 809:145
Tissera PB, Scannapieco C, Beers TC, Carollo D. 2013. *MNRAS* 432:3391
Toller GN. 1990. *IAU Symp* 139:21
Trippe S, Gillessen S, Gerhard OE, Bartko H, Fritz TK, et al. 2008. *A&A* 492:419
Tully R, Courtois H, Hoffman Y, Pomarède D. 2014. *Nature* 513:71
Udalski A, Szymanski MK, Soszynski I, Poleski R. 2008. *Acta Astron* 58:69
Uemura M, Ohashi H, Hayakawa T, Ishida E, Kato T, Hirata R. 2000. *PASJ* 52:143
Valenti E, Zoccali M, Gonzalez OA, Minniti D, Alonso-Garcia J, et al. 2015. *arXiv*:151007425
van den Bergh S. 1999. *A&A Rev.* 9:273
van der Kruit P. 1986. *A&A* 157:230
van der Kruit PC, Freeman KC. 2011. *Annu Rev A&A* 49:301
van der Marel, RP, Fardal M, Besla G, et al. 2012a. *ApJ*, 753, 8
van der Marel, RP, Besla G, Cox TJ, Sohn ST, Anderson, J. 2012b. *ApJ*, 753, 9
van Tulder JJM. 1942. *Bull Astron Inst Netherlands* 9
Vanhollebeke E, Groenewegen MAT, Girardi L. 2009. *A&A* 498:95
Vivas AK, Zinn R. 2006. *AJ* 132:714
Wainscoat R, Freeman K, Hyland A. 1989. *ApJ* 337:163
Wang Q, Yao Y. 2012. *arXiv*:1211.4834
Watkins LL, Evans NW, An JH. 2010. *MNRAS* 406:264
Watkins LL, Evans NW, Belokurov V, Smith MC, Hewett PC, et al. 2009. *MNRAS* 398:1757
Wegg C, Gerhard O. 2013. *MNRAS* 435:1874
Wegg C, Gerhard O, Portail M. 2015. *MNRAS* 450:4050
Weiland J, Arendt R, Berriman G, Dwek E, Freudenreich H, et al. 1994. *ApJ* 425:L81
Weiner BJ, Sellwood JA. 1999. *ApJ* 524:112
Wetzel AR, Hopkins PF, Kim JH, et al. 2016. *arXiv*:1602.05957
Wielen R. 1977. *A&A* 60:263
Wilkinson MI, Evans NW. 1999. *MNRAS* 310:645
Williams MEK, Steinmetz M, Binney J, Siebert A, Enke H, et al. 2013. *MNRAS* 436:101
Xu Y, Newberg H, Carlin J, Liu C, Deng L, et al. 2015. *ApJ* 801:105
Xue XX, Ma Z, Rix HW, Morrison HL, Harding P, et al. 2014. *ApJ* 784:170
Xue XX, Rix HW, Ma Z, Morrison H, Bovy J, et al. 2015. *ApJ* 809:144
Xue XX, Rix HW, Zhao G, Re Fiorentin P, Naab T, et al. 2008. *ApJ* 684:1143
Yanny B, Newberg HJ, Grebel EK, Kent S, Odenkirchen M, et al. 2003. *ApJ* 588:824
Yanny B, Rockosi C, Newberg HJ, Knapp GR, Adelman-McCarthy JK, et al. 2009. *AJ* 137:4377
Yao Y, Wang Q. 2007. *ApJ* 666:242
Yasui C, Kobayashi N, Tokunaga A, Terada H, Saito M. 2008. *ApJ* 675:443
Yepes G, Gottlöber S, Hoffman Y. 2014. *New Astronomy Reviews* 58:1
Yoachim P, Dalcanton J. 2006. *AJ* 131:226
Zhang L, Rix HW, van de Ven G, Bovy J, Liu C, Zhao G. 2013. *ApJ* 772:108
Zhao H, Spergel DN, Rich RM. 1994. *AJ* 108:2154
Zheng Z, Flynn C, Gould A, Bahcall J, Salim S. 2001. *ApJ* 555:393
Zhu Z, Shen M. 2013. *IAU Symp* 289:444
Zoccali M, Cassisi S, Frogel JA, Gould A, Ortolani S, et al. 2000. *ApJ* 530:418
Zoccali M, Gonzalez OA, Vasquez S, Hill V, Rejkuba M, et al. 2014. *A&A* 562:A66
Zoccali M, Hill V, Lecureur A, Barbuy B, Renzini A, et al. 2008. *A&A* 486:177
Zwitter T, Matijevic G, Breddels Ma, Smith MC, Helmi A, et al. 2010. *AJ* 54:16